

Imperial College of Science, Technology and Medicine  
Department of Physics

# Topological Defect Formation in Quantum Phase Transitions

Edward Gillman

Submitted in part fulfilment of the requirements for the degree of  
Doctor of Philosophy in Physics of Imperial College London and  
the Diploma of Imperial College, May 2018



## **Declaration of Authorship**

Unless otherwise referenced, the work presented in this thesis is my own - Edward Gillman.

The copyright of this thesis rests with the author and is made available under a Creative Commons Attribution Non-Commercial No Derivatives licence. Researchers are free to copy, distribute or transmit the thesis on the condition that they attribute it, that they do not use it for commercial purposes and that they do not alter, transform or build upon it. For any reuse or redistribution, researchers must make clear to others the licence terms of this work.



## Abstract

The Kibble Zurek mechanism describes the universal formation of topological defects during continuous symmetry breaking phase transitions. It has been confirmed in a wide variety of systems and is of interest within theoretical high energy physics and cosmology. While during high temperature phase transitions classical methods can be used to study topological defect formation, in zero temperature quantum phase transitions, quantum effects can dominate dynamics such that classical approximations fail. This is problematic in quantum field theory because topological defect formation constitutes a non-perturbative non-equilibrium phenomenon, yet there are at present no well-developed non-perturbative non-equilibrium methods available for calculations. Nonetheless, due to its generality and confirmation in other cases, the Kibble-Zurek mechanism is expected to hold. This means that in addition to being of physical interest in its own right, the Kibble-Zurek mechanism is also an excellent test for any potential non-perturbative non-equilibrium techniques.

In this thesis, tensor network techniques are applied to the problem of confirming the Kibble Zurek mechanism in the  $\phi^4$  quantum field theory in  $D = (1 + 1)$  spacetime dimensions. Such techniques have already been highly successful in condensed matter and to some extent in quantum field theory. The kink defects of the theory are studied both in equilibrium and in the non-equilibrium scenario of their formation. Results consistent with the Kibble-Zurek mechanism are found, which provides evidence that the mechanism holds in this case and confirms tensor networks as a promising non-perturbative non-equilibrium method for quantum field theory. As tensor network methods are developed further to higher dimensions and more sophisticated theories, they could one day provide a powerful method for the non-perturbative study of non-equilibrium high energy physics and cosmology, an area of physics which remains essentially unexplored yet important for our understanding of nature.



## **Acknowledgements**

I would like to thank my supervisor Arttu Rajantie for his help and support during the past four years.

# Abbreviations

<b>KZM</b>	Kibble-Zurek Mechanism
<b>QFT</b>	Quantum Field Theory
<b>QPT</b>	Quantum Phase Transition
<b>UV</b>	Ultraviolet
<b>IR</b>	Infrared
<b>2PI</b>	Two Particle Irreducible
<b>nPI</b>	$n$ Particle Irreducible
<b>AIA</b>	Adiabatic-Impulse-Adiabatic
<b>PBC</b>	Periodic Boundary Conditions
<b>OBC</b>	Open Boundary Conditions
<b>TPBC</b>	Twisted Periodic Boundary Conditions
<b>TN</b>	Tensor Network
<b>TNR</b>	Tensor Network Representation
<b>MPS</b>	Matrix Product State
<b>MPO</b>	Matrix Product Operator
<b>PEPS</b>	Projected Entangled Pairs State
<b>CFT</b>	Conformal Field Theory
<b>uMPS</b>	Uniform Matrix Product State
<b>vMPS</b>	Variational Matrix Product State
<b>vuMPS</b>	Variational Uniform Matrix Product State
<b>TDVP</b>	Time Dependent Variational Principle

# Contents

<b>Declaration of Authorship</b>	<b>3</b>
<b>Abstract</b>	<b>5</b>
<b>Acknowledgements</b>	<b>7</b>
<b>Contents</b>	<b>9</b>
<b>List of Figures</b>	<b>15</b>
<b>List of Tables</b>	<b>17</b>
<b>Preface</b>	<b>19</b>
<b>1 Introduction</b>	<b>22</b>
1.1 Topological Defects and Their Formation . . . . .	22
1.1.1 Topological Defects . . . . .	22
1.1.2 The Formation of Topological Defects and Symmetry Breaking	23
1.1.3 The Kibble-Zurek Mechanism in Quantum Theory . . . . .	24
1.2 Thesis Outline . . . . .	25
<b>2 Topological Defects</b>	<b>27</b>
2.1 Introduction . . . . .	27
2.2 Topological Defects in Classical Field Theory . . . . .	28
2.2.1 Action, Energy Functional and Equations of Motion . . . . .	28

2.2.2	Classical Vacua, Elementary Particles and Phase Transition . . . . .	29
2.2.3	Topological Charge and Sectors . . . . .	30
2.2.4	Topological Charge and Sectors in Classical Field Theory: A General Analysis . . . . .	31
2.2.5	Kink Defects in $\phi^4$ . . . . .	32
2.3	Topological Defects in Quantum Theory . . . . .	34
2.3.1	Hamiltonian and Field Eigenbasis . . . . .	34
2.3.2	Vacua, Particles and Symmetry Breaking . . . . .	35
2.3.3	Topological Charge and Sectors . . . . .	37
2.3.4	Kinks . . . . .	39
2.3.5	Summary of Critical Exponents . . . . .	41
<b>3</b>	<b>Topological Defect Formation</b>	<b>43</b>
3.1	Introduction . . . . .	43
3.2	The Kibble Zurek Mechanism . . . . .	44
3.2.1	AIA Assumption . . . . .	44
3.2.2	Non-Equilibrium Universal Scaling . . . . .	46
3.2.3	Topological Defects and Their Relevance . . . . .	47
3.3	The Kibble Zurek Mechanism in $\phi^4$ Quantum Field Theory . . . . .	48
3.3.1	Universal Scaling in the $\phi^4$ theory . . . . .	48
3.3.2	Defect Ansatz for Quantum Phase Transitions . . . . .	49
<b>4</b>	<b>Hamiltonian Lattice Regularisation</b>	<b>53</b>
4.1	Introduction . . . . .	53
4.2	Hamiltonian Lattice Theory for $\phi^4$ . . . . .	54
4.2.1	The Lattice Hamiltonian and Effective Theory . . . . .	54
4.2.2	Continuum Limit . . . . .	55
4.2.3	Infrared Cutoff . . . . .	58
4.3	Lattice Approximation of Observables for $\phi^4$ . . . . .	59

---

4.3.1	The Ground State and One-Kink State . . . . .	59
4.3.2	The Scalar Mass and Long-Distance Behaviour of $G_2(r)$ . . . . .	60
4.3.3	Extracting $m_S$ at Strong Couplings . . . . .	61
4.4	Real-Space Fock Basis . . . . .	62
4.4.1	Creation and Annihilation Operators . . . . .	62
4.4.2	Boson Number Truncation . . . . .	63
4.5	Calculations in the Hamiltonian Lattice Framework . . . . .	65
<b>5</b>	<b>Tensor Network Representations</b>	<b>66</b>
5.1	Introduction . . . . .	66
5.2	Representation of The Lattice Hamiltonian as a Matrix Product Operator . . . . .	68
5.2.1	Matrix Product Operators . . . . .	68
5.2.2	MPO Representation of $\tilde{H}$ . . . . .	69
5.2.3	MPO as Tensor Networks . . . . .	71
5.3	Matrix Product State Representations . . . . .	72
5.3.1	Definition of MPS . . . . .	72
5.3.2	Entanglement in an MPS . . . . .	74
5.3.3	MPS Representation of Fixed Boson Number States and MPS-MPO products . . . . .	75
5.3.4	Uniform Matrix Product States . . . . .	78
5.4	Representation of Observables as Tensor Networks and Their Evaluation	78
5.4.1	Construction of Representation Using MPS and MPO . . . . .	78
5.4.2	Exact Contractions of Quasi-One-Dimensional TNR . . . . .	80
5.4.3	Expectation Values with uMPS . . . . .	81
5.4.4	Gauge Freedom of MPS and Boundary Conditions . . . . .	82
5.4.5	Low Entanglement Approximation of Higher Dimension Observables . . . . .	84

<b>6</b>	<b>Low Entanglement Approximations with Tensor Networks</b>	<b>85</b>
6.1	Introduction . . . . .	85
6.2	Matrix Product States as a Variational Ansatz . . . . .	87
6.3	Energy Minimisation Algorithm for MPS: vMPS . . . . .	88
6.4	Energy Minimisation Algorithm for uMPS: vuMPS . . . . .	90
6.5	Low Entanglement Approximations for the $\phi^4$ Theory . . . . .	92
<b>7</b>	<b>Studying the Kink in Equilibrium with MPS</b>	<b>95</b>
7.1	Introduction . . . . .	95
7.2	Field Expectation Values, Basis Truncation and Finite Entanglement Effects . . . . .	97
7.3	Particle Masses at Weak Coupling . . . . .	100
7.4	Strong Coupling: Universal Amplitude Ratio and Particle Masses . .	101
7.5	Conclusion . . . . .	104
<b>8</b>	<b>Time Evolution with Tensor Networks</b>	<b>105</b>
8.1	Introduction . . . . .	105
8.2	Non-Perturbative Methods for Non-Equilibrium QFT . . . . .	107
8.3	Variational Methods for Time Evolution . . . . .	109
8.4	Applying Matrix Product States to the Kibble Zurek Mechanism . . .	111
8.5	Time Dependent Variational Principle for uMPS . . . . .	112
<b>9</b>	<b>Studying the KZM with MPS</b>	<b>115</b>
9.1	Introduction . . . . .	115
9.2	Picking the Parameters for Time Evolution . . . . .	116
9.3	Time Evolution, Calculation of $G_2(k)$ and Time-Averaging . . . . .	118
9.4	Loss of Equilibrium . . . . .	120
9.5	Estimating the Defect Density . . . . .	121
9.6	Using The Defect Ansatz with Tensor Networks . . . . .	123
9.7	Universality of $G_2(k)$ with Defect Density . . . . .	124

9.8	Comparison of $\bar{G}_2(k)$ and $G_{\text{def}}(k)$ . . . . .	126
9.9	Conclusion . . . . .	127
<b>10</b>	<b>Conclusion</b>	<b>130</b>
	<b>Bibliography</b>	<b>132</b>



# List of Figures

1.1	A domain wall defect in the Classical 2D Ising Model. . . . .	23
2.1	The classical potential density $V(\phi)$ for $\mu_0^2 = -1, 1$ and $\lambda_0 = 0.5$ . . .	30
2.2	The classical kink solution $\varphi_K(x)$ for $\mu_0^2 = -1$ and $\lambda_0 = 0.5$ . . . . .	33
2.3	Scalar mass and kink mass for the $\phi^4$ theory as predicted by perturbation theory. . . . .	42
4.1	The perturbative phase diagram for the Hamiltonian Lattice Theory .	57
7.1	Matrix product state approximation of the $\phi^4$ ground state field expectation values for weak and strong couplings. . . . .	96
7.2	Matrix product state approximation of the $\phi^4$ kink field expectation values at weak and strong couplings. . . . .	98
7.3	Matrix product state approximation of the kink field-squared expectation value at weak and strong couplings. . . . .	100
7.4	Spatial average and variance of matrix product state approximations to the kink field expectation values. . . . .	101
7.5	Comparison of the matrix product state approximations to the kink mass and scalar mass at weak couplings. . . . .	102
7.6	Comparison of the matrix product state approximations to the kink mass and scalar mass at strong couplings. . . . .	103

9.1	Illustration of regions of interest for non-equilibrium calculations using matrix product state approximations to the scalar mass and kink mass . . . . .	117
9.2	Evolution of two-point function at zero momentum approximated using matrix product states (MPS) and the time dependent variational principle (TDVP). . . . .	118
9.3	Plots showing the error in the MPS approximation of $G_2(k)$ due to finite bond-dimension and boson number truncation . . . . .	119
9.4	Comparison of the time evolution of two-point function at zero momentum $G_2(k = 0)$ with prediction of Kibble-Zurek mechanism (KZM) prior to the critical point . . . . .	121
9.5	Comparison of defect density estimate using MPS and the TDVP with the KZM scaling prediction. . . . .	122
9.6	Comparison of the non-equilibrium two-point function $G_2(k)$ , approximated with MPS and TDVP, and the defect ansatz $G_{\text{def}}(k)$ . . . . .	125
9.7	Comparison between the non-equilibrium two-point function and ground state two-point function approximated with MPS. . . . .	127
9.8	Comparison between the non-equilibrium two-point function and the defect ansatz over full momentum range. . . . .	128

# List of Tables

2.1	Table of critical exponents for the $\phi^4$ theory . . . . .	41
-----	---	----



# Preface

## Thesis Intention

In this thesis, I summarise the key results of the Engineering and Physical Sciences Research Council (EPSRC) funded research project “Defect Formation in Quantum Phase Transitions” conducted by the author and supervised by Arttu Rajantie. The presentation is intended to be self-contained and includes an introduction to the concepts and methods used during the project. The main results of the project are outlined in two separate chapters, 7 and 9. These follow the work published in

1. Gillman, E., Rajantie A. (2017). “*Topological Defects in Quantum Field Theory with Matrix Product States.*” *Phys. Rev. D*, 96:094509, 2017. *arXiv:1705.09802*

and

2. Gillman, E., Rajantie A. (2017) .“The Kibble Zurek Mechanism of Topological Defect Formation in Quantum Field Theory with Matrix Product States.” *preprint*, arXiv:1711.10452. Accepted for publication in *Phys. Rev. D*.

respectively, which constitute the key outcomes of the project for which the author was the primary researcher.

## Context and Motivation

Currently, there is no well-developed general method for performing non-equilibrium quantum field theory calculations non-perturbatively. Access to such a technique would open up significant new areas for study within theoretical high energy physics and cosmology making the development of potential methods extremely appealing.

In one spatial dimension, tensor network methods have emerged as a dominant non-perturbative technique within quantum many body physics and condensed

matter theory. These techniques can be applied both to equilibrium scenarios (including finite fermion densities since they are free of the sign-problem) and to non-equilibrium scenarios, having been highly successful in both cases. Furthermore, they have been successfully applied to quantum field theories previously, including to the  $\phi^4$  theory in equilibrium [1] and in non-equilibrium Kibble-Zurek mechanism type scenarios [2].

The previous success of tensor network methods indicate they are a promising candidate for the study of non-equilibrium quantum field theory more generally. Topological defect formation via the Kibble-Zurek mechanism then provides a particularly interesting area of application since, in addition to being of interest in its own right, it is known to be challenging for non-equilibrium methods to capture, with some standard methods failing in this case [3]. Due to its generality, the Kibble-Zurek mechanism is expected to hold so that topological defect formation functions as an excellent benchmark for potential non-perturbative non-equilibrium methods. Since topological defect formation has a non-trivial realisation in  $D = (1 + 1)$  in the  $\phi^4$  scalar field theory, it is particularly good as a test for tensor network techniques.

Finally, there is at present significant interest in developing tensor network techniques in higher dimensions as well as to Abelian and non-Abelian gauge theories. Therefore, this is an ideal time to also develop them as non-equilibrium quantum field theory methods with the hope that they can one day simulate realistic theories in high energy physics and cosmology.

## Aims

The first main aim of this thesis is to provide evidence for the validity of the Kibble Zurek mechanism of topological defect formation, in the case of a quantum field theory undergoing a quantum phase transition (QPT). To achieve this, we study the  $\phi^4$  scalar field theory in  $D = (1 + 1)$  spacetime dimensions. We then consider a non-equilibrium scenario that should, according to the Kibble-Zurek mechanism, lead to topological defect formation and compare the results of our calculations against these expectations.

The second main aim of the thesis is to benchmark and develop the use of tensor network techniques as a non-perturbative non-equilibrium method for quantum field theory. This is achieved by applying tensor network methods to the study of the kink defect in the  $\phi^4$  model in equilibrium, comparing to known analytic results, and by performing the non-equilibrium calculations needed to study the Kibble-Zurek

mechanism in this theory.

## Results and Basis for Future Research

We use the matrix product state and related tensor network techniques to study the  $\phi^4$  kink defect both in equilibrium and out of equilibrium in the Kibble-Zurek mechanism scenario. In the equilibrium case, we show that matrix product states and tensor networks can be used to capture the physics of kink defects comparing with analytic results for the kink mass at both weak and strong couplings. Out of equilibrium, we find that the two-point function computed using tensor network methods is consistent with expectations from the Kibble-Zurek mechanism of topological defect formation. In addition to these main results, we develop strategies and methods for the application of tensor networks to quantum field theory and topological defects that can be applied more broadly than the specific theory considered here. The results of this work suggest that tensor networks are indeed a promising method for non-equilibrium quantum field theory calculations.

The results of this project can be adapted and built on with applications to more sophisticated theories, in parallel with the development of tensor network techniques more generally.

# Chapter 1

## Introduction

### 1.1 Topological Defects and Their Formation

#### 1.1.1 Topological Defects

The existence of topological defects is a highly generic phenomenon found in condensed matter systems, for example liquid crystals [4] and superfluids [5], and proposed in high energy scenarios such as cosmology [6] and beyond standard model theories [7].

Intuitively, a topological defect can be thought of as a discontinuity in an otherwise ordered system, typically at the interface between ordered domains, that cannot be removed by local changes. Some of the most intuitive examples of topological defects are found in classical spin systems [8]. For example, the classical Ising model has topological defects known as domain walls which separate uniform domains of spins as illustrated in Figure 1.1. In the two-dimensional case shown, the wall defect is line-like (one-dimensional) and, in  $D_S$  spatial dimensions, such a defect will in general be of dimension  $D_{\text{def}} = D_S - 1$  i.e. of codimension  $D_{\text{co}} = D_S - D_{\text{def}} = 1$ . The relationship with topology comes from the fact that local changes such as single spin flips cannot remove such a defect from the system for given boundary conditions. Rather, a global change to the configuration is required - all spins in a domain must be flipped - and such defects can be considered topologically stable for this reason.

The physical importance of defects lies in the fact that they can be formed quite generically during the process of symmetry breaking and are typically very long lived relative to other excitations. Once formed, they are then highly relevant for the subsequent physics in the system of interest.

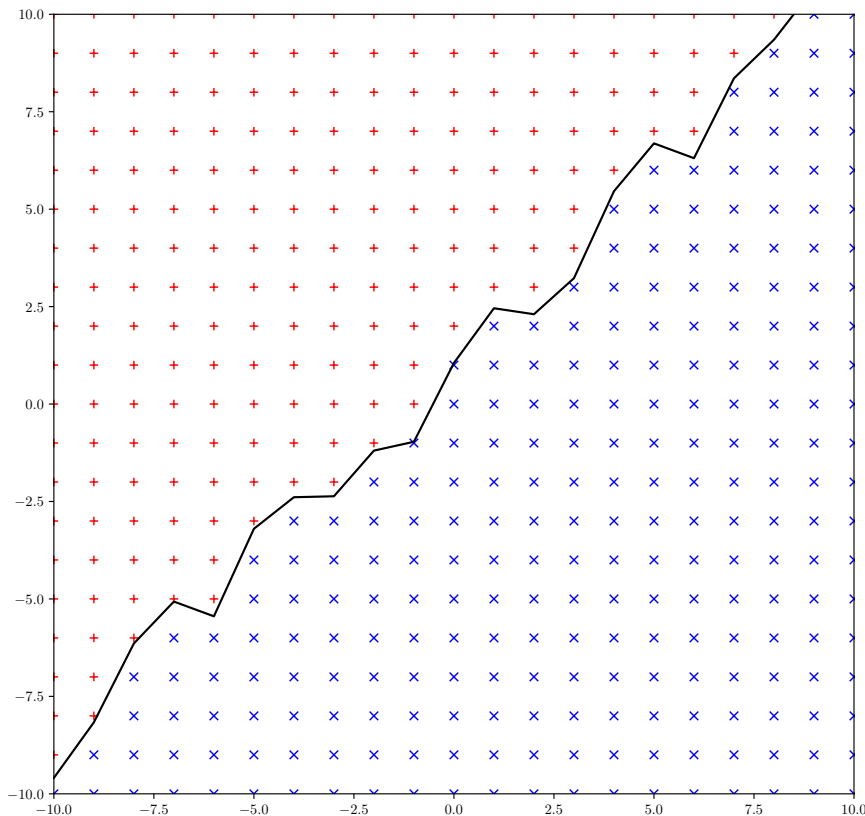


Figure 1.1: The domain wall (solid black line) is a defect that separates uniform regions of spins (red pluses and blue crosses). The defect is topologically stable since local spin-flips can only shift the domain-wall and a global change to the system which flips all the spins in one of the two domains is required to remove it.

### 1.1.2 The Formation of Topological Defects and Symmetry Breaking

The formation of defects can occur during phase transitions characterised by the breaking of symmetry [7]. The case of global symmetry breaking in continuous phase transitions is described by the Kibble-Zurek mechanism (KZM). The KZM combines the work of Kibble, who considered the formation of defects in cosmology [9], with that of Zurek in condensed matter systems [10]. Initially, Kibble observed that the process of any realistic continuous phase transition is in fact a non-equilibrium process where topological defects are formed, assuming they can exist in the system in the first place. Zurek then developed this idea and argued that, despite equilibrium being lost during a continuous phase transition, the process is nonetheless universal. The key prediction of the KZM is then that the density of topological defects  $n$  in a system following an appropriate symmetry breaking phase transition has a universal

scaling. The scaling is determined by the equilibrium critical exponents  $\nu$  and  $\mu$ , associated with the spatial and temporal correlation lengths, along with the quench rate  $\tau_Q$  - a dynamical scale that characterises the rate of the phase transition. The KZM prediction for the defect density  $n$  in the post-transition state is

$$n \sim \tau_Q^{-D_{\text{co}} \frac{\nu}{1+\mu}}, \quad (1.1)$$

where  $D_{\text{co}}$  is the codimension of the defect.

While the KZM constitutes a generic description of a continuous symmetry breaking phase transition and predicts the universal scaling of a number of related quantities, the uncommonly long lifetimes of defects make the scaling (1.1) particularly important. Even long after other excitations have equilibrated and the universal information encoded in their distribution has been lost, details of the phase transition will still be present in the distribution of topological defects. For this reason, topological defects are often described as “fossilised evidence” of the phase transition. This is especially important since confirmation of the KZM can be challenging both experimentally and theoretically as it requires the measurement of quantities within a non-equilibrium scenario over a wide range of parameters (quench rates). As such, having a measurement that can be performed even sometime after the transition has ended is essential and this makes the scaling of the defect density the key testable prediction of the KZM.

### 1.1.3 The Kibble-Zurek Mechanism in Quantum Theory

The universal scaling (1.1) predicted by the Kibble Zurek Mechanism has been confirmed experimentally in a wide variety of systems. There is also significant theoretical evidence for its validity within classical systems and quantum systems where a classical-statistical approximation is valid such as those at sufficiently high temperatures or occupation numbers, see e.g. the reviews [11, 7].

In the case of zero-temperature quantum phase transitions (QPT), thermal fluctuations are absent and cannot dominate dynamics. The understanding of out of equilibrium physics in this case then requires a truly quantum picture, making confirmation of the KZM more challenging. On the one hand, the necessary non-equilibrium calculations are even more difficult in the quantum case. On the other, it may not be clear how to pick an appropriate observable to estimate the defect density in the first place. Nonetheless, in the special case of integrable quantum lattice theories such as the quantum Ising model, it is possible to confirm the KZM

prediction (1.1) exactly [12, 13] for two key reasons. Firstly, the unitary quantum dynamics though the QPT can be computed analytically. Secondly, topological defects can be identified explicitly which allows for the construction of exact defect counting operators. Of course, such analytic calculations and constructions are not possible in non-integrable theories. Some aspects of the KZM have still been confirmed by studying other scaling predictions such as the variance of winding numbers using mean field theory [14], quasi-particle excitations densities and the evolution of initial perturbations into domains [15]. However, such observables may well be unrelated to the defect density [16] and the question of topological defect formation remains.

In the case of quantum field theory (QFT), the question of choosing an appropriate observable to estimate the defect density becomes even more important since observables that are UV sensitive, such as those that perform explicit counting in the lattice case, are ruled out. A more suitable observable for QFT was suggested in [17] where it was shown that in the classical statistical  $\phi^4$  theory, the two-point function could be used to extract a well behaved long-distance estimate of the defect density in addition to providing an explicit signature of defects. However, confirming this suggestion still requires a non-equilibrium quantum field theory calculation of defect formation, which has proven challenging for standard, otherwise successful methods [3, 18].

To summarise, theoretical confirmation of the KZM and defect formation in the case of a QFT undergoing a quantum phase transition remains unclear. However, the generality and substantial evidence for the KZM in other cases strongly suggests its validity. What is then lacking are the necessary calculation tools with the difficulty of capturing defect formation in QFT suggesting that a truly non-perturbative non-equilibrium method is required. The KZM and defect formation can then be viewed not only as a phenomena of significant interest in its own right, but a powerful benchmark for any potential non-perturbative non-equilibrium QFT methods, of which there are no well-developed examples at present.

## 1.2 Thesis Outline

In this thesis, we first provide an introduction to topological defects in the  $\phi^4$  theory in Chapter 2 and an outline of the Kibble Zurek mechanism and defect formation in Chapter 3. In Chapter 4 we outline the Hamiltonian lattice regularisation, which allows standard quantum many body physics techniques to be applied to the

study of quantum field theories. In Chapter 5 we introduce the concept of tensor networks and in Chapter 6 outline some relevant methods for their use in approximations. These ideas are applied in Chapter 7 to the study of the  $\phi^4$  kink defect in equilibrium, where the tensor network approximations are compared to known perturbative and universal results. Chapter 8 introduces the application of tensor networks to non-equilibrium problems and discusses some other non-equilibrium quantum field theory methods for comparison. These are then applied to the problem of defect formation in Chapter 9 before concluding in Chapter 10

# Chapter 2

## Topological Defects

### 2.1 Introduction

In classical field theory, field configurations  $\phi(x)$  can be classified into *topological sectors* so that configurations lying in different sectors cannot be continuously deformed into one another. Since time evolution is a form of continuous deformation, the existence of multiple topological sectors corresponds to the existence of a conserved *topological charge*  $Q_{\text{top}}$ . Thus, the topology of the theory, as specified by the homotopy classes of field configurations, results in a conserved charge which is not related to the symmetries of the system through Noether's theorem.

The topological sector that contains the minimum energy solution to the equations of motion  $\varphi_v(x)$  is called the vacuum sector and given  $Q_{\text{top}} = 0$ . A topological defect or topological soliton (which we will use synonymously) is then a static (time-independent) solution to the equations to motion that lies outside the vacuum sector, i.e.  $Q_{\text{top}} \neq 0$ , and is of minimum energy within that sector so that it is stable.

In a quantum field theory, one can extend the concept of topological sectors by introducing a Hermitian topological charge operator  $\hat{Q}_{\text{top}}$  which commutes with the Hamiltonian  $[\hat{H}, \hat{Q}_{\text{top}}] = 0$  and partitions the physical states of the theory according to a superselection rule [19]. The vacuum sector, which contains the ground-state, is labelled by  $Q_{\text{top}} = 0$  and a topological defect is then a minimum energy state within a sector with  $Q_{\text{top}} \neq 0$ . Since they lie in a different sector to the vacuum, these objects cannot be reached by standard perturbation theory and one must turn to other methods such as semi-classical expansions starting from the classical defect configurations or non-perturbative methods such as lattice theory.

In this thesis, we will focus on one of the simplest examples of a topological defect, the kink defect of the  $\phi^4$  theory in  $D = (1 + 1)$ . This defect is particularly

interesting since an explicit classical form can be found for it, it is zero-dimensional and so appears like a particle in the classical theory and the corresponding topological charge can be defined in terms of a choice of boundary conditions which allows the defect to be studied in the quantum theory using non-perturbative lattice methods.

In this chapter, we will first introduce the classical  $\phi^4$  theory and the kink defect. Second, we will introduce the corresponding quantum theory before reviewing the results obtained for the quantum kink using semi-classical methods and universality arguments.

## 2.2 Topological Defects in Classical Field Theory

### 2.2.1 Action, Energy Functional and Equations of Motion

The classical  $\phi^4$  theory in  $D = (1 + 1)$  provides one of the simplest examples of topological defects in a field theory. The theory can be defined by the action

$$S[\phi] = \int dxdt \left[ \frac{1}{2}(\partial_t\phi)^2 - \frac{1}{2}(\partial_x\phi)^2 - \frac{\mu_0^2}{2}\phi^2 - \frac{\lambda_0}{4!}\phi^4 \right], \quad (2.1)$$

where we will set  $\lambda_0 > 0$  but allow  $\mu_0^2$  to take on negative values. The corresponding energy functional is given by

$$\begin{aligned} E[\phi] &= \int dx \left[ \frac{1}{2}(\partial_t\phi)^2 + \frac{1}{2}(\partial_x\phi)^2 + \frac{\mu_0^2}{2}\phi^2 + \frac{\lambda_0}{4!}\phi^4 \right] \\ &= \int \left[ \frac{1}{2}(\partial_t\phi)^2 + \frac{1}{2}(\partial_x\phi)^2 + V(\phi) \right] dx \\ &= \int \left[ \frac{1}{2}(\partial_t\phi)^2 \right] dx + U[\phi], \end{aligned} \quad (2.2)$$

where  $V(\phi)$  is the potential density and  $U[\phi]$  is the potential energy, which includes the contribution of the spatial gradient energy.

Physical field configurations  $\varphi(t, x)$  correspond to stationary points of the action with fixed boundary conditions and solve the equations of motion (EOM) given by the Euler Lagrange equations

$$\square\phi = -\mu_0^2\phi - \frac{\lambda_0}{3!}\phi^3, \quad (2.3)$$

where  $\square = \partial^\mu\partial_\mu = \partial_t^2 - \partial_x^2$ . Static solutions with  $\partial_t\varphi(t, x) = 0$  are given by

stationary points of the potential energy  $U[\phi]$  while stable solutions are given by the local minima.

### 2.2.2 Classical Vacua, Elementary Particles and Phase Transition

In addition to the spacetime Poincaré symmetry, the action (2.1) has an internal global  $\mathbb{Z}_2$  symmetry given by the group  $\mathbb{G} = \mathbb{Z}_2 = \{e, g\}$ . The action of the non-trivial element  $g$  is given by  $g : \phi(x) \rightarrow -\phi(x)$  and leaves the action (2.1) invariant as  $S[\phi] \rightarrow S[-\phi] = S[\phi]$ .

The minimum energy solutions of the equations of motion  $\varphi_\Omega$  are known as the vacua and can be identified by minima of the potential density, see Figure 2.1. When  $\mu_0^2 > 0$ , there is a unique solution  $\varphi_\Omega = \varphi_0 = 0$  which minimises the energy (2.2). The solution  $\varphi_0$  is spatially uniform and  $\mathbb{Z}_2$  symmetric such that  $g : \varphi_0 \rightarrow \varphi_0$ . However, when  $\mu_0^2 < 0$ , there are two degenerate minimum energy solutions  $\varphi_\pm = \pm \sqrt{\frac{-6\mu_0^2}{\lambda_0}} = \pm v$ . The solutions are still spatially uniform but form an antisymmetric  $\mathbb{Z}_2$  pair as  $g : \varphi_\pm \rightarrow -\varphi_\pm = \varphi_\mp$ . This is an example of a continuous symmetry breaking phase transition where the stable  $\varphi_0$  solution becomes unstable for  $\mu_0^2 < 0$  and perturbations will lead to spontaneous symmetry breaking down to the stable, antisymmetric solutions  $\varphi_\pm$ . In the present case, the location of the critical point is given by  $\mu_0^2 = 0$  for all  $\lambda_0$ , though more generally the critical point is located at some non-zero  $\mu_0^2 = m_C^2$ . The distance from the critical point can be characterised by  $\epsilon = \mu_0^2 - m_C^2$  for a given  $\lambda_0$  so that the symmetric (disordered) phase with  $\epsilon > 0$ , is separated from the symmetry broken (ordered) phase with  $\epsilon < 0$  by the critical point where  $\epsilon = 0$ .

The classical elementary (scalar) particles in the  $\phi^4$  theory can be considered as small linearised excitations about the minimum energy configuration. The action of these excitations can be found by expanding about a chosen vacuum as  $\phi = \varphi_\Omega + \delta\phi$ . In the symmetric phase with  $\mu_0^2 > 0$  the minimum energy configuration is  $\varphi_0 = 0$  such that  $\phi = \delta\phi$  and the particle mass  $m_S$  is given by the usual quadratic coefficient  $m_S = \mu_0 = \sqrt{|\mu_0^2|}$ . In the symmetry broken phase, the classical action (2.1) can be expanded as  $\phi = \pm v + \delta\phi$  so that for  $+v$

$$S[\delta\phi] = \int dxdt \left[ \frac{1}{2}(\partial_t \delta\phi)^2 - \frac{1}{2}(\partial_x \delta\phi)^2 - \frac{|2\mu_0^2|}{2} \delta\phi^2 - \sqrt{\frac{\lambda_0 |\mu_0^2|}{6}} \delta\phi^3 - \frac{\lambda_0}{4!} \delta\phi^4 + V(v) \right], \quad (2.4)$$

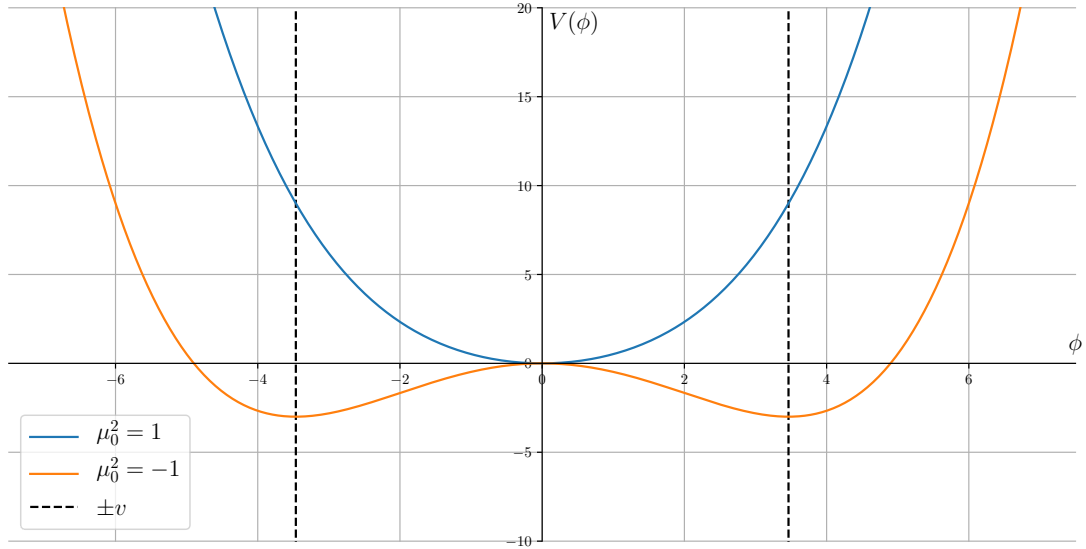


Figure 2.1: The classical potential density  $V(\phi)$  (2.2) with  $\mu_0^2 = -1, 1$  and  $\lambda_0 = 0.5$ . For  $\mu_0^2 > 0$  there is a single minimum corresponding to a unique vacuum solution  $\varphi_0 = 0$  while for  $\mu_0^2 < 0$  there are two global minima corresponding to the degenerate vacua  $\varphi_{\pm} = \pm v = \pm\sqrt{\frac{-6\mu_0^2}{\lambda_0}}$ .

and the classical particle mass is found via the coefficient of the quadratic term  $\delta\phi^2$  such that  $m_S = \sqrt{2}\mu_0$ .

### 2.2.3 Topological Charge and Sectors

The topological charge for the classical  $\phi^4$  theory can be introduced in the symmetry broken phase by considering the necessary criteria for a given field configuration to have finite energy. It is easy to see that such configurations must necessarily fall off to a vacuum configuration as  $x \rightarrow \pm\infty$  i.e.  $\phi(x) \rightarrow \pm v$  as  $x \rightarrow \pm\infty$ . Therefore, there are four possible boundary conditions for finite energy field configurations and these can be given an integer charge

$$Q_{\text{top}} = \frac{1}{2v} (\phi(\infty) - \phi(-\infty)) . \quad (2.5)$$

This charge is necessarily conserved since no finite energy process can change the disconnected boundary conditions. The corresponding conserved current is given by

$$j^\mu = \frac{1}{2v} \epsilon^{\mu\nu} \partial_\nu \phi , \quad (2.6)$$

where  $\epsilon^{\mu\nu}$  is the Levi-Civita symbol. Generally, since no continuous deformation can occur at the boundary without leaving the set of finite energy configurations, the charge  $Q_{\text{top}}$  is indeed a topological charge for the theory and partitions the set of finite energy configurations into topological sectors. Configurations that fall off to the same vacuum configuration (including the vacua themselves) have  $Q_{\text{top}} = 0$  and are topologically trivial, while those falling to distinct vacua have  $Q_{\text{top}} = \pm 1$  and are topologically non-trivial.

### 2.2.4 Topological Charge and Sectors in Classical Field Theory: A General Analysis

While it is quite intuitive in the  $\phi^4$  case that the charge (2.5) defined on the boundary corresponds to a topological charge for the theory, in general situations the existence of multiple topological sectors is less obvious. However, there is a powerful general analysis that can be used to determine the presence of non-trivial topological charges in classical field theory [20]. While the mathematical details of this analysis can be somewhat subtle, the basic idea is quite intuitive and we will outline it here.

The separation of a theory into topological sectors can be established quite generally by examining the symmetries of the theory along with the topology of the vacuum manifold  $\mathcal{M}$  i.e. the set of physically distinct minimum energy field configurations. To achieve this, consider a theory with a symmetry group  $\mathbb{G}$  such that the action of its elements on field configurations  $g : \phi \rightarrow \phi^g$  leaves the energy functional invariant  $E[\phi] = E[\phi^g]$ . Given a configuration  $\phi_0$  that minimises  $E[\phi]$  this symmetry means that all configurations  $\phi_0^g$  will also minimise the energy. However, labelling the minimum energy configurations by the elements of  $\mathbb{G}$  can be redundant as there is always a subgroup  $\mathbb{H}$  (possibly trivial) that will leave the configuration  $\phi_0$  invariant i.e.  $\phi_0^h = \phi_0$  for all  $h \in \mathbb{H}$ . As such, the distinct minimum energy configurations are really labelled by the elements of the (left) coset  $g\mathbb{H}$  and the vacuum manifold is isomorphic to the coset space  $\mathcal{M} \simeq \mathbb{G}/\mathbb{H}$ .

With the vacuum manifold established, the topology of the vacuum manifold can be identified by considering the homotopy groups  $\pi_n(X)$ . The homotopy group  $\pi_n(X)$  can be defined by considering the set of maps  $f$  from the  $n$ -sphere  $S^n$  to the space  $X$ ,

$$f : S^n \rightarrow X, \quad (2.7)$$

that take a fixed point  $a$  (the base point) in  $S^n$  to a fixed point  $b$  in  $X$ . Introducing an equivalence relation such that all maps  $f$  that can be continuously deformed into one another fall into the same equivalence class, the elements of the homotopy group  $\pi_n(X)$  are given by representatives of these equivalence classes.

Finite energy field configurations can then be partitioned into topological sectors by considering them as maps at infinity from  $S_\infty^n$  to the vacuum manifold  $\mathcal{M}$ . It can then be shown that configurations that are topologically non-trivial on the boundary  $S_\infty^n$  cannot be continuously deformed into topologically trivial configurations. This means that such configurations necessarily have a non-zero energy density somewhere in the interior which we associate to the existence of a topological defect. For the homotopy classes with  $n = 0, 1, 2$  and  $3$  the corresponding defects have codimension  $D_{\text{co}} = n + 1$  and are known as domain walls, strings, monopoles and textures respectively.

In cases where the vacuum manifold consists of disconnected parts, then the homotopy group  $\pi_0(\mathcal{M})$  is non-trivial and domain walls (kinks in  $D = (1 + 1)$ ) must occur. The  $\phi^4$  theory then falls into this category with  $\mathbb{G} = \mathbb{Z}_2$ ,  $\mathbb{H} = \mathbb{1}$  such that  $\mathcal{M} = \mathbb{G}/\mathbb{H} = \mathbb{Z}_2$  and  $\pi_0(\mathbb{Z}_2) = \mathbb{Z}_2$ . Therefore, for a fixed boundary point e.g.  $\phi(+\infty) = v$ , the  $\phi^4$  theory has two topological sectors corresponding to the topologically trivial vacuum sector and the non-trivial kink sector. Of course, showing the existence of topological sectors does not guarantee that one can explicitly find solutions to the equations of motion within these sectors, nor that any solutions found will be the minimum energy configurations within these sectors and therefore stable, though this is indeed possible in the  $\phi^4$  case.

### 2.2.5 Kink Defects in $\phi^4$

With the existence of a topological charge and non-trivial topological sectors established, we would now like to find explicit forms for the topological defects i.e. find the minimum energy solutions to the equations of motion with  $Q_{\text{top}} \neq 0$ . For the  $\phi^4$  theory the topological defect solutions  $\varphi_K(x)$  with  $Q_{\text{top}} = 1$  are known as kinks and can be found explicitly to give

$$\varphi_K(x) = v \tanh \left( \frac{\mu_0 (x - x_0)}{\sqrt{2}} \right), \quad (2.8)$$

with the corresponding antikink for  $Q_{\text{top}} = -1$  given by  $-\varphi_K(x)$ .

The kink solution (2.8) has several important features that are characteristic of topological defects. Firstly, as can be seen in Figure 2.2, it is a solution that

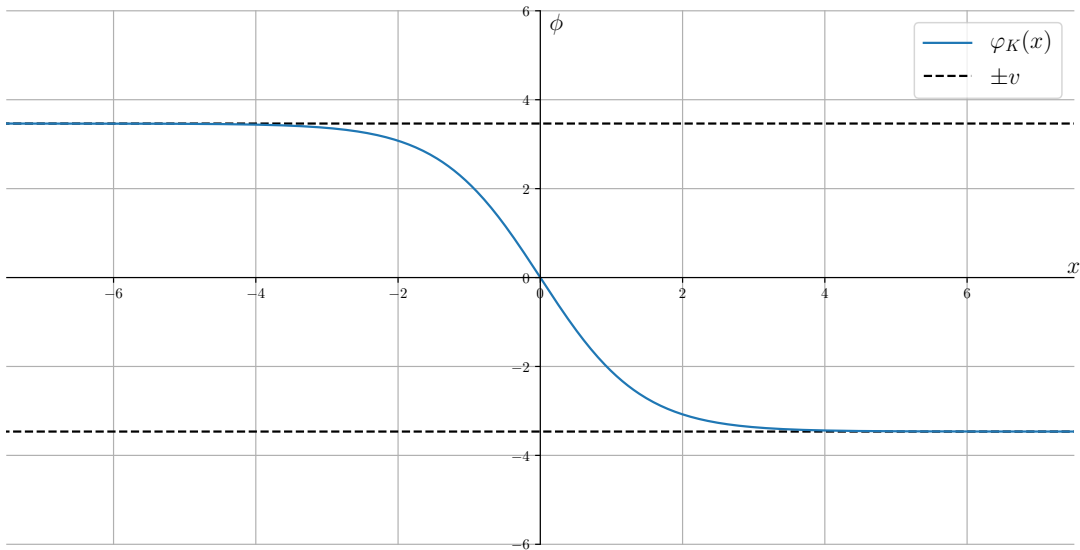


Figure 2.2: The classical kink solution  $\varphi_K(x)$  (2.8) for  $\mu_0^2 = -1$ ,  $\lambda_0 = 0.5$  and  $x_0 = 0$ . The solution interpolates between the two degenerate symmetry broken vacua  $\pm v$ . The “kink width”  $d_K = \sqrt{-2/\mu_0^2}$  characterises the scale over which the kink has a non-zero spatial gradient and, correspondingly, a non-zero energy density relative to the vacua.

smoothly interpolates between two different minimum energy solutions  $\pm v$  as  $x \rightarrow \pm\infty$ . Secondly, the solution has a degree of freedom  $x_0$  known as a zero-mode that determines the point at which the kink crosses the  $x$ -axis. The kink solution (2.8) is then in fact a continuous one-parameter family of solutions labelled by  $x_0$ . Thirdly, the kink solution has a non-zero size characterised by the length scale (which we will call the kink-width)  $d_K = \sqrt{2}/\mu_0$ . This length scale characterises the size of the localised energy density of the kink solution so that, in this way, the kink appears like a classical particle. However, there are important differences with the elementary excitations that we would consider as particles due to their association with particles in a quantum theory. In particular, while finite size seems like a natural thing to associate to a classical particle, the elementary excitations that are associated to particles in the quantum theory have no such size and are considered infinitesimal. Additionally, the kink solution is a non-linear solution to the full equations of motion while the elementary excitations are instead solutions to the linearised equations of motion. In this sense, the kink solutions are naturally non-perturbative objects while the elementary excitations are naturally perturbative.

The kink mass  $M_K$ , i.e. its energy above a vacuum state, is finite due to its localised energy density. Integrating the energy density and subtracting the vacuum

energy gives

$$M_K = 4\sqrt{2} \frac{|\mu_0|^3}{\lambda_0}, \quad (2.9)$$

where the  $\mathcal{O}(\mu_0^3)$  scaling means that the kinks are generally very heavy relative to the scalar excitations with  $m_S = \sqrt{2}\mu_0$ .

## 2.3 Topological Defects in Quantum Theory

### 2.3.1 Hamiltonian and Field Eigenbasis

The continuum Hamiltonian for the  $\phi^4$  quantum field theory in  $D = (1 + 1)$  can be written in the Schrödinger picture as

$$H[\phi] = \int dx \left[ \frac{1}{2}\pi^2(x) + \frac{1}{2}(\partial_x\phi)^2(x) + \frac{\mu_0^2}{2}\phi^2(x) + \frac{\lambda_0}{4!}\phi^4(x) \right]. \quad (2.10)$$

The field operators  $\phi(x)$  and  $\pi(x)$  obey the canonical commutation relations

$$[\phi(x), \pi(y)] = i\delta(x - y) \quad (2.11)$$

and the  $\phi(x)$  field is dimensionless,  $[\phi] = 0$ , where the square brackets indicate the mass dimensions of the enclosed object. The  $\pi(x)$  field is dimensionful with  $[\pi] = +1$  as are the parameters with  $[\mu_0^2] = +2$  and  $[\lambda_0] = +2$ . In  $D = (1 + 1)$  the  $\phi^4$  theory then has a single dimensionless bare parameter given by the ratio  $g_0 = \lambda_0/\mu_0^2$ . Additionally, only mass renormalisation is required so that the (dimensionless) effective coupling  $g$ , which determines the validity of perturbative expansions and is related to the scattering cross-section, can be parametrised using the bare parameter  $\lambda_0$  along with the physical scalar mass  $m_S$  such that we can set  $g = \lambda_0/m_S^2$ .

The field eigenstates  $|\Phi(x)\rangle$ , given by  $\phi(x)|\Phi(x)\rangle = \Phi(x)|\Phi(x)\rangle$ , can be used as basis for the QFT [21] with a general state  $|\psi\rangle$  being expanded as

$$|\psi\rangle = \int \mathcal{D}[\Phi(x)] \psi[\Phi(x)] |\Phi(x)\rangle, \quad (2.12)$$

where  $\mathcal{D}[\Phi(x)]$  indicates an integral over all (spatial) field configurations  $\Phi(x)$  and  $\psi[\Phi(x)]$  is known as the wavefunctional for the state, though we will use wavefunction interchangeably.

### 2.3.2 Vacua, Particles and Symmetry Breaking

As for the classical theory, the Hamiltonian (2.10) has an internal global  $\mathbb{Z}_2$  symmetry and displays a continuous symmetry breaking quantum phase transition (QPT) [22]. In the broken symmetry phase, the theory has degenerate vacuum states that have field expectation values (vacuum expectation values or vev) that are related by the non-trivial  $\mathbb{Z}_2$  symmetry transformation. Since symmetric superpositions of the symmetry broken vacuum states are unstable against symmetry breaking perturbations, the physical vacuum/ground states (which we use interchangeably) can be considered the antisymmetric states [23].

In the case of finite spatial volume, due to the presence of instantons (tunnelling), the ground state of the theory is  $\mathbb{Z}_2$  symmetric even within the symmetry broken phase [24]. Nonetheless, the different phases of the quantum theory can be distinguished in the ground state by the presence of long range order in the equal time field two-point function

$$G_2(r) = \langle \Omega | \phi(x) \phi(x+r) | \Omega \rangle . \quad (2.13)$$

In the disordered phase  $G_2(r)$  decays exponentially at asymptotic distances,

$$G_2(r) \sim e^{-\frac{r}{\xi}} \text{ as } r \rightarrow \infty , \quad (2.14)$$

which defines the correlation length  $\xi$ . In contrast, in the ordered phase  $G_2(r)$  displays long range order and tends to a constant as :

$$G_2(r) \sim v^2 \text{ as } r \rightarrow \infty . \quad (2.15)$$

At the critical point, the theory has a diverging correlation length which scales universally as

$$\xi \approx \xi_0 |\epsilon|^{-\nu} \quad \epsilon > 0 , \quad (2.16)$$

$$\xi \approx \xi'_0 |\epsilon|^{-\nu'} \quad \epsilon < 0 , \quad (2.17)$$

where  $\epsilon$  is some reduced coupling and  $\epsilon = 0$  characterises the critical point. Due to Lorentz invariance of the theory, the correlation length is equal to the inverse mass gap  $\Delta$  which is the mass of the elementary scalar particle,  $\Delta = m_S = \xi^{-1}$ , so that the critical point is characterised by the condition  $m_S \rightarrow 0$ . The dynamical critical exponent  $\mu$  can be defined similarly to  $\nu$ , by the critical scaling of the unequal time

two-point function,  $G_2(t) = \langle \Omega | \phi(x, t) \phi(x, 0) | \Omega \rangle$  [25], and can also be expressed as  $\mu = z\nu$  so that  $z = 1$  due to Lorentz Invariance.

In  $D = (1 + 1)$ , there are two possible universality classes. If the effective coupling  $g$  is kept finite as  $m_S \rightarrow 0$ , by letting  $\lambda_0 \rightarrow 0$ , the theory lies close to a Gaussian fixed point where the critical point is described by a massless Gaussian theory. In the vicinity of this critical point, assuming  $g < 1$ , perturbation theory can be applied about the Gaussian theory and the symmetry breaking phase transition can be understood perturbatively. In this case, in the symmetric phase, the scalar mass can be related to the bare parameters via renormalised perturbation theory [26] to give

$$\mu_0^2 = m_S^2 - \frac{1}{8\pi} \log \left( \frac{64}{m_S^2 a^2} \right) + \mathcal{O}(\lambda_0^2), \quad (2.18)$$

where a spatial lattice with spacing  $a$  provides the UV regularisation. When  $m_S \rightarrow 0$  this expression is infrared divergent and perturbation theory will break down requiring resummation. Nevertheless, we can get a rough estimate for the critical behaviour by retaining only the  $m_S^2$  independent one-loop terms so that

$$m_S^2 = \mu_0^2 + \frac{\lambda_0}{8\pi} \log(64). \quad (2.19)$$

Approaching the critical point by keeping  $\lambda_0$  fixed such that  $\epsilon \sim \mu_0^2 - m_C^2$ , then, since  $\epsilon \sim \mu_0^2 \sim m_S^2$ , the classical/mean-field critical scaling is given by  $\epsilon \sim \xi^{-2}$  i.e.  $\nu_{\text{MF}} = 1/2$ . The location of the critical bare mass  $m_C^2$  can be also be estimated using (2.19) by setting  $m_S^2 = 0$  so that

$$m_C^2(\lambda_0) = -\frac{\lambda_0}{8\pi} \log(64). \quad (2.20)$$

If  $\lambda_0$  is kept finite as  $m_S \rightarrow 0$ , rather than taking  $\lambda_0 \rightarrow 0$ , the effective coupling  $g$  diverges and the Wilson-Fisher fixed point is approached. In this case, at the (strong-coupling) critical point the theory is not equivalent to a Gaussian scalar theory and so standard perturbation theory cannot be applied in its vicinity. Instead, the critical theory is one of massless fermions [27] and falls into the classical  $D = 2$  Ising universality class. The critical exponents for this class are [28]

$$\begin{aligned} \nu &= 1, \\ \mu &= \nu, \\ \nu' &= \nu, \end{aligned} \quad (2.21)$$

where the second line follows from Lorentz invariance and the third line is the hyperscaling relation for the universality class.

### 2.3.3 Topological Charge and Sectors

A topological charge operator for the  $\phi^4$  theory can be introduced by direct analogy with the classical one [19] such that

$$\begin{aligned}\hat{Q}_{\text{top}} &= \frac{1}{2v_{cl}} \int_{-\infty}^{\infty} \partial_x \phi \, dx , \\ &= \frac{1}{2} \sqrt{\frac{\lambda_0}{-6\mu_0^2}} (\phi(+\infty) - \phi(-\infty)) .\end{aligned}\quad (2.22)$$

This operator is Hermitian and commutes with the Hamiltonian so that the corresponding charge is conserved under time evolution. Furthermore, it separates the theory into topological sectors according to a superselection rule [29]. In QFT, the physical observables are those that are (quasi) local and causality requires that physical observables are encoded in operators  $A$  that commute at spacelike separations. Since the charge  $\hat{Q}_{\text{top}}$  is defined on the boundary of the theory, it then must commute with all physical operators: If an operator  $A(t) = \int dx a(x, t)$  where  $a(x, t)$  has finite spatial support for all  $t$ , then the commutator at any given time  $t$ ,

$$\left[ A(t), \hat{Q}_{\text{top}} \right] = \lim_{L \rightarrow \infty} \int dx ([a(x, t), \phi(+L)] - [a(x, t), \phi(-L)]) \rightarrow 0 \quad (2.23)$$

by causality. The topological charge  $\hat{Q}_{\text{top}}$  therefore introduces a superselection rule since, for states with definite charge  $|\psi, Q_{\text{top}}\rangle$ ,

$$\langle \psi', Q_{\text{top}}' | A(t) | \psi, Q_{\text{top}} \rangle = 0 \quad \text{if } Q_{\text{top}} \neq Q_{\text{top}}' \quad (2.24)$$

for all physical operators. As such, from the perspective of physical observables, there is no coherence between different topological sectors so that if  $|\Psi\rangle \sim |\psi, Q_{\text{top}}\rangle + |\psi', Q_{\text{top}}'\rangle$  then

$$\langle \Psi | A(t) | \Psi \rangle \sim \langle \psi, Q_{\text{top}} | A(t) | \psi, Q_{\text{top}} \rangle + \langle \psi', Q_{\text{top}}' | A(t) | \psi', Q_{\text{top}}' \rangle . \quad (2.25)$$

The vacuum sector of the QFT can be defined as the set of states with wavefunction  $\psi[\Phi(x)] = 0$  unless  $\psi[\Phi(+\infty)] = \psi[\Phi(-\infty)] = \pm \sqrt{\frac{\lambda_0}{-6\mu_0^2}}$ . These states have definite topological charge with  $Q_{\text{top}} = 0$ . The kink sector can be defined similarly as

the set of states with  $\psi[\Phi(x)] = 0$  unless  $\psi[\Phi(+\infty)] = -\psi[\Phi(-\infty)] = \sqrt{\frac{\lambda_0}{-6\mu_0^2}}$ . States in this sector are once again states of definite topological charge with  $Q_{\text{top}} = +1$  and the minimum energy state in this sector is the one kink state.

While the definition of  $\hat{Q}_{\text{top}}$  (2.22) has the desired properties of a topological charge, its physical meaning is unclear. In the case of the Sine-Gordon theory given by the Lagrangian density

$$\mathcal{L} = \frac{1}{2}(\partial_t\phi)^2 - \frac{1}{2}(\partial_x\phi)^2 - \frac{\mu_0^4}{\lambda_0} \left[ \cos\left(\frac{\sqrt{\lambda_0}}{\mu_0}\phi\right) - 1 \right] , \quad (2.26)$$

the kinks in the theory can be treated exactly as the theory is integrable and dual to the Massive Thirring model (MTM) [30]. The topological charge for the Sine-Gordon theory can be defined in the same manner as for the  $\phi^4$  to give

$$\hat{Q}_{\text{top}}^{(\text{SG})} = \frac{1}{2v_{\text{SG}}} \int_{-\infty}^{\infty} \partial_x\phi \, dx , \quad (2.27)$$

where  $v_{\text{SG}}$  is the classical vacuum expectation value. However, in the Sine-Gordon theory the kink field operators  $\psi_K$  can be constructed explicitly [31]. These are given by a two-component fermion field with components

$$\begin{aligned} (\psi_K)_1 &= C : \exp \left[ \frac{-i\beta}{2}\phi - \frac{2\pi i}{\beta} \int_{-\infty}^x dz \partial_t\phi(z) \right] : , \\ (\psi_K)_2 &= -iC : \exp \left[ \frac{\beta}{2}\phi - \frac{2\pi i}{\beta} \int_{-\infty}^x dz \partial_t\phi(z) \right] : , \end{aligned} \quad (2.28)$$

where the colons indicate normal ordering,  $\beta = \frac{\mu_0}{\sqrt{\lambda_0}}$  and  $C$  is a constant which can be found in [31].

In terms of  $\psi_K$  the Sine-Gordon Lagrangian takes the form of the Massive Thirring model

$$\mathcal{L} = \bar{\psi}_K (i\gamma^\mu \partial_\mu - M) \psi_K - \left[ \frac{2\pi^2\mu_0^2}{\lambda_0} - \frac{\pi}{2} \right] (\bar{\psi}_K \gamma^\mu \psi_K)^2 , \quad (2.29)$$

where the components of  $\gamma^\mu$  are given by the Pauli matrices  $\gamma^0 = \sigma_1, \gamma^1 = \sigma_2, \bar{\psi}_K = \psi_K \gamma^0$  and  $M$  is the bare mass which can be related to the Sine-Gordon parameters by the duality in [30]. From the Lagrangian (2.29) the particles corresponding to the kink operators can be seen to be (elementary) fermions of the MTM Lagrangian. The topological charge operator can then also be expressed in terms of  $\psi_K$  to give

$$\hat{Q}_{\text{top}}^{(\text{SG})} = \int dx \, \bar{\psi}_K \gamma^\mu \psi_K , \quad (2.30)$$

which shows that the topological charge is really just the standard fermion number for the kink particles. While we cannot construct the kink field operators explicitly in the  $\phi^4$  theory, the Sine-Gordon model shows that, at least in that case, topological kink defects can be interpreted as elementary particles, despite their unusual formulation. This also provides the physical meaning behind the definition of the topological charge and we can use the intuition from the Sine-Gordon model in the  $\phi^4$  theory.

### 2.3.4 Kinks

As with the vacuum state, semi-classical estimates for observables of the kink state can be obtained far from the strong coupling (Ising class) critical point. Since the kink lies outside the  $Q_{\text{top}} = 0$  sector, they do not appear at any order in perturbation theory when starting from a classical configuration within the vacuum sector. However, perturbation theory can still be applied when starting from a classical kink configuration, though this tends to require more sophisticated methods due to the non-uniformity of the classical kink solutions and the presence of a zero-mode [32].

The one-loop order calculation of the kink mass is a classic result known as the ‘DHN’ result following the work of Dashen, Hasslacher and Neveu [33, 34]. This can be written in terms of the scalar mass  $m_S^2 = 2|\mu_0^2| + \mathcal{O}(\lambda_0)$  up to  $\mathcal{O}(\lambda_0)$  to give

$$M_K = 2\frac{m_S^3}{\lambda_0} + \frac{m_S}{2} \left( \frac{1}{6}\sqrt{\frac{3}{2}} - \frac{3}{\pi\sqrt{2}} \right) + \mathcal{O}(\lambda_0) \quad (2.31)$$

$$= m_S \left[ 2g^{-1} + \frac{1}{2} \left( \frac{1}{6}\sqrt{\frac{3}{2}} - \frac{3}{\pi\sqrt{2}} \right) + \mathcal{O}(g) \right], \quad (2.32)$$

where the second line indicates that in this regime the observable ratio  $m_S/M_K$  also provides a reasonable measure of the effective coupling. From the first expression one can see that in the semi-classical region the kink appears again as a heavy particle such that  $M_K = \mathcal{O}(m_S^3)$ . More recently, zeta-function regularisation has allowed for one-loop results in finite size systems [35] and dimensional regularisation has provided a more systematic approach to one-loop corrections allowing for results at finite temperatures and in higher dimensions [36]. While giving equivalent results to one-loop order, a rigorous treatment of the zero-mode requires more work through e.g. the use of canonical coordinates [37], which also allow for the perturbative computation of the scalar field  $n$ -point functions in the presence of the kink [38, 39].

In the vicinity of the critical point, analytic results can be obtained by uni-

versality. Mean field theory results, which follow from the classical behaviour  $m_S = \xi^{-1} \sim \mu_0 \sim \epsilon^{1/2}$  and  $M_K = \xi_K^{-1} \sim m_S^3$  such that  $\xi_K \sim \xi^3$  i.e.  $\nu_K = 3/2$ , are valid only in the vicinity of the Gaussian fixed point when  $\lambda_0 \rightarrow 0$ . In the Ising model universality class, in addition to the standard critical exponents, universal amplitude ratios [40] can be derived and the ratio of correlation length amplitudes in the symmetric and symmetry broken phases is given by

$$\xi_0/\xi'_0 \approx 2 . \quad (2.33)$$

These results can be related to the topological defects in the  $\phi^4$  theory through the Kramers-Wannier duality present in the Ising Model. While explicit kink creation operators cannot be constructed for the  $\phi^4$  theory, the corresponding disorder operators  $\mu(x)$  can be introduced in the classical Ising model [41]. The Kramers-Wannier duality relates the disorder operator two-point correlation function on the dual lattice at coupling (temperature)  $K$  to the spin operator two-point function at a coupling  $K^*$  as

$$\langle \mu(x)\mu(x') \rangle_K = \langle \sigma(\tilde{x})\sigma(\tilde{x}') \rangle_{K^*} . \quad (2.34)$$

This duality establishes the relation  $\nu'_K = \nu$  between the critical exponents where  $\nu'_K$  is the critical exponent associated to the diverging correlation length  $\xi_K$  of the disorder two-point function  $\langle \mu(x)\mu(x') \rangle$  in the symmetry broken phase. When combined with the universal amplitude ratio Equation (2.33) one can establish

$$\begin{aligned} \xi_K/\xi &\approx \frac{\xi_0|\epsilon|^\nu}{\xi'_0|\epsilon|^{\nu'}} \\ &\approx 2 , \end{aligned} \quad (2.35)$$

which uses the hyperscaling relation  $\nu = \nu'$ . This result corresponds in the  $\phi^4$  theory to the relationship  $m_S \approx 2M_K$  between the scalar mass  $m_S$  and the kink mass  $M_K$ . While universality establishes this result rigorously in the vicinity of the critical point, physically it should hold from the point where first  $m_S \approx 2M_K$  down to the critical point, since in this region the scalar excitation will decay into a kink-antikink pair excitation which is the lightest excitation for the  $Q_{\text{top}} = 0$  sector in this region.

Critical Exponent	Mean Field	Ising Class	Notes for Ising Class
$\nu$	1/2	1	Exact Solution/Conformal Field Theory
$\mu$	1/2	1	Lorentz Invariance: $\mu = \nu$
$\nu'$	1/2	1	Hyperscaling: $\nu' = \nu$
$\mu'$	1/2	1	Lorentz Invariance and Hyperscaling
$\nu'_K$	3/2	1	Kramers-Wannier Duality
$\mu'_K$	3/2	1	Lorentz Invariance

Table 2.1: Table of critical exponents for the  $\phi^4$  theory. The mean-field predictions are valid only when  $\lambda_0 \rightarrow 0$  while for any finite  $\lambda_0$  the theory belongs to the Ising universality class.

### 2.3.5 Summary of Critical Exponents

The various critical exponents for the  $\phi^4$  theory are summarised in Table 2.1 and are illustrated in Figure 2.3 (see also [28] for the equilibrium critical behaviour of  $\phi^4$  theories and [25] for a discussion of dynamics). In Figure 2.3, the classical behaviour of  $2M_K$  and  $m_S$  are plotted as dashed blue and red lines, providing the correct description of the QFT when  $\lambda_0 \rightarrow 0$ . The semi-classical (mean-field) approximation is then given by a simple shift, so that  $m_S \rightarrow 0$  as  $\mu_0^2 \rightarrow m_C^2$ , but gives the incorrect critical behaviour when  $\lambda_0 \neq 0$ , as indicated by the faded dot-dashed lines. Instead, the semi-classical results are correct only away from the critical point, as indicated by the solid blue and red lines, while the correct critical behaviour is that of Ising universality class, illustrated by the solid black lines.

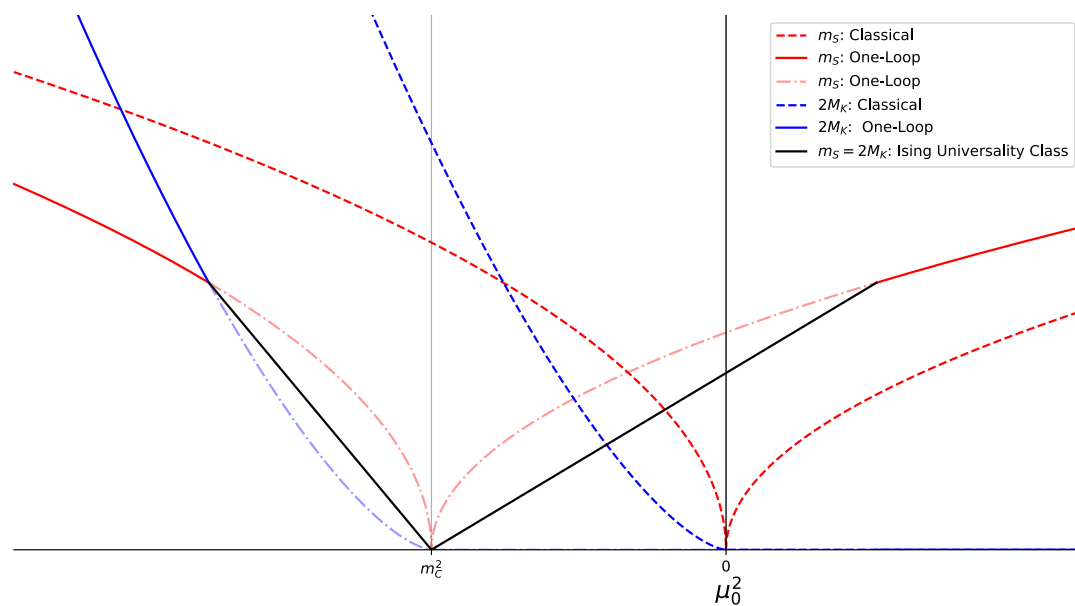


Figure 2.3: The perturbative estimates of scalar mass  $m_S$  and twice the kink mass  $M_K$  are plotted for  $\lambda_0 = 0$  (dashed lines) and illustrated for  $\lambda_0 \neq 0$  by the shifted curves where  $m_S \rightarrow 0$  as  $\mu_0^2 \rightarrow m_C^2$ . For  $\lambda_0 \neq 0$  the perturbative result is correct only away from the critical point, as indicated by the solid lines, but gives an incorrect result near the critical point, as indicated by faded dot-dashed lines. The correct critical behaviour in this case is given by the Ising universality class and is illustrated by solid black lines.

# Chapter 3

## Topological Defect Formation

### 3.1 Introduction

Topological defects can form quite generically in a wide variety of phase transitions [7]. In the case of global symmetry breaking during a continuous transition, the dynamics of the transition and the formation of defects are described by the Kibble Zurek mechanism (KZM). The KZM provides a picture of the transition as a non-equilibrium but nevertheless universal process and predicts the universal scaling of a number of physical quantities. This includes the defect density  $n$  that scales universally as (1.1) with the equilibrium critical exponents and a simple dynamical scale characterising the rate of the transition [9, 10, 11]. While similar scaling relations hold for other quantities, the scaling of defect density is a particularly powerful prediction as topological defects tend to be very long lived so that their distribution can be observed even long after the transition has ended and other excitations have equilibrated.

Recently, there has been interest in the description of the KZM in quantum phase transitions (QPT), i.e. transitions at zero-temperature where the equilibrium state is the ground state [42]. The early confirmation of the KZM scaling of defect density during a QPT in the quantum Ising model [12] was made possible by several simplifying features of the theory. Firstly, in the absence of a transverse field, the quantum states of topological defects in the Ising model can be identified explicitly and exact counting operators can be constructed to establish the defect density. Secondly, the Ising model is integrable in simple dynamical scenarios described by the KZM where it is equivalent to a set of independent Landau-Zener transitions, allowing for analytic results [13]. Due to these properties, the Ising model and other quantum spin systems have been a focal point of much research into the KZM

during QPTs with a number of different quantities being found to scale universally in various models [43, 44, 11]. However, in general systems direct confirmation of the scaling of topological defects can be subtle and quite independent of other quantities which may also show universal scaling [16].

In quantum field theory, the confirmation of the KZM predictions for topological defect formation during QPTs can be challenging and comparatively fewer results have been obtained. For instance, the  $\phi^4$  theory has been studied during the KZM scenario and the expected universal scaling of the correlation length confirmed [2]. However, this does not give direct information about the defect density in the system. Additionally, since explicit counting of defects is highly ultraviolet (UV) sensitive, it cannot be used to extract information about the defect density in a QFT and confirm the KZM prediction (1.1). Instead, a method by which the KZM can be confirmed in a QFT is given by studying the (non-equilibrium) equal time two-point function  $G_2(k)$ . This observable both provides a well behaved estimate of the defect density and displays a clear signature of the presence of topological defects, making it an ideal candidate with which to confirm topological defect formation in a system [45]. However, any confirmation of the KZM still requires the computation of a non-equilibrium observable, in this case  $G_2(k)$ , and otherwise successful non-equilibrium techniques such as those based on the two-particle irreducible (2PI) representation are known to fail to capture the presence of defects during symmetry breaking scenarios [3], though more sophisticated methods have been more successful [18].

In this chapter, we will first introduce the Kibble Zurek mechanism in Section 3.2 and discuss various aspects of it such as the adiabatic-impulse-adiabatic assumption (AIA), the prediction of universal scaling and the formation of topological defects. Second, we will discuss the KZM applied to the  $\phi^4$  QFT and give the predicted scalings in this case before outlining the expected form of  $G_2(k)$ , which we will call the “defect ansatz”  $G_{\text{def}}(k)$ , specialising to the QPT case.

## 3.2 The Kibble Zurek Mechanism

### 3.2.1 AIA Assumption

The essential description of the dynamics captured by the KZM is summarised by the “adiabatic impulse adiabatic” (AIA) assumption [11]. The basic structure of this assumption was first put forward by Kibble [9] who considered a situation where a system was initially in equilibrium within the symmetric phase and approaches

the critical point of a continuous phase transition.

More concretely, consider a system parametrised by a reduced dimensionless coupling  $\epsilon$  that is in the symmetric phase and being driven towards a phase transition by some external process. This corresponds to  $\epsilon \rightarrow 0$  and  $\epsilon$  can be considered to have some time dependence  $\epsilon(t)$  dictated by the environment driving the change.

In this scenario, the correlation length  $\xi$  associated to the order parameter of the equilibrium state diverges in the vicinity of the critical point such that

$$\xi \approx \xi_0 |\epsilon|^{-\nu}, \quad \epsilon > 0. \quad (3.1)$$

However, if the state is initially in equilibrium at some  $\epsilon > 0$ , then Kibble argued that it will not be possible for any physical state of the system to remain in equilibrium all the way up to the critical point since no physical state can have a correlation length that is increasing faster than the speed of light. Therefore, while a state can initially evolve adiabatically, any realistic, finite rate continuous phase transition must ultimately be a non-equilibrium process where the physical correlation length remains finite into the symmetry broken phase.

Zurek later expanded the above argument by considering the relevant time scales in play during the transition that dictate whether the state can remain in equilibrium [10]. For a state to evolve adiabatically, it must be able to adapt to externally driven changes in the system. Denoting the characteristic relaxation timescale of a state as  $\tau$  and the timescale characterising the external change as  $\tau_{\text{ext}}$ , then the adiabatic condition, where the state will remain in equilibrium, can be summarised as

$$\tau \ll \tau_{\text{ext}}. \quad (3.2)$$

Conversely, the diabatic (impulse) condition, where the state does not react at all to external changes, can be summarised as

$$\tau \gg \tau_{\text{ext}}. \quad (3.3)$$

In a continuous phase transition, Kibble's argument can then be restated in terms of timescales. The critical point of a continuous phase transition is associated to a diverging timescale, characterising relaxation in the equilibrium state, which scales universally

$$\tau \approx \tau_0 |\epsilon|^{-\mu}, \quad \epsilon > 0, \quad (3.4)$$

near the critical point. As such, for any finite  $\tau_{\text{ext}}$ , the adiabatic condition (3.2) will always be violated by the equilibrium state near the critical point. Additionally, the impulse condition (3.3) will always be satisfied by the equilibrium state in the vicinity of the critical point. The adiabatic-impulse-adiabatic (AIA) assumption then states that, in the process of a continuous phase transition, a state will first evolve adiabatically before equilibrium is lost. At that point, the evolution is assumed to be impulsive up until the point when evolution can again proceed adiabatically with the external change.

### 3.2.2 Non-Equilibrium Universal Scaling

While the AIA assumption gives a generic description of a continuous phase transition, Zurek further argued that when  $\tau_{\text{ext}}$  is sufficiently large, the state will remain in equilibrium all the way into the critical region. In this case universality arguments can be applied leading to the universal scaling of various quantities, in particular the correlation length  $\xi$ .

Estimating the point at which equilibrium is lost by the condition

$$\tau_{\text{ext}} \approx \tau , \quad (3.5)$$

then for sufficiently large  $\tau_{\text{ext}}$  the behaviour of  $\tau$  can be further estimated by its universal scaling (3.4) so that the previous condition reads

$$\tau_{\text{ext}} \approx \tau_0 |\epsilon|^{-\mu} . \quad (3.6)$$

Assuming that the behaviour of  $\epsilon(t)$  can be linearised in the vicinity of the critical point so that

$$\epsilon(t) = -t/\tau_Q , \quad (3.7)$$

where  $\tau_Q$  is the ‘‘quench rate’’, the timescale  $\tau_{\text{ext}}$  is given by the relative rate of change of  $\epsilon$  i.e.  $|\dot{\epsilon}/\epsilon|$ . In the linear quench case  $|\dot{\epsilon}/\epsilon| = t^{-1}$  so that the associated external timescale is simply the time distance from the critical point  $\tau_{\text{ext}} = t$ . Using this expression for  $\tau_{\text{ext}}$  then

$$\hat{t} \approx - (\tau_0 \tau_Q^\mu)^{\frac{1}{1+\mu}} \quad (3.8)$$

is the estimated time at which equilibrium will be lost. Since the state at time  $\hat{t}$  is still approximated by the equilibrium state of the system, the expression (3.8)

allows for the calculation of other quantities at the point when equilibrium is lost. In particular, the correlation length  $\xi(\hat{t}) = \hat{\xi}$  can be calculated using its universal scaling (3.1) to give

$$\hat{\xi} \approx \xi_0 (\tau_0^{-1} \tau_Q)^{\frac{\nu}{1+\mu}}. \quad (3.9)$$

Therefore, the KZM predicts that the physical length scale at the point equilibrium is lost will scale with the equilibrium universal critical exponents, along with the dynamical scale  $\tau_Q$ . Combining this with the AIA assumption, the length scale  $\hat{\xi}$  is then assumed to equal the correlation length  $\xi$  of the state when entering the symmetry broken phase. While in practice the state will not freeze out exactly, the universal scaling is still expected to hold with only the non-universal coefficients being modified.

### 3.2.3 Topological Defects and Their Relevance

With the AIA assumption, the KZM provides information about the post transition state which encodes details of the phase transition in universal quantities e.g. the finite correlation length and the quasiparticle excitation density. As a system evolves following the phase transition it will equilibrate. In this way, details of the phase transition encoded in the state will be lost and the universal scale  $\hat{\xi}$  will become irrelevant for future evolution. However, Kibble argued that in the case where topological defects can exist in a system, they should necessarily be formed randomly during a continuous phase transition. This can again be seen as a consequence of causality. A topological defect corresponds to an excitation which interpolates between different symmetry broken vacua. Therefore, in order to have a state with no defects, spontaneous symmetry breaking must occur in a spatially uniform manner. In general, this cannot happen since perturbations in causally separated regions must act independently and so defects must be formed.

Since the correlation length  $\hat{\xi}$  sets the scale of correlated domains in the post transition state and defects exist at the boundaries between such domains, the defect density can be related to  $\hat{\xi}$  as

$$n \sim \hat{\xi}^{-D_{co}}. \quad (3.10)$$

Therefore, the universal length scale  $\hat{\xi}$  is encoded in the density of defects  $n$  following the phase transition, as it will be in a number of other quantities such as the distribution of quasi-particles. However, following the transition the initially highly

exited state will begin to equilibrate and non-defect excitations can be expected to thermalise relatively quickly thus wiping out any memory of the universal scale encoded in them. The system should then be well described by a random distribution of topological defects with density  $n$ . In this case, the evolution of the correlation length  $\xi(t)$  is essentially determined by the distribution of defects and the universal scale  $\hat{\xi}$  will remain relevant for the subsequent evolution.

As the topological defects carry details of the phase transition for long periods of time, they are sometimes described as “fossilised evidence” of the dynamics of the transition. This is essential in fields such as cosmology where the system cannot be probed near the time of the phase transition. Additionally, the random distribution of defects tends to provide a relatively clean environment for study, once other noise from the transition has thermalised. It is for these reasons that the universal scaling of the defect density can be considered the key testable prediction of the KZM.

### 3.3 The Kibble Zurek Mechanism in $\phi^4$ Quantum Field Theory

#### 3.3.1 Universal Scaling in the $\phi^4$ theory

The KZM can easily be specialised to the  $\phi^4$  scalar field theory in  $D = (1 + 1)$  undergoing a QPT. Assuming a linear quench of the reduced coupling, the external time scale  $\tau_{\text{ext}}$  is given simply by the absolute time  $t$  while the internal time scale  $\tau$  is given by the inverse of the scalar mass  $m_S$  (equal to the gap  $\Delta$ ) which determines the asymptotic decay of the ground state two-point function in time,

$$G_2(t) = \langle \Omega | \phi(t, x) \phi(0, x) | \Omega \rangle \sim e^{-m_S t} \quad \text{as } t \rightarrow \infty . \quad (3.11)$$

Furthermore, Lorentz invariance implies that the gap not only sets the temporal correlation length but also the spatial correlation length such that  $\tau = \xi = m_S^{-1}$ . The critical exponents  $\mu$  and  $\nu$  are then equal and the expression for the correlation length  $\hat{\xi}$  simplifies to

$$\hat{\xi} \approx \xi_0 (\Delta_0 \tau_Q)^{\frac{\nu}{1+\nu}} , \quad (3.12)$$

where  $\Delta_0$  is the coefficient determined by the vanishing gap on approach to the critical point

$$\Delta = m_S \approx \Delta_0 |\epsilon|^\mu. \quad (3.13)$$

With the classical  $D = 2$  Ising model universality class exponent  $\nu = 1$  (see Table 2.1) the state at time  $\hat{t}$  is approximately the equilibrium state  $|\Omega(\hat{\epsilon})\rangle$  and characterised by the quantities

$$\hat{t} \approx -\Delta_0^{-\frac{1}{2}} \tau_Q^{\frac{1}{2}}, \quad (3.14)$$

$$\hat{\epsilon} \approx -\Delta_0^{-\frac{1}{2}} \tau_Q^{-\frac{1}{2}}, \quad (3.15)$$

$$\hat{\xi} \approx \xi_0 \Delta_0^{\frac{1}{2}} \tau_Q^{\frac{1}{2}}, \quad (3.16)$$

which can be contrasted with those obtained using mean field theory which incorrectly predicts  $\nu_{MF} = 1/2$  to give  $\hat{t} \sim \tau_Q^{1/3}$ ,  $\hat{\epsilon} \sim \tau_Q^{-1/3}$  and  $\hat{\xi} \sim \tau_Q^{1/3}$ .

With the post transition correlation length estimated by  $\hat{\xi}$ , the kink defect density of the state scales as

$$n \sim \tau_Q^{-\frac{1}{2}}. \quad (3.17)$$

While the scaling (3.17) should hold for sufficiently slow quenches, if  $\tau_Q$  is too small the system will lose equilibrium before ever reaching the critical region and the scaling given by the (quantum) critical exponents will be irrelevant. In this case, mean field theory can be applied and the defect density scales as

$$n \sim \tau_Q^{-\frac{1}{3}} \quad : \quad \tau_Q \leq \tau_Q^X, \quad (3.18)$$

where  $\tau_Q^X$ , the size of  $\tau_Q$  at which this quantum-classical crossover takes place, can be estimated from the equilibrium data [2].

### 3.3.2 Defect Ansatz for Quantum Phase Transitions

The KZM predicts that the post transition state for the  $\phi^4$  theory should be described by a random distribution of kinks. In the classical theory, the form of  $G_2(k)$  for a system of random kinks can be constructed explicitly and the defect density  $n$  can be found from the long distance  $k \rightarrow 0$  behaviour of  $G_2(k)$ , indicating it is a promising observable with which to estimate defect density in the quantum theory [3, 45]. The central idea to this construction is that in a system of random

kinks there only two relevant scales in the system:  $n$  the defect density and  $d_K$  the kink width. When these scales are well separated (and typically  $d_K \ll n^{-1}$  in KZM scenarios) the two-point function factorises in momentum space into a contribution coming only from the distribution of kinks  $G_{\text{corr}}(k/n)$  and a contribution coming from the kink profile  $G_{\text{kink}}(kd_K)$ . The classical two-point function for a system of random kinks can then be written as

$$G_{\text{RK}}(k) = \frac{v^2}{n} G_{\text{corr}}(k/n) G_{\text{kink}}(kd_K) . \quad (3.19)$$

In the classical theory the kink profile contribution  $G_{\text{kink}}(kd_K) = \frac{k^2}{4v^2} |\phi_K(k)|^2$  can be calculated exactly via the Fourier transform of the kink solution  $\varphi_K(x)$  (2.8) which gives

$$\phi_K(k) = \frac{2iv}{k} \frac{\frac{1}{2}\pi kd_K}{\sinh \frac{1}{2}\pi kd_K} \quad (3.20)$$

such that

$$G_{\text{kink}}(kd_K) = \left( \frac{\frac{1}{2}\pi kd_K}{\sinh \frac{1}{2}\pi kd_K} \right)^2 . \quad (3.21)$$

Additionally, the form of  $G_{\text{corr}}(k/n)$  can also be calculated explicitly in the case of uniformly random kinks to give an exponential decay in real space [3]. However, a better form can be found phenomenologically [45] using classical simulations to give

$$G_{\text{corr}}(k/n) = \alpha_1 e^{-\alpha_2 (k/n)^2} + \frac{\beta_1}{[1 + \beta_2 (k/n)^2]} \quad (3.22)$$

which in real space is just the sum of a Gaussian part and the exponential part coming from uniform randomness, i.e.,

$$G_{\text{corr}}(nr) = a_1 e^{-a_2 (nr)^2} + b_1 e^{-b_2 nr} . \quad (3.23)$$

The above picture can be confirmed in a classical field theory by considering the dynamics of an (ensemble) of scalar fields that are driven through a (classical) phase transition before relaxing under some damping term such that the expectation value of the two-point function  $G_2(k) = \langle \phi(-k)\phi(k) \rangle$  can be calculated and compared to the ansatz for random kinks (3.19). The ansatz can then be used by first establishing the form of  $G_{\text{corr}}(k/n)$ . This is achieved by taking a subset of data, explicitly counting the number of defects  $n$  and using this to scale the two-point function.

The assumption  $G_2(k) = G_{\text{RK}}(k)$  can then be checked by rearranging it to give

$$\frac{n}{v^2} \frac{G_2(k)}{G_{\text{kink}}(kd_K)} = G_{\text{corr}}(k/n) . \quad (3.24)$$

If this holds, then the left-hand side of (3.24) should be a universal function of  $n$  only and the functional form of  $G_{\text{corr}}(k/n)$  can be fit to establish the universal parameters  $\alpha_1, \alpha_2, \beta_1, \beta_2$ . The ansatz (3.19) can then be used as a one-parameter fit to measure the defect density  $n$  in the remaining data, which can be checked against the values obtained by explicit counting.

When topological defects are formed in a quantum field theory via the KZM, we can again assume that the only two relevant scales in the system are  $n$  and  $d_K$  such that the general factorisation of  $G_2(k)$  follows as in a classical theory. However, we can also expect additional contributions to  $G_2(k)$  in the quantum theory coming from the ground state and the excitations generated during the phase transition. While in a classical theory a damping term can be added to the action to remove energy from the system so that the contribution of excitations can be neglected, in a quantum theory with unitary evolution energy is conserved and we can expect these contributions to be important.

These additional contributions can be included to provide a suitable defect ansatz for the case of defects generated by unitary time evolution through a quantum phase transition. Writing the ground state two-point function as  $G_2^\Omega(k)$  and the two-point function of the excitations (matter) as  $G_{\text{mat}}(k)$ , the defect ansatz  $G_{\text{def}}(k)$  for a quantum theory can then be written as

$$G_{\text{def}}(k) = \frac{v^2}{n} G_{\text{corr}}(k/n) G_{\text{kink}}(kd_K) + G_2^\Omega(k) + G_{\text{mat}}(k) , \quad (3.25)$$

where the various quantities now take on their full quantum corrections. In particular, the ground state  $|\Omega\rangle$  determines the two-point function  $G_2^\Omega(k) = \langle \Omega | \phi(-k) \phi(k) | \Omega \rangle$  and the vacuum expectation value. Similarly, the one-kink particle state  $|K\rangle$  determines the kink profile term  $G_{\text{kink}}(kd_K)$ .

To confirm topological defect formation in the QFT case, we would like to calculate the full non-equilibrium two-point function  $G_2(k)$  and check the assumption that  $G_2(k) = G_{\text{def}}(k)$  by independently calculating  $n, G_2^\Omega(k), G_{\text{kink}}(kd_K)$  and  $G_{\text{mat}}(k)$ . Similarly to the classical case, this assumption can then be rewritten as

$$\frac{n}{v^2} \frac{G_2(k) - G_2^\Omega(k) - G_{\text{mat}}(k)}{G_{\text{kink}}(kd_K)} = G_{\text{corr}}(k) , \quad (3.26)$$

which should be a universal function of the defect density as before. Of course, in the quantum theory the forms of  $v^2$ ,  $G_{\text{kink}}(kd_K)$ ,  $G_2^\Omega(k)$  and  $G_{\text{mat}}(k)$  are not known exactly and approximations must be used. More problematically, unlike in the classical theory,  $n$  cannot be estimated through explicit counting to allow the form of  $G_{\text{corr}}(k)$  to be established by scaling a subset of data.

To gain an estimate of the defect density without reference to the unknown quantity  $G_{\text{corr}}(k/n)$  in a QFT, we can use the assumption that  $G_2(k=0) = G_{\text{def}}(k=0)$ . At  $k=0$  the contribution from the kink profile drops out of  $G_{\text{def}}(k)$  while the matter contributions should be negligible such that  $G_{\text{def}}(k=0) \approx v^2/n + G_2^\Omega(k=0)$ . Therefore, the defect density can be estimated as

$$n_{\text{est}} = [G_2(k=0) - G_2^\Omega(k=0)] / v^2 , \quad (3.27)$$

which requires only the knowledge of the non-equilibrium state and the ground-state at  $k=0$ , which can be calculated relatively easily by e.g. Monte Carlo techniques.

With the defect density estimated, in principle the form of  $G_{\text{corr}}(k/n)$  can then be established as in the classical case by rescaling the non-equilibrium data with  $n_{\text{est}}$  and fitting to a subset of the data. The KZM can then be confirmed by the agreement of the fixed form of  $G_{\text{corr}}(k)$  with the remaining data and its universal scaling with  $k/n$ . However, in practice more assumptions will be required in order to calculate the remaining quantities  $G_{\text{kink}}(kd_K)$  and  $G_{\text{mat}}(k)$ . As such, to confirm the KZM is it better to proceed in a few more stages that allow one to check the approximations being made more carefully. The specific approximations used and the corresponding stages for confirming the KZM via the defect ansatz are discussed further in Chapter 9, once the approximation method to be used has been introduced in Chapters 4 and 5.

# Chapter 4

## Hamiltonian Lattice Regularisation

### 4.1 Introduction

For non-perturbative calculations it is common to use lattice methods which provide a non-perturbative UV regularisation [46]. An appropriate lattice theory can be obtained corresponding to a particular QFT by discretising the continuum action and there are a number of different options for this that differ only by irrelevant terms. When the physical length scales of the lattice theory, e.g. the correlation length  $\xi$ , are larger than the lattice spacing  $a$ , the infrared lattice observables can be approximated by a continuum QFT (and vice versa). These become equivalent in the continuum limit when  $\xi/a \rightarrow \infty$  i.e. in the vicinity of a continuous phase transition. Usually, the construction of a lattice theory takes place in the Lagrangian lattice framework with both time and space being discretised and Euclidean space-time being used to effectively transform the problem of quantum field theory into statistical mechanics. This enables the use of Monte Carlo sampling of the path integral to evaluate the observables of interest. However, since analytically continuing back to real time requires further assumptions and tends to dramatically increase statistical errors, this method is essentially restricted to equilibrium physics.

To instead study the time evolution of quantum states, in particular the non-equilibrium physics of defect formation, it is natural to use a Hamiltonian lattice theory where only the spatial dimension is discretised leaving the time dimension continuous. One advantage of the Hamiltonian lattice framework is that the lattice theory is a valid quantum many body theory in its own right and techniques from this field can be applied to calculate the observables of interest.

In this chapter, we will first introduce the lattice Hamiltonian for the  $\phi^4$  theory before discussing how observables of the continuum theory can be approximated by tuning the parameters of the lattice theory. We will then introduce additional cutoffs that allow standard quantum many body techniques to be applied and discuss how the various observables of interest can be approximated in the lattice framework, focussing on the equal time ground state and kink expectation values along with the scalar mass. Finally, we will review the use of a real space Fock basis for the theory along with boson number truncations which allow for the use of numerically stable quantum many body physics methods to be applied to the lattice theory.

## 4.2 Hamiltonian Lattice Theory for $\phi^4$

### 4.2.1 The Lattice Hamiltonian and Effective Theory

The lattice provides an intuitive regularisation scheme, decoupling high momentums from low momentums via a hard cutoff  $\Lambda = \pi/a$  such that the momentum modes are restricted to  $-\Lambda \leq p \leq \Lambda$ . This regularisation framework can be readily adapted to a given QFT by discretising the spatial derivatives in the continuum Hamiltonian by finite difference approximations  $\partial_x \phi \rightarrow \delta_a \phi$ . The simplest choice for this is the use of first order finite differences  $\delta_a \phi = \frac{1}{a} [\phi(x+a) - \phi(x)]$  which lead to a lattice  $\phi^4$  theory with Hamiltonian

$$H[\phi] = a \sum_x \left[ \frac{1}{2} (\pi_x)^2 + \frac{1}{2a^2} (\phi_{x+a} - \phi_x)^2 + \frac{\mu_0^2}{2} \phi_x^2 + \frac{\lambda_0}{4!} \phi_x^4 \right]. \quad (4.1)$$

Since the discretisation has introduced an additional dimensionful parameter  $a$ , the lattice spacing with dimension  $[a] = -1$ , there will be two dimensionless parameter ratios to consider. Working in lattice units removes this redundancy and effectively sets  $a = 1$  so that  $x = \{1, 2, 3, \dots\}$ . In lattice units the Hamiltonian can be written as

$$\tilde{H}[\phi] = \sum_x \left[ \frac{1}{2} (\tilde{\pi}_x)^2 + \frac{1}{2} (\phi_{x+1} - \phi_x)^2 + \frac{\tilde{\mu}_0^2}{2} \phi_x^2 + \frac{\tilde{\lambda}_0}{4!} \phi_x^4 \right], \quad (4.2)$$

where the now dimensionless  $\tilde{H} = aH$ ,  $\tilde{\pi} = a\pi$  and the two dimensionless parameters are  $\tilde{\mu}_0^2 = a^2 \mu_0^2$  and  $\tilde{\lambda}_0 = a^2 \lambda_0$ . The discrete canonical commutation relation is given

in lattice units by

$$[\phi_x, \tilde{\pi}_y] = i\delta_{x,y} . \quad (4.3)$$

To use the lattice theory as an effective theory, lattice observables are associated to physical (measurable) quantities. For instance, a measured particle mass  $m_{\text{phys}}$  can be equated to the energy gap of the theory, i.e. the lattice scalar mass  $m_S$ . Other lattice quantities can then be computed in terms of  $m_S$ , such as the lattice kink mass  $M_K$ , providing a prediction for the corresponding physical quantities to be measured in terms of  $m_{\text{phys}}$ . Since the lattice is artificial, the finite lattice spacing will introduce systematic errors into predictions. For a lattice observable characterised by the distance  $r = a\tilde{r}$ , the contributions from the finite lattice spacing can be expected to scale as some inverse power e.g.  $\tilde{r}^{-1}$ . For long distance/infrared (IR) lattice observables with  $\tilde{r} \gg 1$ , the error due to finite lattice spacing should then be small and the corresponding physical predictions should match experiment closely. In order to reduce discretisation errors, additional operators can be included in the Hamiltonian [26] but we will use the form (4.2) that keeps only the leading order terms that are relevant as  $\tilde{r} \rightarrow \infty$ . Lattice units can be kept throughout calculations with different lattice observables being related to one another in lattice units. Physical units can be chosen at the end of calculations when equating the lattice observable in lattice units to a measured quantity in physical units. This determines the lattice spacing  $a$  in terms of the physical units used in experiments, allowing other lattice observables to be expressed in these units as well [47].

The key length scale on the lattice is given by the correlation length, associated to a physical particle by equating  $m_S = m_{\text{phys}}$ . As such, we will be interested in observables on the scale  $\tilde{r} \sim \tilde{\xi}$ . When  $\tilde{\xi} \gg 1$ , errors due to finite  $a$  will be small and the lattice will provide a useful effective theory. Since the lattice spacing provides only small corrections to the IR lattice observables in this regime, such observables can be approximated by a continuum theory (a QFT) and vice versa. In practice, it may even be possible to use a continuum approximation for the IR lattice observables with only very modest  $\tilde{\xi}$  so that we refer to the entire region with  $\tilde{\xi} > 1$  as the “continuum region” of the lattice theory.

### 4.2.2 Continuum Limit

By tuning the parameters  $\tilde{\mu}_0^2, \tilde{\lambda}_0$  of the Hamiltonian (4.2) such that  $\tilde{\xi} \rightarrow \infty$  (or equivalently  $\tilde{m}_S \rightarrow 0$ ), the lattice theory approaches a continuous phase transition.

In the vicinity of the critical line where  $\tilde{\xi} \rightarrow \infty$ , IR lattice observables become insensitive to the lattice spacing and equivalent to the observables of a (continuum) quantum field theory. Since the physics of critical points is universal, the same QFT will describe the IR observables of a large class of lattice theories whose Hamiltonians differ only by irrelevant terms.

The phase diagram for the theory (4.2) can be illustrated using perturbation theory. When the effective coupling  $g = \lambda_0/m_S^2 = \tilde{g} = \tilde{\lambda}_0/\tilde{m}_S^2$  is small, the scalar mass  $\tilde{m}_S = \tilde{\xi}^{-1}$  can be estimated in the symmetric phase using renormalised perturbation theory about the trivial vacuum [26]. The resulting  $\tilde{m}_S^2$  can be expressed in terms of the bare parameters as

$$\tilde{\mu}_0^2 = \tilde{m}_S^2 - \frac{1}{8\pi} \log\left(\frac{64}{\tilde{m}_S^2}\right) \tilde{\lambda}_0 + \mathcal{O}(\lambda_0^2). \quad (4.4)$$

Keeping only the  $\tilde{m}_S^2$  independent terms of order  $\tilde{\lambda}_0$  and rearranging the expression (4.4) gives

$$\tilde{\lambda}_0 = \frac{(\tilde{m}_S^2 - \tilde{\mu}_0^2)8\pi}{\log(64)}, \quad (4.5)$$

which can be used to estimate lines of constant  $m_S$  in the phase diagram. Lines of constant  $g$  can also be estimated by substituting in  $g = \lambda_0/m_S^2$  to (4.5) which gives

$$\tilde{\lambda}_0 = \frac{g}{1 - g \log(64)/(8\pi)} \tilde{\mu}_0^2. \quad (4.6)$$

The critical line can then roughly be estimated by taking  $m_S \rightarrow 0$  in (4.5) or  $g \rightarrow \infty$  in (4.6) so that

$$\tilde{\lambda}_0 = -\frac{8\pi\tilde{\mu}_0^2}{\log(64)} \quad \text{when } m_S \rightarrow 0. \quad (4.7)$$

The phase diagram can then be visualised in the  $(\tilde{\mu}_0^2, \tilde{\lambda}_0)$  plane by plotting lines of constant  $\tilde{m}_S^2$  and  $g$  as shown in Figure 4.1.

The phase diagram shown in Figure 4.1 illustrates the two possibilities for taking the continuum limit  $\tilde{m}_S \rightarrow 0$  in this lattice theory. In the first case, corresponding to the standard perturbative renormalisation procedure,  $g$  is kept fixed and the critical line is approached by tuning  $\tilde{\mu}_0^2$  and  $\tilde{\lambda}_0$  such that  $\tilde{m}_S \rightarrow 0$ . In this case, the only possibility is that  $\tilde{\mu}_0^2 \rightarrow 0$  and  $\tilde{\lambda}_0 \rightarrow 0$ . At the critical point, the corresponding continuum theory is the massless Gaussian QFT and the vicinity is described by the  $\phi^4$  QFT. This allows for the application of standard perturbative

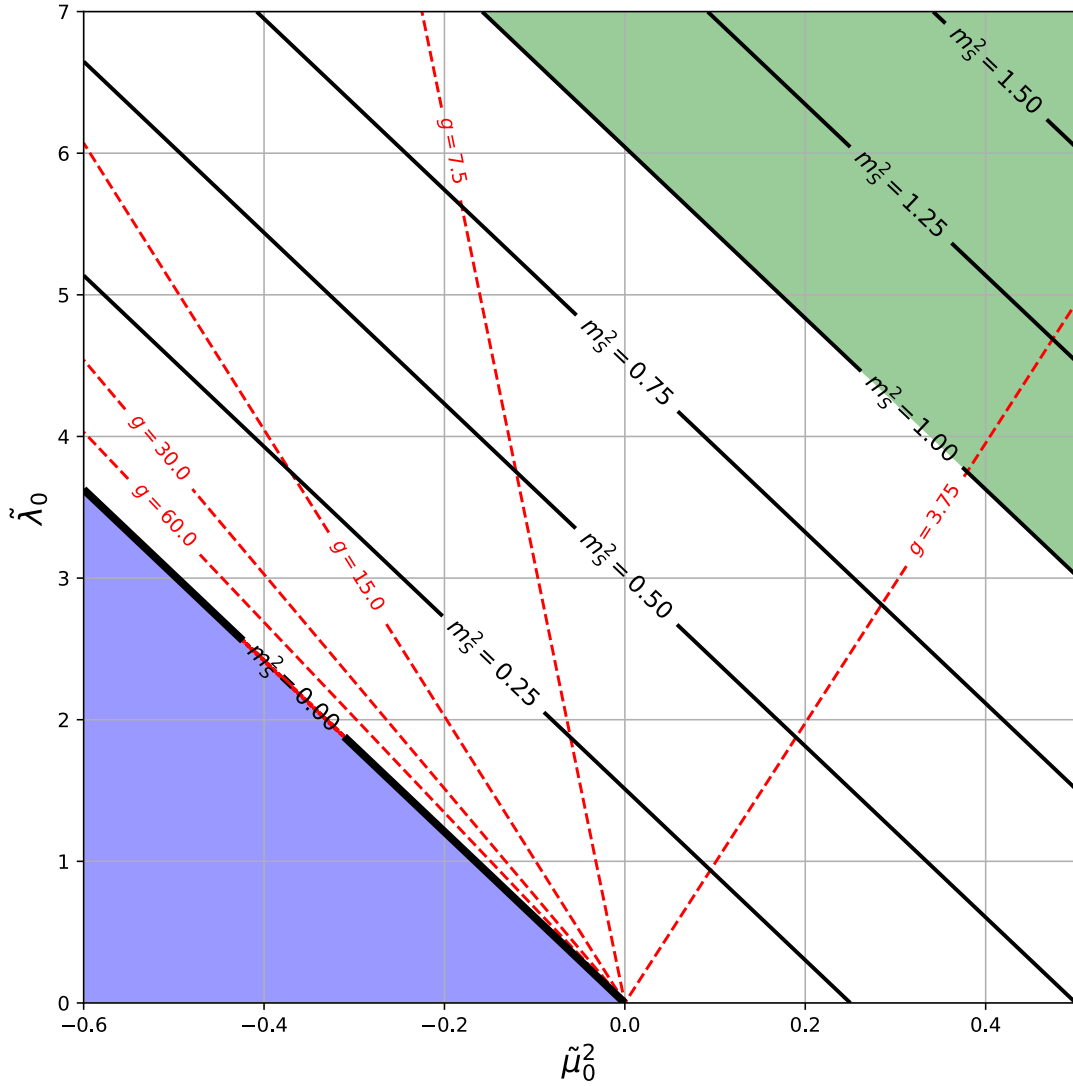


Figure 4.1: The phase diagram for the lattice Hamiltonian  $\phi^4$  theory (4.2) estimated using perturbation theory. Lines of constant  $m_S$  (solid black) and of constant  $g$  (dashed red) map out the diagram in the symmetric phase. The broken symmetry phase is indicated by the blue shaded region in the lower-left corner and is separated from the symmetric region by the critical line where  $m_S = 0$  (thick solid black line). The region where  $m_S > 1$  is also shaded and corresponds to the “lattice region” where finite lattice spacing effects will be important. If the continuum limit  $m_S \rightarrow 0$  is taken along a line of fixed  $g$ , then both  $\tilde{\mu}_0^2 \rightarrow 0$  and  $\tilde{\lambda}_0 \rightarrow 0$ . Any other way of approaching the critical line (e.g. for fixed  $\tilde{\lambda}_0$ ) passes through lines of higher and higher effective coupling  $g$  which diverges in the vicinity of the critical line.

techniques when  $g \leq 1$  and the critical exponents can be derived such that the mean-field critical exponents given in Table 2.1 give the correct behaviour in this instance.

In the second case, which cannot be studied using standard perturbation theory,

the critical line is approached away from the point at  $\tilde{\lambda}_0 \rightarrow 0$  e.g. by keeping  $\tilde{\lambda}_0$  fixed and lowering  $\tilde{\mu}_0^2 \rightarrow \tilde{m}_C^2(\tilde{\lambda}_0)$ . In this case,  $g$  is not fixed and in fact diverges as the critical line is approached. Along the critical line, the continuum critical theory is one of massless Majorana fermions which determines the critical exponents in this case. Since the critical theory is not the massless Gaussian theory, we will refer to this scenario as a “strong coupling” transition. In the vicinity of the critical line, the IR observables are given by a theory of massive Majorana fermions. This is the same continuum limit as the Ising model so that it can be used to compute quantities such as the universal amplitude ratio and Kramers-Wannier duality which are not properties of the critical massless theory directly.

### 4.2.3 Infrared Cutoff

In order to study topological defects non-perturbatively in a lattice setting, it is typical to consider imposing twisted-periodic boundary conditions (TPBC) in the spatial directions and study the corresponding finite size theory where the twist has some definite (but arbitrary) location on a lattice [48]. This method of studying topological defects is quite general and has been applied to both kinks in the  $\phi^4$  theory [49] and to gauge theories e.g. in the study of monopoles [50, 51]

The most standard infrared cutoff technique is to impose periodic boundary conditions (PBC) on the lattice theory over a length  $L = a\tilde{L} = aN$  such that  $\phi_{x+N} = \phi_x$ . The corresponding finite size theory is given by the Hamiltonian

$$\tilde{H}[\phi]_{(PBC)} = \sum_{x=1}^N \left[ \frac{1}{2}(\tilde{\pi}_x)^2 + \frac{1}{2}(\phi_{x+1} - \phi_x)^2 + \frac{\tilde{\mu}_0^2}{2}\phi_x^2 + \frac{\tilde{\lambda}_0}{4!}\phi_x^4 \right], \quad (4.8)$$

where the field operators in (4.8) are related to the originals in the obvious manner

$$\phi_x = \phi_{x+nN} \quad \text{for } n \in \mathbb{Z}, \quad (4.9)$$

so that we do not distinguish them with different symbols. The choice of PBC is consistent with the requirements of the vacuum sector in that states where  $\psi[\Phi(+L)] = \psi[\Phi(0)]$  are energetically favoured, corresponding to the infinite size limit where  $\psi[\Phi(x)]$  is only non-zero when  $\psi[\Phi(+\infty)] = \psi[\Phi(-\infty)]$ .

To study topological defects, one can instead impose TPBC as  $\phi_{x+N} = -\phi_x$  in order to energetically favour states where  $\psi[\Phi(+L)] = -\psi[\Phi(0)]$ , corresponding to the requirement for states lying outside the vacuum sector that  $\psi[\Phi(x)]$  is non-zero only if  $\psi[\Phi(+\infty)] = -\psi[\Phi(-\infty)]$ . The finite size Hamiltonian corresponding to the

choice of TPBC is given as

$$\tilde{H}[\phi]_{(TPBC)} = \sum_{x=1}^N \left[ \frac{1}{2}(\tilde{\pi}_x)^2 + \frac{1}{2}(\bar{\phi}_{x+1} - \bar{\phi}_x)^2 + \frac{\tilde{\mu}_0^2}{2}\bar{\phi}_x^2 + \frac{\tilde{\lambda}_0}{4!}\bar{\phi}_x^4 \right] + 2\bar{\phi}_N\bar{\phi}_1, \quad (4.10)$$

where the field operators  $\bar{\phi}$  in (4.10) are related to the originals by

$$\bar{\phi}_x = \begin{cases} \phi_{x+2nN} & \text{for } n \in \mathbb{Z} \\ -\phi_{x+(2n+1)N} & \text{for } n \in \mathbb{Z} \end{cases}$$

and the location of the twist is chosen arbitrarily to be at the site  $N$  on the lattice.

With the addition of the infrared cutoff, the momentum modes are discretised and accurate approximation of the full theory now requires a hierarchy of scales  $a \ll \xi \ll L$  or equivalently  $\pi/L \ll k \ll \pi/a$  so that the strict continuum limit can only be taken once  $L \rightarrow \infty$ .

## 4.3 Lattice Approximation of Observables for $\phi^4$

### 4.3.1 The Ground State and One-Kink State

For the study of topological defects and the Kibble Zurek Mechanism, we will be particularly interested in the equal-time observables of the ground state  $\langle \Omega | \mathcal{O}[\phi] | \Omega \rangle$  and one kink state  $\langle K | \mathcal{O}[\phi] | K \rangle$ . These are approximated in the lattice theory by the corresponding lattice observables  $\langle \Omega(a, L) | \mathcal{O}[\phi] | \Omega(a, L) \rangle$  and  $\langle K(a, L) | \mathcal{O}[\phi] | K(a, L) \rangle$  where the state  $|\Omega(a, L)\rangle$  is simply the minimum energy state of the lattice theory with PBC (4.8) i.e.

$$|\Omega(a, L)\rangle = \arg \min_{|\psi\rangle} \left( \langle \psi | \tilde{H}_{(PBC)} | \psi \rangle - \lambda [\langle \psi | \psi \rangle - 1] \right) \quad (4.11)$$

and  $|K(a, L)\rangle$  is the minimum energy state of the twisted theory (4.10)

$$|K(a, L)\rangle = \arg \min_{|\psi\rangle} \left( \langle \psi | \tilde{H}_{(TPBC)} | \psi \rangle - \lambda [\langle \psi | \psi \rangle - 1] \right). \quad (4.12)$$

By phrasing both the ground state and one kink state observables as energy minimisation problems, standard techniques developed for the ground state can be applied to the study of the one kink state as well.

### 4.3.2 The Scalar Mass and Long-Distance Behaviour of $G_2(r)$

Lattice methods are typically used to evaluate equilibrium or ground state expectation values. As such, it is useful to have a method which can be used to extract the scalar mass  $m_S$  from observables of the ground state. In particular, the two-point function  $G_2(r)$  can be used at long distances to extract  $m_S$  by comparison with the two-point function of the non-interacting theory.

To see how the scalar mass can be extracted in a quantum field theory, we can consider the Källén-Lehmann spectral representation of the time ordered ground state two-point function which can be constructed quite generally for a Lorentz invariant theory [52]. This representation relates the full two-point function to the two-point function of the non-interacting theory, specifically the Feynman propagator  $D_F(x - y; M^2)$  via

$$\langle \Omega | T \phi(x) \phi(y) | \Omega \rangle = \int_0^\infty \frac{dM^2}{2\pi} \rho(M^2) D_F(x - y; M^2) , \quad (4.13)$$

where  $x$  and  $y$  are space-time coordinates,  $\rho(M^2)$  is the spectral density given by

$$\rho(M^2) = \sum_\lambda (2\pi) \delta(M^2 - m_\lambda^2) | \langle \Omega | \phi(0) | \lambda_0 \rangle |^2 \quad (4.14)$$

$$= \sum_\lambda (2\pi) \delta(M^2 - m_\lambda^2) Z \quad (4.15)$$

and  $|\lambda_0\rangle$  is a zero-momentum energy eigenstate. We can evaluate the Feynman propagator easily in  $D = (1 + 1)$  at equal times to give

$$D_F(r; M^2) = \frac{1}{2\pi} K_0(Mr) , \quad (4.16)$$

where  $K_0(z)$  is a modified Bessel function of the second kind. The equal time two-point function can then be written as

$$G_2(r) = \int_0^\infty \frac{dM^2}{4\pi} \rho(M^2) K_0(Mr) . \quad (4.17)$$

If the spectrum contains an isolated pole, then we can extract this contribution and write schematically

$$G_2(r) = \frac{Z}{(2\pi)^2} K_0(m_S r) + \int_{4m_S^2}^\infty \frac{dM^2}{4\pi} \rho(M^2) K_0(Mr) . \quad (4.18)$$

This suggests that at sufficiently long distances, the non-interacting form of the two-point function will be dominant and depend on the dimensionless combination  $m_S r$ .

The above arguments motivate the use of the ansatz

$$G_2(r) = AK_0(m_S r) \quad (4.19)$$

to estimate the scalar mass using a lattice approximation to  $G_2(r)$ . This can be achieved by taking the appropriate ratios (finite differences) to cancel overall factors as

$$\frac{G_2(r+1)}{G_2(r)} = \frac{K_0(m_S(r+1))}{K_0(m_S r)} . \quad (4.20)$$

This equation can then be solved numerically to extract  $m_S(r)$  which depends on  $r$  due the fact that  $G_2(r)$  is not a pure Bessel function. Following the previous arguments, we can expect for some initial  $r \lesssim \xi$  the value of  $m_S(r)$  will vary due to lattice effects and higher  $M^2$  eigenstate contributions, before becoming uniform such that  $m_S$  can be extracted (in practice, the uniform region must be selected by some criteria e.g. the gradient of  $m_S(r)$  falling below some specified tolerance, with  $m_S$  then estimated by averaging over the selected region).

If there is an additional infrared scale, e.g.  $L$ , then the behaviour of  $G_2(r)$  will be modified at long-distances  $r \sim L$ . An estimate of  $m_S$  will then have to be made from an intermediate distance where  $m_S(r)$  is uniform so that an accurate estimate requires  $\xi \ll L$  such that the scales in the theory have the clear hierarchy  $a \ll \xi \ll L$ .

### 4.3.3 Extracting $m_S$ at Strong Couplings

When sufficiently close to the critical point within the symmetry broken phase, the lightest excitations will become kink-antikink pairs. This motivates the use of a Bessel-squared function ansatz for the two-point function

$$G_2(r) = AK_0(m_S r)^2 , \quad (4.21)$$

corresponding to the form for two non-interacting excitations. The behaviour of  $G_2(r)$  can be established more rigorously in the critical region by considering the critical behaviour of the classical  $D = 2$  Ising model as described by the field theory of Majorana fermions [27].

At strong couplings, the Bessel-squared ansatz can then be used in a similar way to the Bessel function form. In fact, both  $K_0(z)$  and  $K_0(z)^2$  have similar exponentially decaying asymptotic forms

$$K_0(z) \rightarrow e^{-z} \sqrt{\frac{1}{z}} , \quad (4.22)$$

$$[K_0(z)]^2 \rightarrow e^{-2z} \frac{1}{2z} . \quad (4.23)$$

As such, in principle either form can be used to estimate  $m_S$ . However, unlike  $K_0(z)$ , we can expect  $[K_0(z)]^2$  to be valid outside the asymptotic regime which is useful since then shorter distances of  $G_2(r)$  will need to be approximated.

## 4.4 Real-Space Fock Basis

### 4.4.1 Creation and Annihilation Operators

The momentum-space field eigenbasis is a natural choice for mean field theory and semi-classical approximations. However, to go beyond these it is better to pick a numerically stable basis of real space harmonic oscillators [53]. Real space creation and annihilation operators for the  $\phi^4$  lattice theory can be introduced as

$$\begin{aligned} \phi_x &= \frac{1}{\sqrt{2}} (a_x^\dagger + a_x) , \\ \tilde{\pi}_x &= \frac{i}{\sqrt{2}} (a_x^\dagger - a_x) , \end{aligned} \quad (4.24)$$

such that the canonical commutation relation (4.3) becomes

$$[a_x, a_y^\dagger] = \delta_{x,y} . \quad (4.25)$$

In this parametrisation, a natural basis set is given by the tensor products  $|\mathbf{n}\rangle = |n_1\rangle \otimes |n_2\rangle \otimes \dots \otimes |n_N\rangle$  where  $|n_x\rangle$  are the eigenstates of the number operator  $N_x = a_x^\dagger a_x$  at each site. In terms of the creation and annihilation operators, the number eigenstate of site  $x$  is given by

$$|n_x\rangle = \frac{1}{\sqrt{n_x!}} (\hat{a}^\dagger)^{n_x} |0_x\rangle , \quad (4.26)$$

$$a_x |0_x\rangle = 0 . \quad (4.27)$$

For a finite size system, states are now labelled by a  $N$ -tuple  $\mathbf{n} = (n_1, n_2, n_3, \dots, n_N)$  with  $n_x \in \mathbb{Z}$  and a general state  $|\psi\rangle$  can be expanded as

$$\begin{aligned} |\psi\rangle &= \sum_{n_1=0}^{\infty} \dots \sum_{n_N=0}^{\infty} \langle n_1 n_2 \dots n_N | \psi \rangle |n_1 n_2 \dots n_N\rangle \\ &= \sum_{\mathbf{n}} \psi_{\mathbf{n}} |\mathbf{n}\rangle , \end{aligned} \quad (4.28)$$

where the state coefficient  $\psi_{\mathbf{n}}$  (wavefunction) now specifies the state in this basis.

The action of the creation and annihilation operators  $a_x^\dagger, a_x$  on the element  $|n_x\rangle$  is

$$\begin{aligned} a_x |n_x\rangle &= \sqrt{n_x} |n_x - 1\rangle , \\ a_x^\dagger |n_x\rangle &= \sqrt{n_x + 1} |n_x + 1\rangle , \end{aligned} \quad (4.29)$$

and can be applied recursively to calculate the action of any product of field operators on basis states, from which one can easily calculate the matrix elements. The matrix elements of the field operators in this basis are given by

$$\langle m_x | \phi_x | n_x \rangle = \frac{\sqrt{n_x + 1}}{\sqrt{2}} \langle m_x | n_x + 1 \rangle + \frac{\sqrt{n_x}}{\sqrt{2}} \langle m_x | n_x - 1 \rangle , \quad (4.30)$$

$$\langle m_x | \pi_x | n_x \rangle = i \frac{\sqrt{n_x + 1}}{\sqrt{2}} \langle m_x | n_x + 1 \rangle - i \frac{\sqrt{n_x}}{\sqrt{2}} \langle m_x | n_x - 1 \rangle , \quad (4.31)$$

with other operators in the Hamiltonian (4.2) being found in a similar manner.

#### 4.4.2 Boson Number Truncation

So far, the  $\phi^4$  lattice theory has been written as a set of coupled harmonic oscillators. To proceed with numerics, it is helpful to introduce an additional cutoff  $d$  that, like the IR cutoff  $L$ , truncates the theory down to a smaller Hilbert space. In this case, the cutoff limits the maximum number of bosons at any site to the value  $d - 1$  so that the total Hilbert-space dimension is finite when including the IR cutoff  $L$  and equal to  $d^N = d^{L/a}$ .

In the field eigenbasis, the associated error in the use a similar of basis truncation can be bound rigorously [26]. In that case, the state  $|\psi\rangle$  is approximated by another state  $|\psi_{\text{trunc}}\rangle$  where  $|\psi_{\text{trunc}}\rangle$  has no support on the basis elements that are

to be removed by the truncation. In the field eigenbasis

$$|\psi\rangle = \int \mathcal{D}[\Phi_x] \psi(\Phi_1, \Phi_2, \dots, \Phi_N) |\Phi_1, \Phi_2, \dots, \Phi_N\rangle, \quad (4.32)$$

$$|\psi_{\text{trunc}}\rangle = \int \mathcal{D}[\Phi_x] \psi_{\text{trunc}}(\Phi_1, \Phi_2, \dots, \Phi_N) |\Phi_1, \Phi_2, \dots, \Phi_N\rangle, \quad (4.33)$$

where  $\psi_{\text{trunc}}(\Phi_1, \Phi_2, \dots, \Phi_N) = 0$  if any  $\Phi_x \notin [-\Phi_{\text{max}}, \Phi_{\text{max}} : \delta\Phi]$ . Equivalently, the integral can be written as a finite sum so that

$$|\psi_{\text{trunc}}\rangle = \sum_{\{\Phi\}} \psi_{\text{trunc}}(\Phi_1, \Phi_2, \dots, \Phi_N) |\Phi_1, \Phi_2, \dots, \Phi_N\rangle \quad (4.34)$$

and the state can be considered as an element of the restricted Hilbert space  $\mathbb{C}^{d^N}$  where  $d$  is the number of elements in the local basis set  $\Phi_x \in [-\Phi_{\text{max}}, \Phi_{\text{max}} : \delta\Phi]$ .

The error associated with this approximation can then be quantified as  $\epsilon = 1 - \langle \psi | \psi_{\text{trunc}} \rangle$  and this may be bound by the values of  $\langle \psi | \phi_x^2 | \psi \rangle$  and  $\langle \psi | \pi_x^2 | \psi \rangle$  or alternatively the energy expectation value  $E = \langle \psi | H | \psi \rangle$ . This shows that this truncation corresponds to an additional UV cutoff in the expected way and that lower energy states will require fewer basis states (i.e. a lower value of  $d$ ) for an accurate approximation.

Since we will not be working in the field eigenbasis and in practice the rigorous bounds provided tend to be far more restrictive than necessary, we will only use these results to provide intuition concerning the effect of basis truncation in the real space Fock basis. In particular, these results suggest that computing the field expectation values such as  $\langle \psi | \phi_x^2 | \psi \rangle$  and  $\langle \psi | \pi_x^2 | \psi \rangle$  can provide a useful measure of the accuracy of approximations and in practice we will simply look for convergence in these and other observables of interest to indicate that enough basis states have been kept for a reasonable approximation.

A simple Fock-space basis truncation is achieved by keeping the first  $d$  basis states at each site. A state can then be expressed as

$$|\psi\rangle = \sum_{n_1=0}^{d-1} \dots \sum_{n_N=0}^{d-1} \langle n_1 n_2 \dots n_N | \psi \rangle |n_1 n_2 \dots n_N\rangle, \quad (4.35)$$

and this state can be considered either as one in the larger Hilbert space with zero overlap with elements outside the basis set, or as the state of a valid quantum theory with some smaller Hilbert space of dimension  $d^N$ .

## 4.5 Calculations in the Hamiltonian Lattice Framework

In the Hamiltonian lattice framework, we can approximate the low energy, low momentum observables of a QFT using standard quantum many body physics techniques. In principle, with the two UV cutoffs  $a, d$  and the IR cutoff  $L$  making the dimension of the Hilbert space finite, the theory can be studied numerically-exactly. Picking a basis and using a matrix-vector representation for the operators and states, then one can e.g. solve the energy minimisation problems for the ground state and one-kink state or exactly diagonalise the Hamiltonian for access to the full spectrum of the lattice theory. However, this approach is severely limited as the dimension of the lattice Hilbert space increases exponentially in the number of lattice sites. This means that firstly it will not even be possible to store a state or Hamiltonian with a large number of sites on a computer. More important in practice, the algorithms used to extract the physics from this representation (i.e. the diagonalisation or minimisation techniques) have a time-cost scaling with the size of the vectors/matrices so these will provide an even worse bottleneck. Therefore, such computational methods require very severe truncations to the  $\phi^4$  theory via the cutoff  $L$  and so are highly restrictive.

If one is not interested in the full spectrum e.g. for equilibrium ground-state calculations, it is possible to improve on this computational limitation somewhat. For example, one can target just the ground-state using sparse methods or exploit certain symmetries, though these methods are still fairly limited.

Alternatively, since one is often only interested in certain low energy observables, one can make additional truncations to reduce computational costs further while also being structured so as to capture the physics of interest. This is the typical approach in quantum-many-body theory and can be applied quite directly to quantum field theory through the Hamiltonian lattice regularisation framework outlined in this chapter.

# Chapter 5

## Tensor Network Representations

### 5.1 Introduction

Tensor network techniques provide a strategy for the approximation of lattice theories by first representing states, operators and observables as tensor networks, i.e. as sets of tensors contracted in a specified pattern, rather than as vectors and matrices as usual. The advantage of this is that the tensor network representations (TNR) are associated to a natural truncation, corresponding to limiting the size of the tensors in the network, that can be used to make computations feasible while still capturing desired physics. In fact, in some cases TNR can be constructed so that it is possible to truncate a theory efficiently, ensuring computational costs rise only polynomially in the number of lattice sites  $N$ , while still capturing the low energy physics of the theory numerically-exactly.

The key example of this is given by the matrix product state (MPS) TNR that can be used to numerically-exactly represent the ground states of gapped, local lattice Hamiltonians in one-dimension with a number of parameters rising only polynomially in  $N$  [54, 55]. Similar rigorous results hold in a few other cases and, for example, higher-dimensional ground-states can sometimes be represented by projected-entangled-pairs-states (PEPS) while thermal states can be efficiently represented by the matrix product operator (MPO) TNR assuming an additional bound in the density of states in both cases [56, 57]. The MPO can also be used to represent operators efficiently, such as the lattice Hamiltonian, so long as the operators are sufficiently “local” in the sense of the range of interaction terms present in them [58].

The physical reason that TNR can be used to efficiently capture the low energy physics of such lattice theories is that the low energy states of local theories are

extremely atypical. Such states manifest this locality in a number of ways and one familiar property is short range correlations. In one-dimension this corresponds exactly to another manifestation of locality: the entanglement area law [59].

Tensor network representations are constructed to mimic the entanglement structure of low energy states and are specifically designed so that when truncated they obey certain low entanglement laws e.g. the entanglement area law. While this does allow the exact representation of certain states, in practice the use of TNR goes well beyond this and more generally they provide a natural way to perform computationally efficient low entanglement approximations. These approximations are controlled by a cutoff parameter  $\chi$ , that determines the computational efficiency by limiting the sizes of tensors in the TNR, corresponding to some physical limitation in the amount of entanglement being kept. The cutoff can be removed by allowing it to scale exponentially with the number of lattice sites  $\chi \sim d^N$  (which we sometimes denote as  $\chi \rightarrow \infty$ ) allowing comparison with other methods when  $N$  is sufficiently small. Thus, the use of a TNR and an “entanglement cutoff”  $\chi$  constitutes the implementation a low entanglement, low energy effective theory and we can expect that the low entanglement physics - which is often the relevant physics at low energies - will be well approximated while the high entanglement physics - hopefully irrelevant in the situations of interest - is lost.

To put tensor network methods in context as a quantum field theory technique, we can compare this approach to that of numerical evaluation of the lattice path integral i.e. the Lagrangian lattice regularisation. In the path integral case, observables of the field theory are represented by a multi-dimensional integral. A finite size spacetime lattice then provides a UV regularisation and truncation of the integral, which reduces the degrees of freedom to a computationally feasible number. This truncation can be removed to recover the full theory by adjusting the lattice size and spacing. Additionally, the truncation is physically well motivated since its impact on the energy-momentum modes of the theory is well understood and the lattice theory provides a low energy effective theory. Finally, observables can be evaluated using a Monte Carlo approximation. Since the errors coming from this approximation are purely statistical, they are well controlled and the procedure as a whole leads to a clear and powerful computation scheme, albeit one limited to certain equilibrium observables.

As a comparison, tensor networks provide an alternative representation for observables of the quantum field theory. In this case, in addition to the spatial lattice which provides the regularisation, there is the truncation parameter  $\chi$  associated with the size of the tensors. The truncation can be removed by adjusting  $\chi$  and is

physically well motivated since it can be linked to the level of entanglement entropy in the system. Thus, these techniques can be understood as providing a low entanglement effective theory. Observables can then be calculated by contracting the relevant tensor network and in some cases (such as low dimensions) it is possible to calculate observables directly, while in others Monte Carlo sampling can sometimes be used. More generally, since the TNR already constitutes a low entanglement approximation, it is conceptually consistent to introduce additional low entanglement approximations in order to evaluate observables and this is a typical approach e.g. in spatial dimensions greater than one.

In this chapter, we will introduce the tensor network representations that we will use later: the MPS and MPO. These representations allow for the efficient expression of a number of states, operators and observables of interest. While in this chapter we will focus on exact examples that are later used or provide some intuition for the representation, the primary use of tensor networks is as an approximation scheme and we will introduce some algorithms to achieve this in Chapter 6.

## 5.2 Representation of The Lattice Hamiltonian as a Matrix Product Operator

### 5.2.1 Matrix Product Operators

To introduce the concept of tensor network representations, it is helpful to start by representing the lattice Hamiltonians (4.8) and (4.10) in the matrix product operator TNR. In addition to being of practical importance for the efficiency of algorithms, this provides some intuition for the relationship between locality of the object, in this case the range of interaction of the operator, and the efficiency of the TNR for that object.

An MPO consists of expressing the operator of interest as the product of matrices  $\mathbf{W}_x$ , one per lattice site, where the entries of the matrix consist only of operators that act as identity on all sites but  $x$ . Explicitly, the (one-dimensional) MPO representation of an operator  $\hat{O}$  is given by

$$\hat{O} = \text{tr} \left( \prod_{x=1}^N \mathbf{W}_x \right), \quad (5.1)$$

where the matrices  $\mathbf{W}_x$  are of size  $(\chi_W, \chi_W)$  and have components

$$(\mathbf{W}_x)_{\alpha_x, \beta_x} = \hat{O}_x^{(\alpha_x, \beta_x)} . \quad (5.2)$$

In other words, each matrix is formed of  $\chi_W^2$  operators that act only on site  $x$ . The non-local (multi-site) interaction terms of the operator  $\hat{O}$  are then encoded in the one-dimensional nearest-neighbour structure of the matrix product operator. When this nearest-neighbour structure correctly corresponds to the interaction structure of the operator being represented, only small matrices will be required. However, in the general case where the interactions are not short range at all e.g. if  $\hat{O}$  was a two-dimensional lattice Hamiltonian being represented in one-dimension, then the size of  $\chi_W$  will grow exponentially with the number of lattice sites. This corresponds to the fact that the MPO structure completely fails to capture the real-space interaction structure of the operator in this case and MPO defined as in (5.1) are best suited to the representation of one-dimensional operators with short range interactions.

### 5.2.2 MPO Representation of $\tilde{H}$

To represent the lattice Hamiltonian  $\tilde{H}[\phi]$  (4.2) as an MPO it is helpful to first simplify the expression by collecting all one site terms into a single operator  $h_x$ . The Hamiltonian, ignoring the boundary conditions for the moment, then takes the form

$$\tilde{H}[\phi] = \sum_x -\phi_x \phi_{x+1} + h_x , \quad (5.3)$$

with

$$\begin{aligned} h_x &= \frac{1}{2} \tilde{\pi}_x^2 + \frac{2+\tilde{\mu}_0^2}{2} \phi_x^2 + \frac{\tilde{\lambda}_0}{4!} \phi_x^4 \\ &= \frac{1}{2} \tilde{\pi}_x^2 + \phi_x^2 + V(\phi_x)_x . \end{aligned} \quad (5.4)$$

Since this has the same nearest neighbour structure as the Ising model Hamiltonian we can use the same MPO construction methods as in that case [60]. To see how a correct MPO representation can be found, we can consider building the Hamiltonian up iteratively from the rightmost site to the left. The correct choice of matrix for

the bulk of the Hamiltonian is given by

$$\mathbf{W}_x = \begin{pmatrix} \mathbb{1} & 0 & 0 \\ -\phi_x & 0 & 0 \\ h_x & \phi_x & \mathbb{1} \end{pmatrix}. \quad (5.5)$$

This matrix is tri-diagonal so that  $\mathbf{W}_x \mathbf{W}_{x+1}$  is given by

$$\mathbf{W}_x \mathbf{W}_{x+1} = \begin{pmatrix} \mathbb{1} & 0 & 0 \\ -\phi_x & 0 & 0 \\ h_x + h_{x+1} - \phi_x \phi_{x+1} & \phi_{x+1} & \mathbb{1} \end{pmatrix} \quad (5.6)$$

and the general structure of the matrices remains the same while the Hamiltonian is built up iteratively in the bottom-left corner. It then only remains to pick a single boundary term (e.g. at site  $x = 1$ ) to correctly select out the bottom-left corner, where the bulk of the Hamiltonian has been built up, and encode any remaining boundaries using the trace appearing in the MPO definition (5.1). For PBC a consistent choice is

$$\mathbf{W}_1 = \begin{pmatrix} 0 & \phi_1 & \mathbb{1} \\ 0 & 0 & -\phi_1 \\ 0 & 0 & h_1 \end{pmatrix}, \quad (5.7)$$

while for TPBC we can choose

$$\mathbf{W}_1 = \begin{pmatrix} 0 & -\bar{\phi}_1 & \mathbb{1} \\ 0 & 0 & -\bar{\phi}_1 \\ 0 & 0 & h_1 \end{pmatrix} \quad (5.8)$$

and open boundary conditions (OBC) can be encoded by setting  $\mathbf{W}_1$  and  $\mathbf{W}_N$  to be vectors  $\mathbf{W}_1 = w_1^T, \mathbf{W}_N = w_N$  e.g. by the choice

$$w_1^T = \begin{pmatrix} h_1 & \phi_1 & \mathbb{1} \end{pmatrix}, \quad (5.9)$$

$$w_N = \begin{pmatrix} \mathbb{1} \\ -\phi_N \\ h_N \end{pmatrix}. \quad (5.10)$$

The above construction demonstrates that indeed the lattice Hamiltonian can be written efficiently as an MPO. The fact that only small matrices with size  $\chi_W = 3$  were required reflects the fact that the real-space structure of the interactions in the



The contraction of two tensors over a particular index can then be indicated by simply connecting the corresponding legs of the two shapes. For example, the OBC MPO representation of an operator can be drawn as a set of rank-4 tensors connected in nearest-neighbour fashion with two rank-3 boundary tensors,

$$O_{\mathbf{n},\mathbf{m}} = \begin{array}{c} | \\ | \\ | \\ | \\ | \\ \hline \square - \square - \square - \square - \square \\ | \\ | \\ | \\ | \\ | \end{array} , \quad (5.14)$$

where the OBC mean that the first and last tensors have only three legs. Often, we will be more interested in PBC MPO but may still draw OBC diagrams for convenience.

In the rank-4 tensor  $W_x$  of size  $(d, d, \chi_W, \chi_W)$ , the first two indices provide the *physical indices* corresponding to the local basis state ket  $|n_x\rangle = |0\rangle, |1\rangle, \dots, |d-1\rangle$  and bra  $\langle m_x|$ . These physical indices are drawn vertically in the TN diagrams and we have chosen the convention that downwards legs corresponding to the ket and upwards legs corresponding to the bra. The latter two indices provide the *internal* or *virtual* degrees of freedom and are drawn horizontally. All the internal indices are contracted over while the physical indices remain uncontracted.

While the ideas of locality were used quite intuitively in the construction of the MPO representations, this idea can be made precise in the corresponding matrix product state (MPS) representation of states which clarifies the link between an efficient TNR for an object and its locality in the sense of obeying a low entanglement law.

## 5.3 Matrix Product State Representations

### 5.3.1 Definition of MPS

Similar to the definition of the MPO, the matrix product state representation for a state  $|\psi\rangle$  is given by the form

$$|\psi\rangle = \text{tr} \left( \prod_x \mathbf{M}_x \right) , \quad (5.15)$$

where the components of the  $(\chi, \chi)$  matrices  $\mathbf{M}_x$  are states in the local Hilbert space corresponding to that site i.e.

$$(\mathbf{M}_x)_{\alpha_x, \beta_x} = |\psi_x^{(\alpha_x, \beta_x)}\rangle . \quad (5.16)$$

Taking the matrix product of  $\mathbf{M}_x$  at different sites in (5.15) now generates superpositions of states over larger numbers of sites, with the understanding that the components should be combined via a tensor product as in the MPO case. In a given basis, the MPS representation of the wavefunction is given by

$$\psi_{\mathbf{n}} = \text{tr} \left( \prod_x \mathbf{M}_x^{n_x} \right) , \quad (5.17)$$

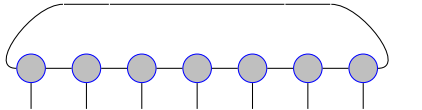
where the components of  $\mathbf{M}_x^{n_x}$  are

$$(\mathbf{M}_x^{n_x})_{\alpha_x, \beta_x} = \langle n_x | \psi_x^{(\alpha_x, \beta_x)} \rangle \quad (5.18)$$

$$= (M_x)_{\alpha_x, \beta_x}^{n_x} , \quad (5.19)$$

so that the MPS can be considered a tensor network of rank-3 tensors with size  $(d, \chi, \chi)$  where  $\chi$  is often referred to as the “bond-dimension”.

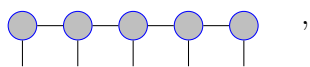
The MPS diagrams follow simply as for the MPO. For example, the PBC lattice MPS with  $N = 7$  sites is represented by

$$\psi_{\mathbf{n}} = \text{tr} \left( \prod_{x=1}^7 \mathbf{M}_x^{n_x} \right) , \quad (5.20)$$


while an MPS with OBC can be used by considering the first and last tensors as rank-2 tensors so that

$$\psi_{\mathbf{n}} = (m_L^{n_1})^T \left( \prod_{x=2}^{N-1} \mathbf{M}_x^{n_x} \right) m_R^{n_N} , \quad (5.21)$$

where  $m_L^{n_1}, m_R^{n_N}$  are of size  $(d, \chi)$  and the trace is no longer needed. As for the MPO, the diagrams for OBC MPS are somewhat simpler than their PBC counterparts e.g. for  $N = 5$

$$\psi_{\mathbf{n}} = \text{tr} \left( \prod_{x=1}^5 \mathbf{M}_x^{n_x} \right) , \quad (5.22)$$


so that we will use OBC in MPS diagrams for convenience, though calculations will

tend to involve PBC. Once again, the first index of the MPS is the physical local basis index (drawn downwards in this convention) and the virtual indices are fully contracted over.

### 5.3.2 Entanglement in an MPS

On a lattice of size  $N$ , the number of parameters required to specify an MPS is  $\mathcal{O}(Nd\chi^2)$ . As such, the truncation parameter  $\chi$  controls the cost of the representation and must be kept small (must not rise exponentially with  $N$ ) to ensure computational efficiency. This truncation parameter can be linked directly to the maximum allowed entanglement of a state represented by an MPS, thus providing a clear physical understanding of the truncation.

The entanglement entropy  $S_{\mathcal{A}}$  of a subsystem  $\mathcal{A}$  under a bipartition of the full system is given by the von Neumann entropy of the reduced density matrix for the subsystem:

$$S_{\mathcal{A}} = -\text{tr} [\rho_{\mathcal{A}} \log_2 \rho_{\mathcal{A}}] . \quad (5.23)$$

For a generic state, the entanglement entropy grows as the volume of the region under consideration  $S_{\mathcal{A}} \sim V_{\mathcal{A}}$  while for states obeying an entanglement area law it grows with the boundary of the region i.e.  $S_{\mathcal{A}} \sim \partial V_{\mathcal{A}}$ . In one-dimension, area law states are then particularly simple and have  $S_{\mathcal{A}} \sim \text{const}$ .

The investigation of the entanglement in physically interesting quantum many body states has been of significant interest with area laws being found for a number of important cases [61, 62]. There has also been interest within the context of quantum field theory. For example, the entanglement entropy of ground-states in perturbed/massive conformal field theories has been calculated in  $D = (1 + 1)$  on the lattice [63]. In that case, the entanglement entropy diverges logarithmically with size of the subregion in lattice units

$$S_{\mathcal{A}} \sim \frac{c}{3} \log_2 \left( \frac{V_{\mathcal{A}}}{a} \right) , \quad (5.24)$$

where  $c$  is the central charge and  $\xi \gg V_{\mathcal{A}}$ . However, when  $V_{\mathcal{A}} \gg \xi$  then

$$S_{\mathcal{A}} \sim \frac{c}{6} \log_2 \left( \frac{\xi}{a} \right) , \quad (5.25)$$

which is a one-dimensional area law giving an example of the connection between correlation length and entanglement in one-dimension. The ground-state of the  $\phi^4$

QFT has also been studied [64]. In the non-interacting case the entanglement area law has both UV divergent and finite pieces

$$S_A \sim \frac{\partial V_A}{a^{D_S-1}} + \gamma_{D_S} \frac{\partial V_A}{\xi^{D_S-1}}, \quad \text{for } D_S \text{ even}, \quad (5.26)$$

$$S_A \sim \frac{\partial V_A}{a^{D_S-1}} + \gamma_d \frac{\partial V_A}{\xi^{d-1}} \log_2(\xi/a), \quad \text{for } D_S \text{ odd}, \quad (5.27)$$

where  $\gamma_d$  is a constant given in [64]. The divergent piece, which is independent of the physical features (e.g. particle mass), can be cancelled by considering differences in the entanglement entropy and it is therefore such differences which can be considered the physical observable associated with the entanglement entropy in QFT [65]. The effect of interactions has also been studied at weak-coupling. Using perturbation theory, the free-field formulas (5.27) were found to hold with mass renormalisation [66] while in [67] entanglement was found to decrease monotonically with coupling in  $D = (1 + 1)$  and  $D = (2 + 1)$  using variational Gaussian states.

For an MPS, the entanglement can be evaluated by making use of a Schmidt decomposition and manipulating the MPS form [68]. For a block of contiguous lattice sites, the maximum entanglement entropy of an MPS is bound logarithmically in its bond-dimension

$$S_A \leq C \log \chi, \quad (5.28)$$

where  $C$  is some constant. In other words, matrix product states obey a one-dimensional entanglement area law. Thus, to represent a general state in one spatial dimension an MPS requires  $\chi \sim e^N$  and so is computationally inefficient. However, as one might expect from the scaling (5.28), MPS can in fact represent one-dimensional area law states efficiently. Naively, this simply requires the highly efficient scaling  $\chi \sim \text{const}$ , i.e. independently of the number of sites. More rigorously, it can be shown that  $\chi \sim \text{Poly}(N)$  is sufficient to represent all area law states [69] and, as a special case, ground-states of gapped systems can be represented with a bond-dimension that scales sub-linearly [55].

### 5.3.3 MPS Representation of Fixed Boson Number States and MPS-MPO products

To illustrate the MPS representation, states of fixed boson number  $N_{\text{Tot}} = \sum_x N_x = \sum_x a_x^\dagger a_x$  can be built up explicitly. Since it is a unentangled, i.e. a product state, the zero-boson number state  $|0\rangle = \bigotimes_x |0_x\rangle$  (4.27) can be trivially

represented as an MPS with  $\chi = 1$  by setting

$$(\mathbf{M})_{\alpha,\beta} = |0_x\rangle \quad (5.29)$$

for all sites (for  $\chi = 1$  PBC and OBC MPS are identical). An MPS representation for translationally invariant states with one boson, given by (up to normalisation)

$$\begin{aligned} |1_p\rangle &= a_p^\dagger |0\rangle \\ &= \sum_x e^{ipx} a_x^\dagger |0\rangle \\ &= \sum_x e^{ipx} |\dots 0_{x-1}, 1_x, 0_{x+1}, \dots\rangle, \end{aligned} \quad (5.30)$$

can be constructed with  $\chi = 2$ . An explicit form can be found in a similar manner as for the MPO representation of  $\tilde{H}$  using bulk matrices

$$\mathbf{M}_x = \begin{pmatrix} |0_x\rangle & 0 \\ e^{ipx} |1_x\rangle & |0_x\rangle \end{pmatrix}, \quad (5.31)$$

which multiply as

$$\mathbf{M}_x \mathbf{M}_{x+1} = \begin{pmatrix} |0_x 0_{x+1}\rangle & 0 \\ e^{ipx} |1_x 0_{x+1}\rangle + e^{ip(x+1)} |0_x 1_{x+1}\rangle & |0_x 0_{x+1}\rangle \end{pmatrix}, \quad (5.32)$$

so that again the state is built up in the lower-left corner and a suitable boundary matrix can be chosen to complete the  $\chi = 2$  MPS representation.

In order to build up  $m$ -boson representations, it is helpful to note that the creation operator  $a_p^\dagger$  can itself be expressed as an MPO with  $\chi_W = 2$  where the bulk matrices are

$$\mathbf{W}_x = \begin{pmatrix} \mathbb{1} & 0 \\ e^{ipx} a_x^\dagger & \mathbb{1} \end{pmatrix}. \quad (5.33)$$

and the boundary matrix can be chosen as

$$\mathbf{W}_1 = \begin{pmatrix} \mathbb{1} & 0 \\ e^{ip} a_1^\dagger & 0 \end{pmatrix}, \quad (5.34)$$

picking  $x = 1$  as the arbitrary boundary site.

Writing the one-boson state as  $|1_p\rangle = a_p^\dagger |0\rangle$  shows that the  $\chi = 2$  MPS representation of  $|1_p\rangle$  is equivalent to a two-layer MPS-MPO tensor network with

$\chi = 1, \chi_W = 2$ , which can be represented diagrammatically as

$$|1_p\rangle = a_p^\dagger |0\rangle = \begin{array}{c} \textcircled{\bullet} \text{---} \textcircled{\bullet} \text{---} \textcircled{\bullet} \text{---} \textcircled{\bullet} \text{---} \textcircled{\bullet} \\ | \\ \blacksquare \text{---} \blacksquare \text{---} \blacksquare \text{---} \blacksquare \text{---} \blacksquare \\ | \\ \text{---} \end{array} . \quad (5.35)$$

This equivalence between the  $\chi = 2$  MPS representation and a two-layer representation can be seen explicitly by contracting the two-layer TNR vertically i.e. by applying the operator  $a_p^\dagger$  to the state  $|0\rangle$  in the MPO/MPS representation. Generally, the application of an MPO to an MPS can be written as

$$\begin{aligned} \hat{O} |\psi\rangle &= \text{tr} \prod_x \mathbf{W}_x \text{tr} \prod_x \mathbf{M}_x \\ &= \text{tr} \prod_x \mathbf{W}_x \otimes \prod_x \mathbf{M}_x \\ &= \text{tr} \prod_x \mathbf{W}_x \otimes \mathbf{M}_x \\ &= \text{tr} \prod_x \tilde{\mathbf{M}}_x , \end{aligned} \quad (5.36)$$

demonstrating that an MPO-MPS product is in general equivalent to an MPS with a higher bond-dimension  $\chi' = \chi_W \chi$  and parametrised by matrices  $\tilde{\mathbf{M}}_x$  with components

$$\begin{aligned} (\tilde{\mathbf{M}}_x)_{\alpha_1 \alpha_2, \beta_1 \beta_2} &= (\mathbf{W}_x)_{\alpha_1, \beta_1} (\mathbf{M}_x)_{\alpha_2, \beta_2} \\ &= \hat{O}^{(\alpha_1, \beta_1)} |\psi^{(\alpha_2, \beta_2)}\rangle . \end{aligned} \quad (5.37)$$

In this sense, MPO with  $\chi_W > 1$  can increase the entanglement of the state they are applied to (though note that there might be some redundancy in the description of the MPS so that  $\chi'$  really only provides an upper bound on the bond-dimension necessary to represent the state in question).

States with  $m$ -bosons can then be built up in a similar manner and represented either as a  $m + 1$  layer TN or as an MPS with  $\chi = 2^m$ . For example, the two-boson states can be represented as

$$a_{p_1}^\dagger a_{p_2}^\dagger |0\rangle = \begin{array}{c} \textcircled{\bullet} \text{---} \textcircled{\bullet} \text{---} \textcircled{\bullet} \text{---} \textcircled{\bullet} \text{---} \textcircled{\bullet} \\ | \\ \blacksquare \text{---} \blacksquare \text{---} \blacksquare \text{---} \blacksquare \text{---} \blacksquare \\ | \\ \square \text{---} \square \text{---} \square \text{---} \square \text{---} \square \\ | \\ \text{---} \end{array} . \quad (5.38)$$

The high bond-dimension of the MPS representation of  $m$ -boson states suggests that these states are in fact highly entangled from the perspective of a one-dimensional area law. However, this does not mean that the states cannot be represented efficiently by a TNR. Indeed, the representation of the  $m$ -boson states as an  $m + 1$  layer network requires only a polynomial number of parameters. It is then how highly entangled a state is relative to a one-dimensional representation that will be of crucial importance for the computational efficiency of algorithms and it will be in this sense of low entanglement that we will focus, particularly since this coincides with the physical spatial dimension of the theories of interest here.

### 5.3.4 Uniform Matrix Product States

When dealing with translationally invariant states, translation symmetry can be enforced and exploited by using a uniform matrix product representation (uMPS). This MPS is constructed by simply requiring all tensors to be identical i.e.  $\mathbf{M}^{n_x}(x) = \mathbf{A}^{n_x}$  for all  $x = (1, \dots, N)$ . Since there is no spatial variation the uMPS can be defined in the infinite size limit  $N \rightarrow \infty$ , which we will assume unless otherwise specified. This is particularly useful since in this case the boundaries are irrelevant and OBC can be used which offer a number of computational advantages. The uMPS representation for states can be defined as

$$|\psi[A]\rangle = \sum_{\mathbf{n}} v_L^\dagger \left( \prod_{x=-\infty}^{+\infty} \mathbf{A}^{n_x} \right) v_R |\mathbf{n}\rangle, \quad (5.39)$$

where the notation  $|\psi[A]\rangle$  indicates the state is a uMPS and emphasises the fact that it is defined by  $d\chi^2$  parameters encoded in the single tensor  $A_{\alpha,\beta}^n$ . The boundary tensors  $v_L, v_R$  are of size  $(d, \chi)$  and act as vectors in the matrix product, encoding the (irrelevant) OBC.

## 5.4 Representation of Observables as Tensor Networks and Their Evaluation

### 5.4.1 Construction of Representation Using MPS and MPO

Using the MPO and MPS forms, it is possible to represent observables as TN in a simple way. Due to the completeness of both the MPS and MPO representations,



two MPS as

$$\langle \tilde{\psi} | \hat{O} | \psi \rangle = \begin{array}{c} \bullet \quad \bullet \quad \bullet \quad \bullet \quad \bullet \\ | \quad | \quad | \quad | \quad | \\ \blacksquare \quad \blacksquare \quad \blacksquare \quad \blacksquare \quad \blacksquare \\ | \quad | \quad | \quad | \quad | \\ \circ \quad \circ \quad \circ \quad \circ \quad \circ \end{array} \quad (5.43)$$

so that the observable is calculated by fully contracting the corresponding tensor network.

### 5.4.2 Exact Contractions of Quasi-One-Dimensional TNR

In the case that the TN is quasi-one-dimensional, it is possible to efficiently contract the tensor-network numerically-exactly. This can be achieved by choosing a contraction ordering that proceeds horizontally from the left or right boundary. A useful way to express this is in terms of transfer matrices, which can be done by defining the object  $E_B^A[O] = \sum_{i,j} \mathbf{A}^i \otimes \mathbf{O}^{i,j} \otimes (\mathbf{B}^*)^j$ , or  $E_B^A = \sum_i \mathbf{A}^i \otimes (\mathbf{B}^*)^i$  if no “operator” tensor is included, where  $A$  and  $B$  label the rank-3 tensors placed in the upper and lower positions respectively while  $O$  labels the rank-4 tensor. Diagrammatically we have

$$E_B^A = \begin{array}{c} \bullet \\ | \\ \circ \end{array} \quad (5.44)$$

and

$$E_B^A[O] = \begin{array}{c} \bullet \\ | \\ \blacksquare \\ | \\ \circ \end{array} \cdot \quad (5.45)$$

In this notation, the matrix element  $\langle \tilde{\psi} | \hat{O} | \psi \rangle$  is given by

$$\begin{aligned} \langle \tilde{\psi} | \hat{O} | \psi \rangle &= \text{tr} (E_{B_1}^{A_1}[O_1] E_{B_2}^{A_2}[O_2] \dots E_{B_N}^{A_N}[O_N]) \\ &= \text{tr} (\mathbf{E}_1 \mathbf{E}_2 \dots \mathbf{E}_N) \\ &= \text{tr} \left( \prod_x \mathbf{E}_x \right) . \end{aligned} \quad (5.46)$$

Viewing  $\mathbf{E}_x$  as matrix of size  $(\chi^2 \chi_W, \chi^2 \chi_W)$  the cost of this matrix multiplication would naively be  $\mathcal{O}(\chi^6 \chi_W^3)$ , though this can be lowered by exploiting the tensor network structure of the transfer matrices, see e.g. [68] for details.

### 5.4.3 Expectation Values with uMPS

Computations with uMPS are performed in a similar manner to the finite size MPS, though care has to be taken to remove the infrared divergences associated to the thermodynamic limit, see [71, 72] for details. The evaluation of expectation values can be illustrated using the transfer matrix notation (5.46). For example, the norm of a uMPS can be written as

$$\langle \psi[A] | \psi[A] \rangle = \text{tr} \left( \dots E_A^A E_A^A E_A^A \dots \right) , \quad (5.47)$$

where the ellipses represent an infinite product of transfer matrices, one per site. If the matrix  $E_A^A$  has a single dominant eigenvector  $\omega^0 = 1$  then one can write

$$\begin{aligned} \langle \psi[A] | \psi[A] \rangle &= \text{tr} (|R\rangle\langle L|) \\ &= 1 , \end{aligned} \quad (5.48)$$

where  $|R\rangle$  and  $\langle L|$  are the right and transposed left dominant eigenvectors of the matrix  $E_A^A$ , normalised such that  $\langle L|R\rangle = 1$ . If the dominant eigenvector  $\omega^0 \neq 1$  then normalisation can be achieved by scaling  $A \rightarrow A/\sqrt{\omega^0}$ . The expectation value of any local operator on some set of  $m$ -sites can then be evaluated in a similar manner taking the infinite product of transfer matrices  $E_A^A$  that occur on either side of the region on which  $\hat{O}$  has support. If we represent the operator  $\hat{O}$  with support on  $m$ -sites as an MPO and again assume that the transfer matrix has a single dominant eigenvector  $\omega_0 = 1$ , then we can write that

$$\begin{aligned} \langle \psi[A] | \hat{O} | \psi[A] \rangle &= \text{tr} \left( \dots E_A^A E_A^A [O_1] E_A^A [O_2] \dots E_A^A [O_m] E_A^A \dots \right) \\ &= \langle L | E_A^A [O_1] E_A^A [O_2] \dots E_A^A [O_m] | R \rangle . \end{aligned} \quad (5.49)$$

More generally, local expectation values of uMPS can be defined in this way so long as the transfer matrix has a single dominant eigenvector and its left and right dominant eigenvectors have full rank when written as matrices [71]. We will always assume this is the case and that the uMPS has been normalised unless specified otherwise. In this case, once the dominant eigenvectors of the transfer matrix have been determined, local expectation values such as (5.49) can be evaluated using the contraction strategies available for finite-size OBC MPS.

#### 5.4.4 Gauge Freedom of MPS and Boundary Conditions

Matrix product states, and tensor networks more generally, are associated to a simple gauge redundancy under the insertion of matrices at the point of contraction between two tensors. This freedom can be seen easily for MPS since any MPS can be equivalently rewritten by inserting identity matrices  $\mathbb{1}$  of size  $(\chi, \chi)$  between any of the rank-3 tensors. Decomposing the identities as  $\mathbb{1} = \mathbf{G}(x)^{-1}\mathbf{G}(x)$  then leads to a different MPS representation of the same state as

$$\begin{aligned}\psi_{\mathbf{n}} &= \text{tr} \left( \prod_x \mathbf{G}(x) \mathbf{M}^{n_x}(x) \mathbf{G}^{-1}(x+1) \right) \\ &= \text{tr} \left( \prod_x \tilde{\mathbf{M}}^{n_x}(x) \right) .\end{aligned}\tag{5.50}$$

Equivalently, and more common in practice, one can think of performing a matrix decomposition on the tensors which will leave the matrix product unchanged. This gauge freedom can be exploited to give desirable properties to the MPS matrices which can simplify calculations and associated algorithms. The most common choice is that of left/right orthonormality where  $\mathbf{G}$  is chosen such that  $\mathbf{M}^n$  has the property

$$(\mathbb{1} | E_M^M = (\mathbb{1} | , \text{ (left-orthonormal) } , \tag{5.51}$$

$$E_M^M | \mathbb{1} \rangle = | \mathbb{1} \rangle , \text{ (right-orthonormal) } , \tag{5.52}$$

where the “identity vector”  $| \mathbb{1} \rangle$  simply contracts the two indices of the transfer matrix together when expressed in tensor form:

$$E_B^A | \mathbb{1} \rangle = \sum_i \mathbf{A}^i (\mathbf{B}^\dagger)^i . \tag{5.53}$$

We will refer to an MPS for which all matrices are left/right orthonormal as being in the left/right gauge and this gauge can be fixed by using e.g. singular value decompositions on the  $\mathbf{M}^n$  matrices. For OBC MPS this gauge choice simplifies calculations considerably as the boundary transfer matrices act like identity vectors on the adjacent matrices

$$E_{v_L}^{v_L} = (\mathbb{1} | , \text{ if left-orthonormal } , \tag{5.54}$$

$$E_{v_R}^{v_R} = | \mathbb{1} \rangle , \text{ if right-orthonormal } , \tag{5.55}$$

and products of transfer matrices in the same gauge simply reduce to the identity. Another standard gauge choice is the mixed/canonical gauge where to the left of a chosen site  $k$  (the centre site) all matrices are left-orthonormal while to the right all matrices are right-orthonormal. This choice simplifies the calculations of local expectation values where the operator of interest acts only on the centre site. All other sites surrounding the centre site can then be contracted trivially and the expectation value reduces to

$$\begin{aligned} \langle \psi | \hat{O}_k | \psi \rangle &= \text{tr} \left( E_{v_L}^{v_L} E_{M_1}^{M_1} \dots E_{M_k}^{M_k} [O_k] \dots E_{M_{N-2}}^{M_{N-2}} E_{v_R}^{v_R} \right) \\ &= (\mathbf{1} | E_{M_k}^{M_k} [O_k] | \mathbf{1} ) , \end{aligned} \quad (5.56)$$

so that only the tensor at site  $k$  contributes to the expectation value.

While we will mainly use PBC in finite size calculations where such simplifications cannot be made, similar gauge choices can improve the stability of algorithms even in the PBC case and so are still of significant interest. In the infinite size case, such gauge choices will be particularly powerful since OBC can be used without the strong boundary effects found in the finite size case. In the mixed gauge with centre site  $x$ , the uMPS can be written as

$$|\psi[A]\rangle = \sum_{\mathbf{n}} \dots \mathbf{A}_L^{n_{x-2}} \mathbf{A}_L^{n_{x-1}} \mathbf{A}_C^{n_x} \mathbf{A}_R^{n_{x+1}} \mathbf{A}_R^{n_x} \dots |\mathbf{n}\rangle , \quad (5.57)$$

where all tensors to the left of site  $x$  has been left-orthonormalised  $A \rightarrow A_L$  while to the right they have been right-orthonormalised  $A \rightarrow A_R$  which together result in  $A \rightarrow A_C$  on the centre site at  $x$ . Now denoting the transfer matrices corresponding to  $A_L$  and  $A_R$  (without operators inserted) as  $T_L$  and  $T_R$ , then the associated gauge conditions mean that for a normalised state these matrices have dominant left/right eigenvectors that act as the identity vector and in this case we can define

$$\begin{aligned} (\mathbf{1} | T_L &= (\mathbf{1} | \\ T_R | \mathbf{1} &= | \mathbf{1} \rangle \\ T_L | R &= | R \rangle \\ (L | T_R &= (L | . \end{aligned} \quad (5.58)$$

Therefore, the simplification of local expectation values found in the finite size mixed gauge case follows over to the infinite-size case with the boundaries acting as identity vectors only.

### 5.4.5 Low Entanglement Approximation of Higher Dimension Observables

As we have seen, it is often possible to represent interesting observables efficiently as two-dimensional tensor networks. In principle, these TN can be contracted vertically corresponding to the application of the MPO layers onto the MPS. However, this is generally inefficient since the MPS bond-dimension grows exponentially with the number of layers in the network. To evaluate such an observable represented in this manner, more truncations must be used. When applied sensibly, these truncations should correspond to extracting a “low entanglement approximation” for the observable. For example, one clear strategy is to repeatedly apply the MPO layers to the MPS but at each step truncate the MPS so that the computation is feasible and the entanglement remains limited. Similar strategies can be applied in  $D = (2 + 1)$  and there are a number of related relevant methods, see [73, 74] for reviews and examples. Alternatively, one can try more complicated schemes to extract a low entanglement approximation and recently this idea has been formalised by constructing renormalisation group transformations on tensor networks. These methods systematically simplify tensor networks, removing the high-entanglement degrees of freedom and producing a low-entanglement approximation to the observable in question [75, 76, 77].

# Chapter 6

## Low Entanglement Approximations with Tensor Networks

### 6.1 Introduction

While some observables can be represented and calculated exactly in an efficient manner using tensor networks, more generally they are used to provide powerful low-entanglement approximation schemes. This is primarily achieved by treating the tensor networks as variational ansatz for quantum states. The chosen form of the tensor network then restricts one to a subset of states (the variational manifold) and the entries of the tensors are treated as free parameters which specify a state in the manifold. To approximate a particular observable, the parameters are then chosen so that the corresponding state is approximated as well as possible by the ansatz. Equal-time observables can then be evaluated using the state approximation leading to an approximation for the observable  $O(\chi)$ . Since the TNR are complete, when the truncation is removed  $\chi \rightarrow \infty$  the approximation will agree with its true value. We can then consider some threshold  $\chi^*$  for which the difference between the true value and approximation  $|O(\infty) - O(\chi)|$  is sufficiently small. The required  $\chi^*$  will depend on the observable/system in question with “higher entanglement” observables requiring higher  $\chi^*$  to approximate.

For example, to approximate the entanglement entropy of a state with correlation length  $\xi$  that is described by a conformal field theory (CFT), we can expect from the CFT result for the entanglement entropy (5.25) and corresponding MPS result (5.28) that  $\chi^* \sim \tilde{\xi}^p$  where  $p$  is some positive number. Another example is

given by the equal time ground-state two-point function

$$G_2(r) = \langle \Omega | \phi(x) \phi(x+r) | \Omega \rangle . \quad (6.1)$$

Using an MPS, this can be approximated by first approximating the ground-state  $|\Omega(\chi)\rangle$  and then calculating

$$G_2(r; \chi) = \langle \Omega(\chi) | \phi(x) \phi(x+r) | \Omega(\chi) \rangle . \quad (6.2)$$

In this case, the limitation of entanglement has a clear consequence in the approximation of  $G_2(r)$  with  $G_2(r; \chi)$ . For an MPS, the two-point function  $G_2(r; \chi)$  necessarily decays asymptotically as an exponential, with the maximum correlation length of this decay  $\xi_\chi$  being set by the truncation parameter  $\chi$

$$G_2(r; \chi) \rightarrow e^{-r/\xi_\chi} \text{ as } r \rightarrow \infty . \quad (6.3)$$

Therefore, we can associate the finite entanglement effects for such MPS approximations with the infrared scale  $\xi_\chi$  which functions as an infrared cutoff like e.g. the finite lattice size  $N$ . For distances  $r \ll \xi_\chi$  we can expect that  $G_2(r; \chi)$  will approximate  $G_2(r)$  accurately. However, at longer distances the behaviour of  $G_2(r; \chi)$  will be modified significantly and to reproduce the two-point function at this scale higher  $\chi$  will be needed. Since the typical physical length scale in problems of interest is the correlation length  $\xi$ , we will want to reproduce  $G_2(r)$  with  $G_2(r; \chi)$  up to the scale  $r \sim \xi$  i.e. we require the hierarchy  $\xi \ll \xi_\chi$ .

When MPS are applied to the Hamiltonian lattice regularisation for the  $\phi^4$  theory, there will then be a number of different cutoffs to account for. Firstly, there are the UV cutoffs given by the lattice spacing  $a$  and boson number truncation  $d$ . Additionally, there is the entanglement cutoff  $\chi$ , which we can associate to an IR cutoff parametrised by  $\xi_\chi$ . Finally, for finite size systems there is the IR cutoff  $L$ . Depending on the observable in question, the effects of these cutoffs will be more or less relevant. Assuming that  $d$  and  $L$  are set sufficiently high we can expect that when  $\xi \ll \xi_\chi$  the physics of interest will be well reproduced by the use of MPS. Combined with the lattice spacing, this means that we will be interested in having the hierarchy of scales  $a \ll \xi \ll \xi_\chi$ , where both discretisation effects and finite entanglement effects should be small. Of course, this also requires  $\xi_\chi \ll L$  and the strict continuum limit  $\xi \rightarrow \infty$  will require that the entanglement effects be removed via  $\chi \rightarrow \infty$  along with any other IR cutoff e.g.  $L \rightarrow \infty$ .

In this chapter, we provide an outline of some of the approximation methods

for the ground-state and one-kink state that will be applied in Chapters 7 and 9, focussing on the “variational” algorithms that are specialised to tensor networks. We will also make use of more standard methods in Chapter 7, in particular the conjugate gradient method for uMPS, and details for this can be found in [1, 78]. Details for the finite-size variational-matrix-product-state (vMPS) algorithms discussed in Section 6.3 can be found in [68, 79, 80] while the variational-uniform-matrix-product-state (vuMPS) algorithm discussed in Section 6.4 is described in [81]. In Chapters 7 and 9 we also make use of algorithms to approximate the scalar mass using uMPS which we do not discuss in this Chapter and details can be found in [72].

## 6.2 Matrix Product States as a Variational Ansatz

To approximate observables using MPS, it is typical to find an approximation to the state of interest by solving an associated minimisation/optimisation problem restricted to the subset of states described by an MPS representation. For example, the energy minimisation problems that define the ground-state (4.11) and one-kink state (4.12) can also be used to define MPS approximations as :

$$|\Omega(\chi)\rangle = \arg \min_{|\psi\rangle \in \text{MPS}(\chi)} \left( \langle \psi | \tilde{H} | \psi \rangle - \lambda [\langle \psi | \psi \rangle - 1] \right) \quad (6.4)$$

for the ground state and

$$|K(\chi)\rangle = \arg \min_{|\psi\rangle \in \text{MPS}(\chi)} \left( \langle \psi | \tilde{H}_{(TPBC)} | \psi \rangle - \lambda [\langle \psi | \psi \rangle - 1] \right) \quad (6.5)$$

for the one-kink state, where  $\text{MPS}(\chi)$  denotes the set of MPS with bond-dimension  $\chi$  and other truncation parameters are not included explicitly for notational convenience. Approximations to equal-time observables can then be constructed as  $O(\chi) = \langle \Omega(\chi) | \hat{O} | \Omega(\chi) \rangle$  or  $O(\chi) = \langle K(\chi) | \hat{O} | K(\chi) \rangle$  and the corresponding one-dimensional tensor network can be contracted numerically-exactly. For instance, the equal-time  $n$ -point functions

$$G_n(x_1, x_2, \dots, x_n; \chi) = \langle \Omega(\chi) | \phi(x_1) \phi(x_2) \dots \phi(x_n) | \Omega(\chi) \rangle, \quad (6.6)$$

$$G_n^{(K)}(x_1, x_2, \dots, x_n; \chi) = \langle K(\chi) | \phi(x_1) \phi(x_2) \dots \phi(x_n) | K(\chi) \rangle, \quad (6.7)$$

provide approximations to the true  $n$ -point functions and can be calculated easily for MPS. The ground-state energy for finite size systems,

$$E_{\Omega}(\chi) = \langle \Omega(\chi) | \tilde{H} | \Omega(\chi) \rangle , \quad (6.8)$$

can be calculated using the MPO representation of  $\tilde{H}$ . Similarly, the kink mass can be approximated using the MPO representation of  $\tilde{H}_{(TPBC)}$  as

$$M_K(\chi) = \langle K(\chi) | \tilde{H}_{(TPBC)} | K(\chi) \rangle - E_{\Omega}(\chi) . \quad (6.9)$$

Note that, while this approximation coincides with that typically used in lattice QFT [48], one can also use the PBC Hamiltonian  $\tilde{H}_{(PBC)}$  instead of  $\tilde{H}_{(TPBC)}$  to estimate the kink energy, with the two estimates differing only by a boundary term that is irrelevant as  $N \rightarrow \infty$ . Of course, such variational estimates require the solution of the minimisation problems (6.4) and (6.5) which in general requires additional approximations.

### 6.3 Energy Minimisation Algorithm for MPS: vMPS

Standard optimisation strategies such as conjugate gradient have been applied successfully to the minimisation problems with MPS, see e.g. [82]. However, tensor networks are also associated to a more specific set of minimisation algorithms that take advantage of their natural structure. In the case of MPS, variational matrix product state energy minimisation (vMPS) is now a standard procedure for approximating ground states with MPS and has been highly successful in a variety of cases, see [68] for a detailed guide to implementation. The tensor network structure of the MPS provides a natural way to proceed with minimisation: rather than treat all degrees of freedom at once, one can instead minimise the energy with respect to just a single tensor (i.e. at a single site) while keeping all other tensors fixed. One then proceeds tensor by tensor minimising the energy iteratively. This is most efficiently performed in a sweeping pattern moving from site to site in a given direction until some convergence criteria are met.

To minimise the energy while changing only a tensor at a particular site, one must solve a generalised eigenvalue problem. To see this, consider the OBC tensor network representation of the energy expectation value with  $\tilde{H}$  in MPO form and

$N = 5$

$$\langle \psi | \tilde{H} | \psi \rangle = \begin{array}{c} \circ - \circ - \circ - \circ - \circ \\ | \quad | \quad | \quad | \quad | \\ \square - \square - \square - \square - \square \\ | \quad | \quad | \quad | \quad | \\ \circ - \circ - \circ - \circ - \circ \end{array} . \quad (6.10)$$

If we are only interested in varying a single tensor at a particular site, e.g. the site  $x = 3$ , all other tensors can be contracted together, giving

$$\langle \psi | \tilde{H} | \psi \rangle = \begin{array}{c} \circ \\ | \\ \square - \square - \square \\ | \\ \circ \end{array} . \quad (6.11)$$

for OBC, while in PBC the boundary tensors would include additional indices to be traced over. This expression can then be thought of as the action of an effective Hamiltonian on the tensor at the uncontracted site. In terms of the tensor network, the effective Hamiltonian then takes the form

$$H_{\text{eff}} = \begin{array}{c} \circ \\ | \\ \square - \square - \square \\ | \\ \circ \end{array} , \quad (6.12)$$

which is a linear operator on the space of rank-3 tensors. As such, it can be considered a matrix of size  $(d\chi^2, d\chi^2)$  that acts on vectors of size  $(d\chi^2)$  (i.e. the rank-3 tensors). In a similar way, an effective normalisation matrix can be constructed by replacing the MPO representing the Hamiltonian by the identity operator via  $\langle \psi | \psi \rangle = \langle \psi | \mathbf{1} | \psi \rangle$  where  $\mathbf{1} = \mathbf{1}_1 \otimes \mathbf{1}_2 \otimes \dots \otimes \mathbf{1}_N$ . To emphasise this structure, we can use the notation  $v_M = \mathbf{M}_{\alpha_x, \alpha_{x+1}}^{n_x}$  and write the two effective operators as matrices on this space,  $\mathbf{H}_{\text{eff}}$  and  $\mathbf{N}_{\text{eff}}$ . In this notation the (ground state) minimisation problem at this site can be written as

$$\tilde{v}_M = \arg \min_{v_M \in \mathbb{C}^{d\chi^2}} \left( v_M^\dagger \mathbf{H}_{\text{eff}} v_M - \lambda \left[ v_M^\dagger \mathbf{N}_{\text{eff}} v_M - 1 \right] \right) , \quad (6.13)$$

which can be solved by finding the minimum eigenvector of the generalised eigenvalue problem

$$\mathbf{H}_{\text{eff}} v_M = \lambda \mathbf{N}_{\text{eff}} v_M . \quad (6.14)$$

To find an approximation to the ground state one then initiates a (random) MPS, chooses a site  $i$ , forms the effective operators  $\mathbf{H}_{\text{eff}}$ ,  $\mathbf{N}_{\text{eff}}$ , finds the minimum eigenvector  $\tilde{v}_M$  of the generalised eigenvalue problem Equation (6.14) and updates the

current MPS by replacing the rank-3 tensor at the site  $i$  with the rank-3 tensor corresponding to the minimum eigenvector  $\tilde{v}_M$ . The updated MPS will have a lower energy and so by proceeding to the next site the energy can be lowered iteratively until convergence is achieved. This constitutes the general idea of the vMPS procedure.

To improve the stability and efficiency of the vMPS procedure, the gauge freedom in the MPS definition can be exploited. With OBC MPS, when optimising the site  $i$ , if the mixed gauge is chosen then expectation values of local observables depend only on the tensor at that site as in Equation (5.56). This is particularly important since the norm is then simply given by

$$\langle \psi | \mathbf{1} | \psi \rangle = (\mathbf{1} | E_{M_k}^{M_k} | \mathbf{1} ) , \quad (6.15)$$

which means the effective normalisation matrix is trivial  $\mathbf{N}_{\text{eff}} = \mathbf{1}$ . This reduces the generalised eigenvalue problem (6.14) to an ordinary eigenvalue problem which is considerably more stable and can be solved very efficiently. Unfortunately, for PBC, this gauge cannot be chosen and other stabilisation strategies must be found, e.g. see [79, 80].

## 6.4 Energy Minimisation Algorithm for uMPS: vuMPS

A variational algorithm can also be found in the case of infinite-size uMPS, see [81] for details. In this case, OBC can be used and the mixed gauge can be chosen to improve stability and performance without the associated boundary effects. Of course, in the infinite size case, the ground-state energy is infrared divergent. This can be seen by calculating the energy expectation value of a uMPS  $|\psi[A]\rangle$ , assumed to provide an approximation to the ground-state, in the left or right gauge. A convenient parametrisation for the nearest-neighbour Hamiltonian in the infinite-size case is as a sum over product operators

$$\tilde{H} = \sum_x \sum_s \mathcal{H}_x^{(s)} \otimes \mathcal{H}_{x+1}^{(s)} + \sum_x \epsilon \mathbf{1}_x \otimes \mathbf{1}_{x+1} , \quad (6.16)$$

where the constant  $\epsilon$  is chosen to regulate the infrared divergence. In the left gauge, the approximation to the ground-state energy expectation value is then

$$\begin{aligned} \langle \psi[A] | \tilde{H} | \psi[A] \rangle &= \epsilon |\mathbf{Z}| + \sum_{x=-\infty}^{\infty} \sum_s (\mathbb{1} | T_L[\mathcal{H}_1^{(s)}] T_L[\mathcal{H}_2^{(s)}] | R) \\ &= \epsilon |\mathbf{Z}| + |\mathbf{Z}| \sum_s (\mathbb{1} | T_L[\mathcal{H}_1^{(s)}] T_L[\mathcal{H}_2^{(s)}] | R) \end{aligned} \quad (6.17)$$

$$= \epsilon |\mathbf{Z}| + \epsilon_0 |\mathbf{Z}|, \quad (6.18)$$

where  $|\mathbf{Z}|$  indicates the divergent contribution coming from the sum over all sites. The choice  $\epsilon = -\epsilon_0$ , i.e. subtracting the current best estimate of the ground-state energy density, then regulates the infrared divergence as expected.

The effective Hamiltonian representing the variation of the energy expectation value with  $A_C$  is then constructed by finding the explicit dependence of  $\langle \tilde{H} \rangle$  on  $A_C$  and removing the tensor  $A_C$  from the corresponding network, as in the finite-size MPS case. In the mixed gauge form, the energy expectation value can be written as

$$\begin{aligned} \langle \psi[A] | \tilde{H} | \psi[A] \rangle &= \sum_x \sum_s \langle \psi[A] | \mathcal{H}_x^{(s)} \mathcal{H}_{x+1}^{(s)} | \psi[A] \rangle - \epsilon_0 \sum_x \langle \psi[A] | \psi[A] \rangle \\ &= (H_L | E_{A_C}^{A_C} | \mathbb{1}) + (\mathbb{1} | E_{A_C}^{A_C} | H_R) - |\mathbf{Z}| \epsilon_0 (\mathbb{1} | E_{A_C}^{A_C} | \mathbb{1}) + \\ &\quad + \sum_s \left[ (\mathbb{1} | E_{A_C}^{A_C} [\mathcal{H}_1^{(s)}] T_R[\mathcal{H}_2^{(s)}] | \mathbb{1}) + (\mathbb{1} | T_L[\mathcal{H}_1^{(s)}] E_{A_C}^{A_C} [\mathcal{H}_2^{(s)}] | \mathbb{1}) \right], \end{aligned} \quad (6.19)$$

where  $(H_L |$  and  $|H_R)$  contain infinite sums over products of the transfer matrices

$$(H_L | = \sum_s \left[ (\mathbb{1} | T_L[\mathcal{H}_1^{(s)}] T_L[\mathcal{H}_2^{(s)}] \left( \sum_{k=0}^{\infty} (T_L)^k \right) \right], \quad (6.20)$$

$$|H_R) = \sum_s \left[ \left( \sum_{k=0}^{\infty} (T_R)^k \right) T_R[\mathcal{H}_1^{(s)}] T_R[\mathcal{H}_2^{(s)}] | \mathbb{1} \right]. \quad (6.21)$$

The infrared divergences are now encoded in the infinite sums over products of  $T_L$  and  $T_R$  which are divergent since they have dominant eigenvalue equal to one. This divergence can be extracted by decomposing the transfer matrix into a sum of its dominant eigenspace projector and complementary part, e.g.,  $T_L = |R)(\mathbb{1} | + \tilde{T}_L$ .

Then

$$\begin{aligned} \sum_{k=0}^{\infty} [T_L]^k &= \sum_{k=0}^{\infty} [\tilde{T}_L]^k + \sum_{k=0}^{\infty} [|R](\mathbb{1}]^k \\ &= \sum_{k=0}^{\infty} [\tilde{T}_L]^k + \frac{1}{2} |\mathbb{Z}| |R](\mathbb{1}] , \end{aligned} \quad (6.22)$$

and similarly for the sum involving  $T_R$ , see [72] for more details. The first sum in (6.22) is now convergent and can be summed as a standard geometric series. When inserted back into the expression (6.21), the second divergent term just provides a constant contribution equal to half the energy

$$\begin{aligned} \langle H_L | &= \sum_s (\mathbb{1} | T_L [\mathcal{H}_1^{(s)}] T_L [\mathcal{H}_2^{(s)}] \left[ \sum_{k=0}^{\infty} (\tilde{T}_L)^k \right] + \frac{1}{2} |\mathbb{Z}| \sum_s (\mathbb{1} | T_L [\mathcal{H}_1^{(s)}] T_L [\mathcal{H}_2^{(s)}] | R](\mathbb{1} | \\ &= \sum_s (\mathbb{1} | T_L [\mathcal{H}_1^{(s)}] T_L [\mathcal{H}_2^{(s)}] \left[ \sum_{k=0}^{\infty} (\tilde{T}_L)^k \right] + \frac{1}{2} |\mathbb{Z}| \epsilon_0 (\mathbb{1} | . \end{aligned} \quad (6.23)$$

The divergent piece is then cancelled in the expression (6.19) by the term proportional to  $\epsilon$  as desired.

With  $\langle \tilde{H} \rangle$  regulated and written with the dependence of  $A_C$  made explicit, the effective Hamiltonian can be derived from (6.19) by removing the tensor  $A_C$ . The vMPS algorithm then proceeds similarly to vMPS with the corresponding eigenvalue problem being solved to update  $A_C$  and iteratively minimise the energy. While the above discussion captures the spirit of the algorithm, there are in fact more subtleties since the whole state must be updated in a way that preserves translational invariance, for details see [81].

## 6.5 Low Entanglement Approximations for the $\phi^4$ Theory

Within the Hamiltonian lattice regularised setting, matrix product states can be applied to the  $\phi^4$  scalar field theory in  $D = (1 + 1)$  allowing the equilibrium physics of the theory to be studied efficiently, see e.g. [1]. The ground-state can be approximated in the infinite-size limit by uMPS using minimisation algorithms such as the conjugate gradient method or vuMPS. With the approximation of the ground-state obtained observables such as the ground-state equal-time  $n$ -point functions and

energy (density) can be studied. The scalar mass can also be approximated from the equal-time two-point function or by direct approximation of the one-particle excited state.

When the correlation length of the ground-state is small, only small bond-dimensions  $\chi$  should be required to approximate the observables of interest. Therefore, deep in the symmetric or symmetry broken phases when the correlation length becomes small, we can expect that only small  $\chi$  will be required to approximate observables, consistent with the fact that semi-classical methods/mean-field theory is applicable in these regions. Near the critical point, when the correlation length is very large, we can expect high values of  $\chi$  to be needed and ultimately at the critical point other methods will be required. By contrast, we can expect that the maximum required local boson occupation number  $d$  will grow as one heads into the symmetry broken phase and the field expectation values become large.

The one-kink state and associated observables can be studied using a finite-size MPS along with the vMPS minimisation algorithm. While this method can be applied equally to the one-kink state and the finite-size ground-state, in the former case we can expect more difficulties. In particular, the finite-size matrix product state techniques described here are naturally inhomogeneous and during the minimisation procedure translational invariance will be broken numerically leading to spatial dependence of the tensors  $\mathbf{M}_x^{n_x}$ . As such, the true translational invariance of observables is only approximated. In the case of the ground state, this is no problem since the MPO representation of the lattice Hamiltonian is reasonably homogeneous and translational invariance can be easily approximated with a low  $\chi$  MPS. However, for the one kink state, the Hamiltonian appears quite inhomogeneous with a particular location being selected for the twist. This makes it much harder to approximate translational invariance and the kink must be “delocalised” by using a sufficiently high  $\chi$ .

In practice, the approximation of translational invariance tends to happen quickly so that one can think of a threshold  $\tilde{\chi}(d, N)$  after which the spatial variance of local observables drops dramatically. The value of  $\tilde{\chi}(d, N)$  will depend on the observable in question as well as the values of  $d$  and  $N$  with higher  $d$  and larger  $N$  leading to an increased  $\tilde{\chi}(d, N)$ . The dependence on  $d$  is particularly important since it means that in regions of parameter space requiring high  $d$  it will become impossible to approximate translational invariance for the kink state with this method. Therefore, it is the semi-classical region  $\tilde{\mu}_0^2 \gg \tilde{\lambda}_0$  that will be hard to approximate in this sense, while the strong coupling region will be less problematic. Of course, as with the ground-state, this is not too much of an issue since the semi-classical

region can be treated perturbatively. Furthermore, observables that include contributions from the entire lattice, e.g. the kink mass, do not depend strongly on the translational invariance of the state. We note that, if desired, the kink mass can also be approximated in a similar manner to the scalar mass using specific ansatz for the kink excitations which can include translational invariance explicitly, see [83] for details.

# Chapter 7

## Studying the Kink in Equilibrium with MPS

### 7.1 Introduction

In this chapter, following the work by the author published in [84], we turn to the study of the ground-state and one-kink state using matrix product states. From a physics perspective, the approximation of ground-state and one-kink state observables is desirable in its own right, particularly when done in a manner that can generalised to other theories and defects. Additionally, such equilibrium quantities are required for the confirmation of topological defect formation via the KZM, and so are also helpful in the non-equilibrium case. From a more technical point of view, the study of equilibrium physics provides an opportunity to understand the effect of the various truncations on approximations, in addition to confirming that the method used can capture the physics of kink defects at all.

We study the  $\phi^4$  QFT in the lattice Hamiltonian setting as described in Chapter 4. An approximation to the ground-state is obtained by using uMPS and conjugate gradient energy minimisation applied to the lattice Hamiltonian (4.2). We will work in lattice units throughout and so drop the tildes for notational convenience. The one-kink state is approximated using PBC MPS and the vMPS algorithm, see Section 6.3, applied to the lattice Hamiltonian with TPBC (4.10). When using the vMPS algorithm to approximate the one-kink state, a strategy must be chosen to stabilise the vMPS algorithm. In this chapter, we have followed the method outlined in [79]. Unfortunately, in the case of TPBC this was not sufficient to be able to solve the generalised eigenvalue problem with sparse methods and we have used dense methods at a cost of  $\mathcal{O}(\chi^6)$ . Despite the relative expense, we find that

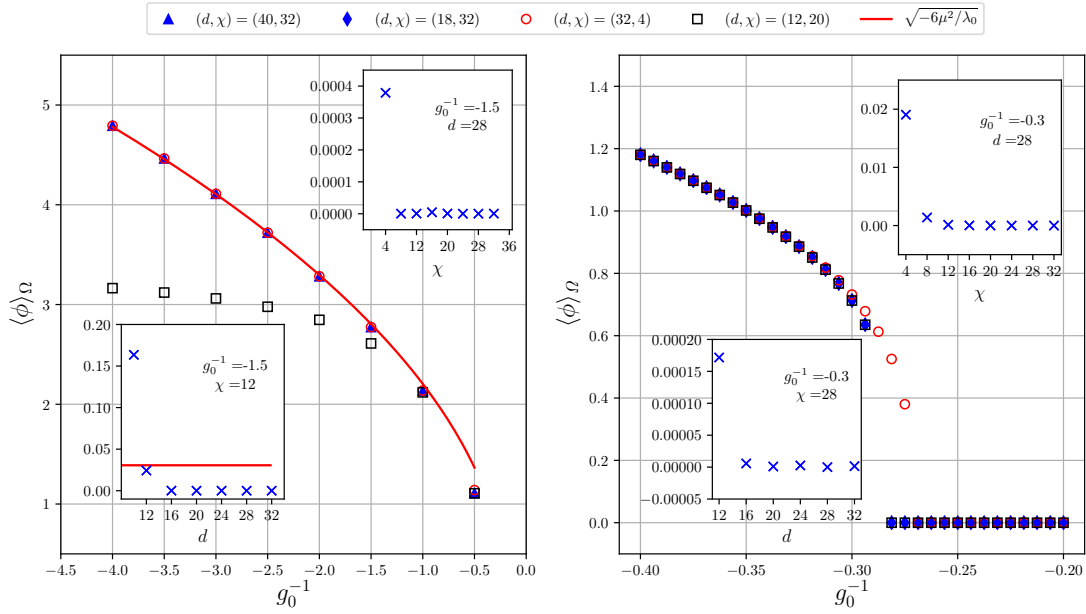


Figure 7.1: The field expectation value for various effective couplings using a uMPS approximation to the ground state. In the left-hand plot, weak-couplings are displayed with  $\lambda_0 = 0.1$  and  $(d, \chi) = (40, 32)$  (blue triangles). These can be compared to low  $\chi = 4$  approximations (hollow red circles) which look almost identical on this scale. This contrasts the low  $d = 12$  approximations (hollow black squares) for which the expectation value appears truncated agreeing with the higher  $d$  approximations only when the field expectation value is relatively low. The insets show the convergence for the selected inverse coupling  $g_0^{-1} = -1.5$  (the best estimate has been subtracted so that the plots tend to zero) and the difference in scales between the two indicate that  $d$  is the relevant parameter to achieve a good approximation in the weak coupling regime. The semi-classical result is also shown in the main figure and lower-left inset (solid red line) with  $v = \sqrt{-6\mu^2/\lambda_0}$  where  $\mu^2 = \mu_0^2 - m_C^2$  and  $m_C^2 = -0.019$  is determined by fitting to the data. The stronger coupling data (right-hand plot) with  $(d, \chi) = (18, 32)$  and  $\lambda_0 = 2$  (blue diamonds) shows the usual symmetry breaking pattern. Here, the relevant parameter to achieve a good approximation is  $\chi$  as shown by the scale difference between the insets and also by the fact that the low  $d$  approximation agrees well with the data on the main plot while the low  $\chi$  data fails to agree near the critical point.

the reachable  $\chi \approx 20$  are sufficient for studying the kink mass at strong couplings though for studying other observables e.g. the two-point function in the presence of the kink, higher  $\chi$  would be needed and an alternative stabilisation strategy would be useful such as the one in [80] which was applied to a spin system with TPBC. To fix the value of  $d$  in the TPBC case, we start with a low  $\chi$  and increase  $d$  until convergence is reached in the observable in question. The final value of  $d$  is then used when performing the higher  $\chi$  calculations.

We study both weak and strong coupling behaviour by fixing the value of  $\lambda_0 = 0.1$  or  $2$  while using a range of  $\mu_0^2$ . When the effective coupling is small we compare the MPS approximation to the analytic results from the classical continuum, see Section 2.2. This comparison can be made in the continuum region where  $\xi \gg 1$  with the lowest order mass renormalisation included numerically by fitting the classical forms to the MPS data, replacing the bare mass with  $\mu^2 = \mu_0^2 - m_C^2$  where  $m_C^2$  is treated as a free parameter. In the strong coupling region, the TN approximations can be compared with universal results and we will focus on a comparison of the mass ratio  $m_S/M_K$  to the universal result  $m_S/M_K \approx 2$  corresponding to the universal amplitude ratio (2.33). In both the strong-coupling and weak-coupling cases, we assess the effects of the truncation parameters  $d$  and  $\chi$  to check that the approximation of observables behave as expected.

## 7.2 Field Expectation Values, Basis Truncation and Finite Entanglement Effects

In order to accurately approximate an observable with the lattice theory and MPS, both the local basis truncation parameter  $d$  and the entanglement cutoff (bond-dimension)  $\chi$  must be sufficiently high. Depending on the observable in question, the effect of the cutoffs, controlled by the  $d$  and  $\chi$ , will be more or less important. As discussed in Section 4.4.2, the boson occupation number truncation via  $d$  can be understood somewhat simply in the full lattice theory (i.e. when  $\chi \rightarrow \infty$ ) in terms of its effect on the approximation of local quantities such as  $\langle \phi^2 \rangle$ . This should also be the case when using MPS for local observables e.g.  $\langle \Omega | \phi^2 | \Omega \rangle$  since the approximation of local quantities should require relatively small values of  $\chi$  that will be reachable with the algorithms used here. Depending on the effective coupling, the value of  $\chi$  required will change somewhat from a smaller value for weak couplings (where mean-field theory is accuracy and quantum corrections are small) to larger values when the effective coupling is strong. Conversely, as the expectation value of  $\langle \Omega | \phi | \Omega \rangle$  increases into the symmetry broken phase, the value of  $d$  required will increase.

This effects of finite  $d$  and  $\chi$  are illustrated in Figure 7.1 where the uMPS approximation of the vacuum expectation value  $\langle \Omega | \phi | \Omega \rangle$  is shown for perturbative and non-perturbative bare effective couplings  $g_0 = \lambda_0 / \mu_0^2$ . In the first case, the results (blue triangles) can be compared with the classical continuum result (red line)

$v = \sqrt{-6\mu^2/\lambda_0}$ . In the stronger coupling case, there is no analytic comparison but the expected symmetry breaking pattern can be seen. In principle, such plots can be used to determine the location of the critical point e.g. by using the critical exponent associated with the vanishing field expectation value. However, as discussed in [1], such fits are highly sensitive and it is much better to use observables with a simpler scaling, e.g. the kink mass, to determine the location of the critical point.

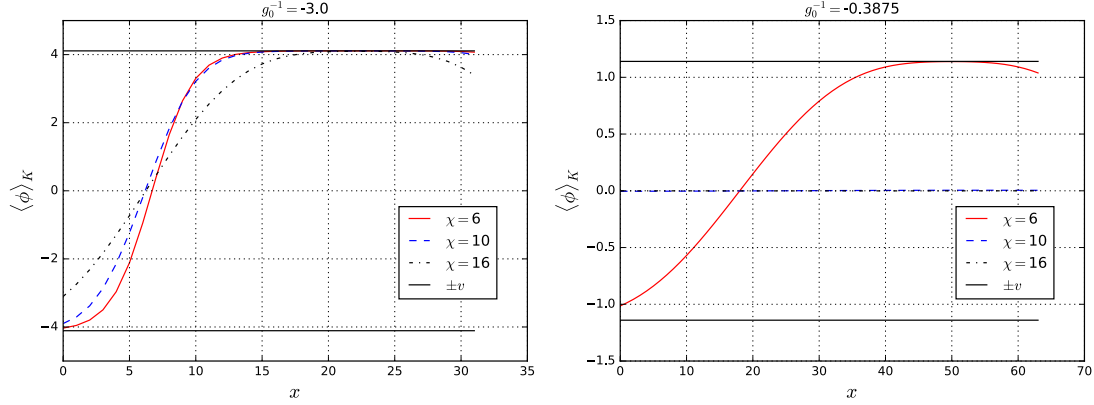


Figure 7.2: The field expectation value of the finite size lattice MPS approximation to the one kink state for weak coupling  $g_0 \approx -0.33$  (left-hand plot) and stronger coupling  $g_0 \approx -2.58$  (right-hand plot) with lattice sizes  $N = 32, 64$  and  $28 \leq d \leq 32, 14 \leq d \leq 18$  respectively. These can be compared with the corresponding field expectation values of a uMPS approximation to the ground state  $\pm v$  (solid black lines) with  $(d, \chi) = (40, 32)$  and  $(18, 32)$  for the weak coupling and stronger coupling respectively. For the low  $\chi = 6$  runs (solid red line) a classical kink-like profile is visible for both couplings which interpolates between  $\pm v$  such that the correct  $\langle \phi \rangle_K = 0$  is not found. Increasing  $\chi$  de-localises the kink and translational invariance can be approximated in the stronger coupling case such that  $\langle \phi \rangle_K \approx 0$ .

For observables other than the local ground state expectation values, there are additional factors that determine the accuracy of the approximations obtained by the MPS. Essentially, the important features are the observation distance and to what degree the observable represents an average over the system. In the first case, only the truncation parameter  $\chi$  is important and increasing  $\chi$  will allow longer distances to be better approximated. This can be seen clearly in ground state connected two-point function  $G_2(r)$  where larger  $\chi$  are required to approximate the observable at larger distances  $r$ . In the second case, one can think of a particular threshold  $\chi \approx \tilde{\chi}(d, N)$  being required before the translational invariance of observables is well approximated. This will depend strongly on the observable/state in question and on the truncation parameters  $d$  and  $N$ .

The issues surrounding the approximation of translational invariance can be

seen clearly when calculating the field expectation values  $\langle \Omega | \phi | \Omega \rangle$  and  $\langle K | \phi | K \rangle$ . Since both observables are local, they will converge quickly in  $\chi$  so long as the threshold  $\chi \approx \tilde{\chi}(d, N)$  is met. In the ground state case,  $\tilde{\chi}(d, N)$  is essentially negligible and the approximation of  $\langle \Omega | \phi | \Omega \rangle$  converges rapidly. However, in the one kink state  $\tilde{\chi}(d, N)$  is important and, for sufficiently large values of  $d$  or  $N$ , local expectation values such as  $\langle K | \phi | K \rangle$  will show significant spatial variations and cannot be accurately approximated. We note that, in the finite-size case, the field expectation value is in principle zero, respecting the  $\mathbb{Z}_2$  symmetry but is broken numerically during the approximation and must be enforced explicitly if desired [85].

The problematic behaviour of  $\langle K | \phi | K \rangle$  is shown in Figure 7.2. In the semi-classical case with bare effective coupling  $g_0 \approx -0.33$ , the high field expectation value requires a relatively high value of  $d$  to converge and the threshold  $\tilde{\chi}(d, L)$  is higher than the shown  $\chi = 6, 10, 16$ . This means that a classical-like kink profile can be seen and increasing  $\chi$  achieves only very slight changes to the width such that the correct  $\langle \phi \rangle_K = 0$  value is not obtained. Moreover, the zero-mode means that the point at which  $\langle \phi(x) \rangle_K$  crosses zero is independent of the energy making convergence in  $\chi$  or  $d$  difficult to quantify. However, at stronger couplings the field expectation value is much lower, corresponding to a lower  $d$ , which makes it easy to approximate translational invariance and obtain  $\langle \phi \rangle_K \approx 0$  even for the modest values of  $\chi$  shown.

Observables that average over the whole system can be much less sensitive to spatial variations in the MPS representation than observables evaluated at a particular point. For example, the behaviour of  $\langle K | \phi_x^2 | K \rangle = \langle \phi^2 \rangle_K$  displays similar spatial variations at weak coupling as for the case of  $\langle K | \phi_x | K \rangle$ , see Figure 7.3. However, the spatial average of this expectation value  $\langle \langle \phi^2 \rangle \rangle_K$  has a much weaker dependence on  $\chi$ . This is shown in Figure 7.4 where the spatial variation of the expectation values of both  $\langle \phi \rangle_K$  and  $\langle \langle \phi^2 \rangle \rangle_K$  are shown by error bars corresponding to their standard deviation with  $x$ . Despite the strong spatial variation in  $\langle \phi^2 \rangle_K$ , the spatial average changes only very weakly with  $\chi$  in both cases indicating that this observable can be well approximated even in the weak coupling case. This behaviour can be compared with that of  $\langle \phi \rangle_K$ : while the spatial average does not display much variation in the weak coupling case, since the operator is  $\mathbb{Z}_2$  anti-symmetric, it still gives the incorrect non-zero value and is only correctly approximated in the stronger coupling region where translational invariance is approximated. In general, observables corresponding to  $\mathbb{Z}_2$  anti-symmetric operators cannot be reliably approximated outside the translational invariant region, while the spatial average of those corresponding

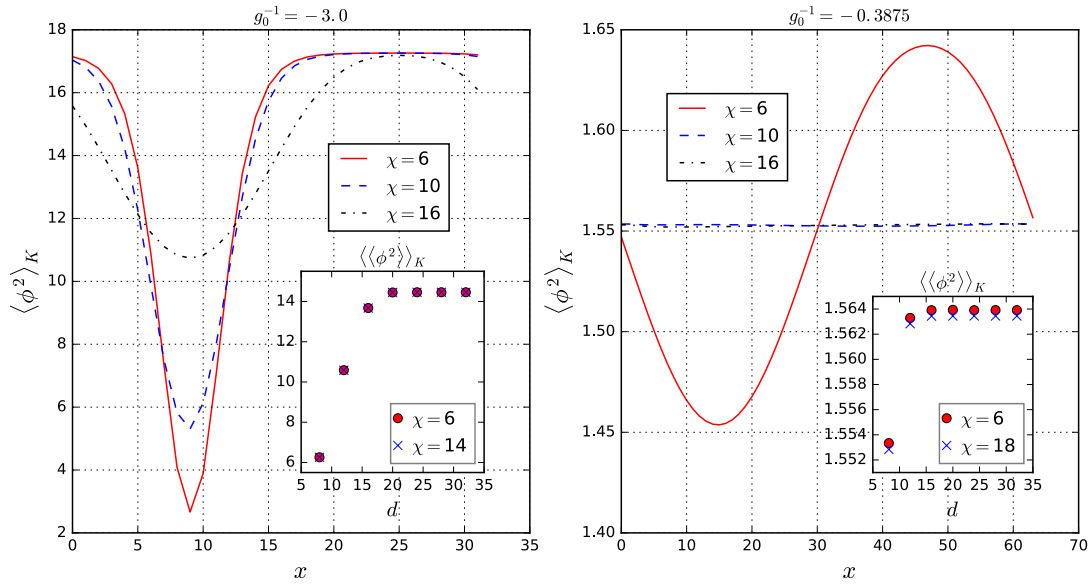


Figure 7.3: The  $\phi^2$  expectation value corresponding to the one kink approximations in Figure 7.2. As with  $\langle \phi \rangle_K$ , translational invariance can only be approximated in the stronger coupling case. Nevertheless, since the operator is  $\mathbb{Z}_2$  invariant, the spatial average is well behaved and its convergence can be studied as shown in the insets.

to  $\mathbb{Z}_2$  symmetric operators can be.

### 7.3 Particle Masses at Weak Coupling

An estimate of the scalar mass  $m_S$  can be extracted from the lattice regularised theory by the method outlined in Section 4.3.2. When using MPS, the finite bond-dimension will modify the long-distance behaviour of the observable  $G_2(r)$  ultimately leading to a pure exponential decay. The distance where this occurs is determined by the truncation parameter  $\chi$  and we denote the length scale associated to this as  $\xi_\chi$ . Recalling that an estimate of the scalar mass is obtained via a constant region of  $m_S(r)$  (4.20), we now expect this region to occur at some intermediate distance above the scale of higher mass contributions to  $G_2(r)$  and below the scale of finite entanglement corrections which artificially force the decay of  $G_2(r)$ .

The kink mass  $M_K$  is calculated from the difference of the one kink energy expectation value  $\langle K | \tilde{H}_{(TPBC)} | K \rangle$ , obtained from the finite size lattice MPS, and the ground state energy density, obtained from the uMPS. The latter converges quickly in  $\chi$  and the only potential issue is the approximation of  $\langle K | \tilde{H}_{(TPBC)} | K \rangle$ .

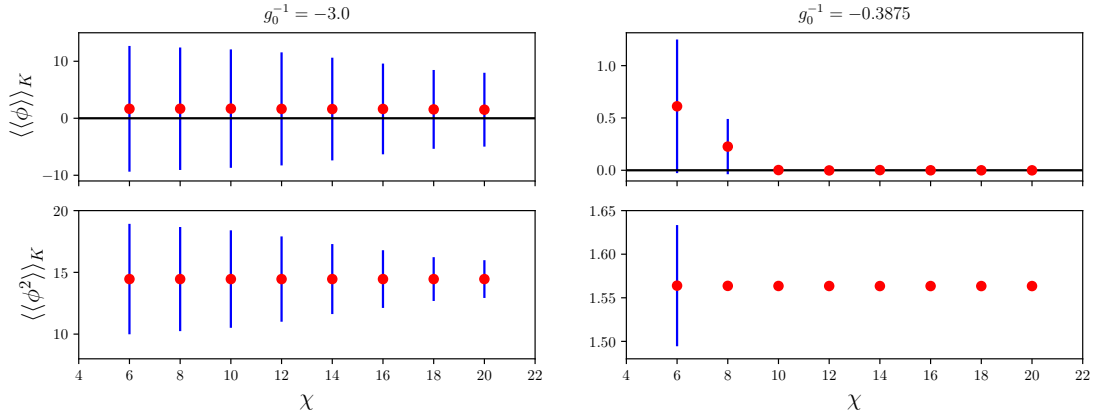


Figure 7.4: The spatial average (red dots) of the  $\phi$  and  $\phi^2$  expectation values for the finite size lattice MPS approximation to the one kink state at weak coupling  $g_0 \approx -0.33$  (left-hand plots) and stronger coupling  $g_0 \approx -2.58$  (right-hand plots) with the same parameters as in Figure 7.2. The spatial standard deviation of the expectation values, shown as error bars, changes strongly with  $\chi$  and becomes small only for strong couplings. However, the spatial averages changes only weakly and the value of  $\langle\langle\phi^2\rangle\rangle_K$  can be reliably approximated in both regions. Note that, due to its anti-symmetry, the value of  $\langle\langle\phi\rangle\rangle_K$  is only correct and approximately equal to zero (indicated by the black line) in the stronger coupling case.

However, since the kink mass includes contributions from the whole system, is fairly local and  $\mathbb{Z}_2$  symmetric, we can expect a reasonable convergence with  $\chi$  even in the weak coupling case. In the case of the scalar mass, since it is estimated from the ground state observable  $G_2(r)$ , approximating translational invariance should not be an issue and we can focus on the need to increase  $\chi$  so that the region up to  $r \approx \xi$  is well approximated. At weak couplings,  $\xi$  is relatively small so that the required  $\chi$  should not be too high allowing for an estimate of  $m_S$  to be extracted relatively easily. The kink mass and scalar mass are shown for a variety of weak couplings in Figure 7.5 along with the classical continuum results for comparison.

## 7.4 Strong Coupling: Universal Amplitude Ratio and Particle Masses

At stronger couplings the correlation length  $\xi$  increases so that to estimate  $m_S$  longer distances of  $G_2(r)$  need to be approximated requiring larger  $\chi$ . Ultimately, this means that this method cannot be used with MPS arbitrarily close to the critical point where the scalar mass vanishes. This is reflected in the fact that at

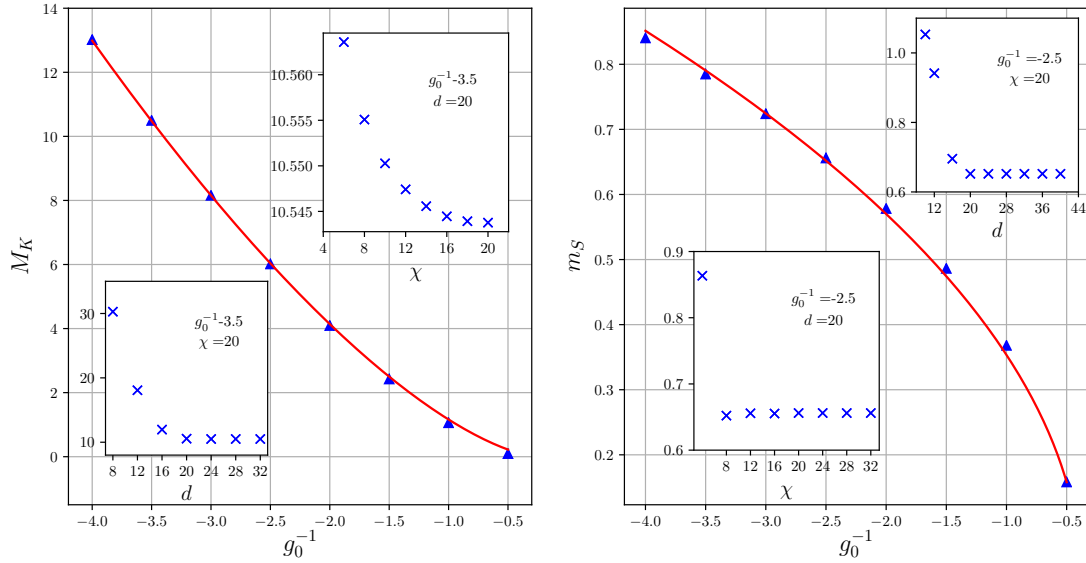


Figure 7.5: The kink mass  $M_K$  (left-hand plot) and scalar mass  $m_S$  (right-hand plot) for various weak couplings (data in blue triangles). The kink mass is calculated from the energy expectation value of the finite size lattice MPS approximation of the one kink state with  $\chi = 14$  and the approximation of the ground state energy density obtained from a uMPS approximation with  $\chi = 32$ . The scalar mass is extracted from the uMPS approximation to the ground state connected equal time two-point function  $G_2(r)$  via a Bessel function ansatz (4.19). Both are compared with the semi-classical continuum results (solid red lines)  $M_K = 4\sqrt{2}\mu^3/\lambda_0$  and  $m_S = \sqrt{2}\mu$  where  $\mu^2 = \mu_0^2 - m_C^2$  and  $m_C^2$  is determined by fitting to the data to give  $-0.025, -0.037$  respectively. The convergence of the approximations with  $d$  and  $\chi$  is shown in the insets.

the critical point the correlation length diverges leading to algebraically decaying correlations which correspond to a logarithmic violation of the entanglement area law i.e.  $S_A \sim \log(V_A)\partial\mathcal{A}$ . While an MPS can still be used to approximate short distance observables in the critical region [86] an alternative tensor network, e.g. the *multi-scale entanglement renormalisation ansatz* (MERA) [87], that obeys the correct low entanglement law will also allow the approximation of the long range physics. Of course, this means that MPS are not especially suited to the study of universal physics and we can expect difficulty when trying to reproduce the strong coupling behaviour e.g. the universal mass ratio.

The scalar mass at strong couplings is plotted along with the kink mass in Figure 7.6. As discussed in Section 2.3, at strong couplings in the broken symmetry phase, the universal amplitude ratio relates the kink and scalar mass as  $2M_K = m_S$  and a qualitative change in the scaling can be seen in the left-hand plot of Figure 7.6 at the point when  $2M_K \approx m_S$  as expected. However, the estimate of  $m_S$  with

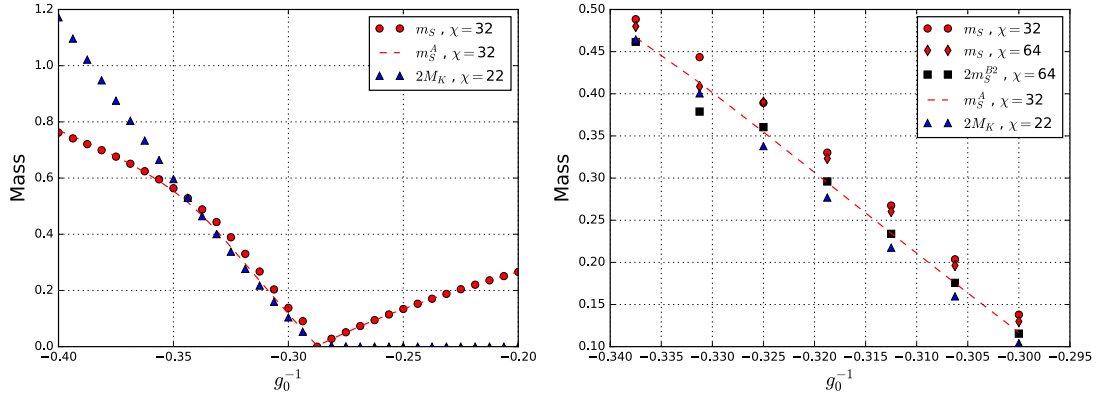


Figure 7.6: Estimate of the scalar mass  $m_S$  extracted from the uMPS approximation to the ground state connected equal time two-point function  $G_2(r)$  via a Bessel function ansatz (4.19) ( $\chi = 32$  red dots,  $\chi = 64$  red diamonds). This can be compared with the estimate extracted from the excitation ansatz  $m_S^A$  (dashed red line) and twice the kink mass  $2M_K$  (blue triangles) calculated from the  $N = 64$  finite size lattice MPS approximation to the one kink state. The left-hand plot shows a larger range of bare coupling  $2.5 \lesssim g_0 \lesssim 5$  while the right-hand plot focuses on the strong coupling region with  $2.95 \lesssim g_0 \lesssim 3.39$ . A qualitative change can be seen when entering the strong coupling region at  $m_S \approx 2M_K$  but the  $\chi = 32$  Bessel ansatz (4.19) does not provide a good quantitative agreement with the expected behaviour  $m_S \approx 2M_K$  in the strong coupling region. The higher  $\chi = 64$  Bessel ansatz does improve the estimate but the  $\chi = 64$  Bessel-squared ansatz (4.21) (black squares, only in right-hand plot) improves the estimate further in agreement with the  $\chi = 32$  excitation ansatz estimate (dashed red line). As mentioned in Section 4.3.2, the scalar mass is estimated from averaging over a “uniform” region of  $m_S(r)$  chosen here by a single tolerance for all values of  $g_0^{-1}$ . While this has the advantage of being “blind” using a single tolerance can lead to somewhat anomalous points (e.g. see the point at  $g_0^{-1} \approx -0.331$ ) and instead one can choose the tolerance adaptively for each  $g_0^{-1}$  which eliminates such points, improving the estimates of  $m_S$ .

$\chi = 32$  in the critical region extracted from the Bessel function tends to be somewhat higher than the value of  $2M_K$  suggesting that, as might be expected, it is inaccurate in this region. The scalar mass extracted from the excitation ansatz described in [72] with  $\chi = 32$  is also plotted for comparison (red dashed line) and is somewhat closer to the value of  $2M_K$  suggesting that it can provide a more efficient and accurate method to extract the scalar mass in the critical region. To increase the accuracy of the uMPS method one can simply increase the value of  $\chi$  but it is also possible to use the Bessel-squared ansatz Equation (4.21). A comparison of these methods is shown for the strong coupling region in the right-hand plot. The estimate of the scalar mass is closer to the expected behaviour when  $\chi$  is increased (red dots and diamonds) but the use of the Bessel-squared ansatz improves the estimate again (black squares)

agreeing fairly well with the excitation ansatz. The significant improvement of the Bessel-squared method over the single Bessel method suggests that the uMPS is able to capture the contributions coming from the kink-antikink excitations in this observable.

## 7.5 Conclusion

In this chapter, we have seen that TN can be used to successfully approximate the equilibrium observables of the kink defect in the  $\phi^4$  theory. The generality of the TPBC method used means that other defects could also be approximated in this way, assuming an appropriate choice of tensor network is made. We have also shown how the scalar mass can be extracted from the ground-state two-point functions, once again in a general way that can be applied easily to other theories, and discussed various practical issues with using TNs for the study of QFT.

To achieve higher accuracies than obtained here, larger  $\chi$  can be used by following more recently developed algorithms than the conjugate gradient minimisation used here, such as the vuMPS algorithm [72]. Alternatively, one can also turn to better suited tensor networks such as MERA and both the methods to obtain the kink mass and scalar mass should be readily adaptable to this case.

# Chapter 8

## Time Evolution with Tensor Networks

### 8.1 Introduction

In non-equilibrium quantum field theory, one is typically interested in calculating  $n$ -point functions of field operators in situations where the state is far from an equilibrium state. Typical scenarios of study are evolution from some chosen non-equilibrium initial condition or the inclusion of explicit time-dependence in the Hamiltonian. When non-equilibrium dynamics are expressed in the Heisenberg picture, equations of motion for the field operators can be derived that determine the generally infinite hierarchy of equations required to specify the dynamics of observables such as the  $n$ -point functions. For example, the equation of motions for the field operators of the  $\phi^4$  theory in the Hamiltonian lattice regularisation (4.2) are

$$\begin{aligned}\dot{\phi}_x &= \tilde{\pi}_x , \\ \dot{\tilde{\pi}}_x &= (\phi_{x+1} - 2\phi_x + \phi_{x-1}) - \tilde{\mu}_0^2 \phi_x - \frac{\tilde{\lambda}_0}{3!} \phi_x^3 .\end{aligned}\tag{8.1}$$

These can be combined to give the equations of motion in the desired  $n$ -point functions which depend on all others, unless they are zero by some symmetry. For example, the two-point function  $G_2(x, y) = \langle \phi_x \phi_y \rangle$  is linked to the four-point func-

tion  $G_4(x, y, z, w) = \langle \phi_x \phi_y \phi_z \phi_w \rangle$  by

$$\begin{aligned} \frac{d}{dt} G_2(x, y) &= \langle \dot{\phi}_x \phi_y \rangle + \langle \phi_x \dot{\phi}_y \rangle \\ &= \langle \tilde{\pi}_x \phi_y \rangle + \langle \phi_x \tilde{\pi}_y \rangle , \end{aligned} \quad (8.2)$$

$$\begin{aligned} \frac{d}{dt} \langle \tilde{\pi}_x \phi_y \rangle &= \langle \dot{\tilde{\pi}}_x \phi_y \rangle + \langle \tilde{\pi}_x \dot{\phi}_y \rangle \\ &= \langle \phi_{x+1} \phi_y \rangle - 2 \langle \phi_x \phi_y \rangle + \langle \phi_{x-1} \phi_y \rangle - \tilde{\mu}_0^2 \langle \phi_x \phi_y \rangle - \frac{\tilde{\lambda}_0}{3!} \langle \phi_x^3 \phi_y \rangle + \langle \tilde{\pi}_x \tilde{\pi}_y \rangle \\ &= G_2(x+1, y) - 2G_2(x, y) + G_2(x-1, y) - \tilde{\mu}_0^2 G_2(x, y) + \langle \tilde{\pi}_x \tilde{\pi}_y \rangle + \\ &\quad - \frac{\tilde{\lambda}_0}{3!} G_4(x, x, x, y) , \end{aligned}$$

$$\frac{d}{dt} G_4(x, x, x, y) = \dots \quad (8.3)$$

Standard perturbation theory can be applied to non-equilibrium problems but, due to the appearance of secular terms, such approaches become invalid at late times [88]. Instead, a better approach is to first approximate observables of interest by a closed set of equations of motion. These equations can then be solved independently and, when they retain properties of the full theory such as the conservation of energy and other symmetries, can provide an approximation scheme that remains consistent and stable over long periods of time. A simple example of this kind of approximation is mean-field theory, in particular Hartree-Fock type approximations. In the  $\phi^4$  case, such an approximation can be made by replacing  $\phi_x^4 \rightarrow -3 \langle \phi^2 \rangle^2 + 6 \langle \phi^2 \rangle \phi^2$  [89]. The Heisenberg equations of motion (8.1) then read

$$\begin{aligned} \dot{\phi}_x &= \tilde{\pi}_x , \\ \dot{\tilde{\pi}}_x &= (\phi_{x+1} - 2\phi_x + \phi_{x-1}) - \tilde{\mu}_0^2 \phi_x - \frac{\tilde{\lambda}_0}{2} \langle \phi_x^2 \rangle \phi_x . \end{aligned} \quad (8.4)$$

These are simply free-field equations so that this method essentially approximates the true quantum dynamics by classical dynamics. In terms of the  $n$ -point functions, the equations of motion (8.4) form a closed set of equations and energy is conserved leading to a stable approximation scheme. For instance, the two-point function is now determined by the equations

$$\frac{d}{dt} G_2(x, y) = \langle \pi_x \phi_y \rangle + \langle \phi_x \pi_y \rangle , \quad (8.5)$$

$$\frac{d}{dt} \langle \pi_x \phi_y \rangle = \langle \phi_{x+1} \phi_y \rangle - 2 \langle \phi_x \phi_y \rangle + \langle \phi_{x-1} \phi_y \rangle - \tilde{\mu}_0^2 \langle \phi_x \phi_y \rangle - \frac{\tilde{\lambda}_0}{2} \langle \phi_x^2 \rangle \langle \phi_x \phi_y \rangle + \langle \pi_x \pi_y \rangle , \quad (8.6)$$

so that the dependence on the four-point function factorises into the contribution of two two-point functions. Unfortunately, while such methods can be accurate for short times, they will fail when quantum corrections to the dynamics becomes important e.g. during thermalisation. These methods can be enhanced somewhat by including statistical fluctuations, as in e.g. the inhomogeneous Hartree approximation [90]. The quantum dynamics is then approximated by classical-statistical dynamics which show better thermalisation over intermediate times for weak effective couplings but ultimately struggle at long times.

To incorporate quantum corrections into dynamics in a consistent way, the  $n$ -particle-irreducible ( $n$ PI) effective action  $\Gamma_n$  can be evaluated with a loop or  $1/N$  (large number of field components) expansion [91]. In terms of the  $n$ PI effective action,  $m$ -point functions, with  $m \leq n$ , are given by the stationarity conditions:

$$\frac{\delta \Gamma_n}{\delta \langle \phi_x \rangle} = 0 , \quad (8.7)$$

$$\frac{\delta \Gamma_n}{\delta \langle \phi_x \phi_y \rangle} = 0 , \quad (8.8)$$

$$\frac{\delta \Gamma_n}{\delta \langle \phi_x \phi_y \phi_z \rangle} = 0 , \quad (8.9)$$

and so on. When evaluated in a loop-expansion or similar, certain higher- $n$   $n$ PI effective actions become equivalent which allows for the derivation of closed equations of motion. For example, at two-loop order all  $\Gamma_n$  with  $n \geq 2$  are equivalent and the 2PI effective action can be used to derive closed equations of motion [88]. The resulting equations, which conserve energy and other symmetries, take the form of non-linear integro-differential equations which can be solved using standard numerical techniques. These methods lead to better long-time behaviour and the approximation of thermalisation, particularly in the case of scalar field theory [92]. However, as they are essentially semi-classical, when dealing with non-perturbative physics such as defect formation such methods have struggled [3] though they can also be adapted to have more success in specific cases [18].

## 8.2 Non-Perturbative Methods for Non-Equilibrium QFT

While in equilibrium Monte Carlo evaluation of the path integral provides as a well-developed non-perturbative method to tackle a number of different problems,

with finite fermion densities being a notable exception, there is no similar well-developed non-perturbative method for non-equilibrium QFT.

One approach that stands out as a first principles attempt at non-perturbative non-equilibrium QFT is that of the complex Langevin [93, 94]. In these techniques, an additional time dimension is introduced along with a stochastic complex Langevin field equation. For real scalar field theory, the Langevin equation can be written in terms of a complex field  $\phi_C = \phi + i\phi_I$  as

$$\frac{\partial \phi_C}{\partial \nu} = i \left( -\square \phi_C - \mu_0^2 - \lambda_0 \phi_C^3 \right) + \eta(x, \nu) , \quad (8.10)$$

where  $\nu$  is the Langevin time parameter,  $\square$  is the d'Alembert operator and  $\eta(x, \nu)$  is a noise term. Averages of observables  $O(\phi)$  over the noise terms,  $\langle O(\phi) \rangle_\eta$ , can then be associated to an effective probability distribution for the real field,  $P_{\text{eff}}(\phi, \nu)$ , by equating them to a path-integral expectation value over the real-field  $\phi$  as

$$\langle O \rangle_\eta = \frac{\int \mathcal{D}[\phi] O(\phi) P_{\text{eff}}(\phi; \nu)}{\int \mathcal{D}[\phi] P_{\text{eff}}(\phi; \nu)} . \quad (8.11)$$

The complex pseudo-distribution  $P_{\text{eff}}(\phi, \nu)$  is then governed by a Fokker-Plank equation that admits a stationary solution

$$\lim_{\nu \rightarrow \infty} P_{\text{eff}}(\phi, \nu) \sim e^{iS[\phi]} . \quad (8.12)$$

Therefore, by evaluating noise averaged observables over long Langevin times,  $\nu \gg 1$ , one should be able to approximate the true quantum observables in a systematic way and this method has seen some success in the case of scalar field theories [93]. However, a number of mathematical barriers to proving the overall validity of the method still exist [94]. Additionally, there are potentially serious unresolved practical issues such as stability [95], lack of ergodicity [94] and high computational costs in the application to gauge theories [96] all of which currently limit the applicability of the approach.

Apart from the complex Langevin, there are a number of other strategies to approximated time-evolution non-perturbatively in development. For example, in Hamiltonian truncation methods, the full Hamiltonian is represented as a matrix using a restricted basis of Gaussian states up to some energy  $E$  [97, 98]. Since the size of the Hamiltonian matrix is sufficiently restricted, matrix multiplications can be employed and the truncated Hamiltonian can be diagonalised to estimate the ground-state and low energy states in the restricted basis. Time-evolution can then be studied by expanding the time-evolution operator in terms of the Hamiltonian

matrix and acting on the approximation of the ground-state encoded as a vector using standard matrix-vector multiplication [99]. Other methods include deforming the contour of the path integral onto regions of constant phase that can be sampled [100] and canonical (operator) approaches to truncating the infinite hierarchy of field equations of motion [101].

### 8.3 Variational Methods for Time Evolution

Another non-perturbative approach to time-evolution, more typically applied within a condensed matter/quantum many body context, is the use of a variational ansatz. Just like in equilibrium, a specific choice of ansatz with some (complex) parameters  $\mathbf{z} = (z_1, z_2, \dots, z_K)$  leads to the description of a subset of quantum states. For instance, a common (unnormalised) choice in  $D = (0 + 1)$  is the ansatz [102]

$$\psi_n(\mathbf{z}) = e^{\sum_i z_i O_i(n)} \langle n | \tilde{\psi} \rangle, \quad (8.13)$$

where  $O_i(n)$  are a chosen set of matrix elements given by operators diagonal in this basis and  $|\tilde{\psi}\rangle$  is some fixed reference state. The set of all states achieved by varying the parameters  $\{z_i\}$  then forms a variational manifold for this ansatz.

Time-evolution can be approximated within a variational manifold by making the parameters time-dependent  $z_i \rightarrow z_i(t)$ . The time-dependent ansatz from the previous example then reads

$$\psi_n(t) = e^{\sum_i z_i(t) O_i(n)} |\tilde{\psi}\rangle, \quad (8.14)$$

and the parameters  $z_i(t)$  can be determined so that the evolution of the ansatz though the variational manifold approximates the true time-evolution as closely as possible. Since the ansatz can be made quite independently from any semi-classical approximation, this method can provide a fully non-perturbative approach to time-evolution.

To derive closed equations of motion in the variational case, meaning here that the equations of motion are written directly in terms of the parameters  $z_i(t)$ , the time-dependent-variational-principle (TDVP) can be applied [103]. The TDVP gives an action formulation of the Schrödinger equation and, by restricting attention to a specific variational manifold, can be used to derive equations of motion as desired. Treating the states  $|\psi\rangle$  and  $\langle\psi|$  as independent degrees of freedom, variation of the

action

$$S = \int dt L = \int dt \left[ -\frac{i}{2} \langle \dot{\psi} | \psi \rangle + \frac{i}{2} \langle \psi | \dot{\psi} \rangle - \langle \psi | H(t) | \psi \rangle \right], \quad (8.15)$$

yields the time-dependent Schrödinger equation, assuming the states are normalised for all  $t$ . One can then restrict the states in (8.15) via an ansatz to a variational manifold parametrised by a set of  $K$  real numbers  $x_1, x_2, \dots, x_K$ . The Lagrangian in (8.15) can then be written in terms of the parameters  $x_i(t)$ , energy expectation values and overlaps as

$$L = \sum_{k=1}^K i \dot{x}_k \langle \psi | \frac{\partial \psi}{\partial x_k} \rangle - \langle \psi | H(t) | \psi \rangle, \quad (8.16)$$

which again assumes that the state is normalised.

Variation of the action corresponding to (8.16) then leads to equations of motion for the parameters :

$$\dot{x}_i = \sum_j \eta^{ij} \frac{\partial \langle \psi | H(t) | \psi \rangle}{\partial x_j}, \quad (8.17)$$

where  $\eta^{ij}$  is inverse of

$$\eta_{ij} = \frac{\langle \psi | \partial \psi / \partial x_i \rangle}{\partial x_j} - \frac{\partial \langle \psi | \partial \psi / \partial x_j \rangle}{\partial x_i}, \quad (8.18)$$

which can be interpreted as a metric on the variational manifold. The equations of motion (8.17) are a closed set of coupled first-order partial differential equations of the parameters  $x_i(t)$  that typically, due to the dependence on state expectation values, will be highly non-linear.

More generally, rather than use the Lagrangian (8.15), a different Lagrangian can be used such that normalisation need not be assumed. Additionally, while any complex parametrisation of the ansatz can be written in terms of real parameters by splitting into real and imaginary parts, it is often convenient to make use of a complex parametrisation explicitly since this simplifies geometric analysis of the variational manifold, see [103] for details.

The TDVP has been applied to a wide variety of ansatz and is often combined with Monte Carlo evaluation of observables in the time-dependent variational Monte Carlo method [104, 105]. The TDVP can also be applied to the effective action which allows for the construction of variational effective action approximations, providing a link with other non-equilibrium QFT methods [106].

## 8.4 Applying Matrix Product States to the Kibble Zurek Mechanism

To study the KZM scenario in the  $\phi^4$  scalar field theory using uMPS, we would like to approximate the equal time two-point function

$$\begin{aligned} G_2(k, t) &= \langle \Omega | \phi(-k, t) \phi(k, t) | \Omega \rangle \\ &= \langle \psi(t) | \phi(-k) \phi(k) | \psi(t) \rangle , \end{aligned} \quad (8.19)$$

where the time-dependence is generated by the lattice Hamiltonian

$$\begin{aligned} \tilde{H}[\phi, t] &= \sum_x \left[ \frac{1}{2} (\tilde{\pi}_x)^2 + \frac{1}{2} (\partial_x \phi)^2 + \frac{\tilde{\mu}_0^2(t)}{2} \phi_x^2 + \frac{\tilde{\lambda}_0}{4!} \phi_x^4 \right] , \\ \tilde{\mu}_0^2(t) &= -\frac{t}{\tau_Q} + \tilde{\mu}_0^2(t=0) , \quad t < t_F , \\ \tilde{\mu}_0^2(t) &= \tilde{\mu}_0^2(t=t_F) , \quad t \geq t_F . \end{aligned} \quad (8.20)$$

The state is initially in the ground-state  $|\psi(t=0)\rangle = |\Omega(\tilde{\mu}_0^2(t=0))\rangle$  and the explicit time-dependence of the Hamiltonian drives the system from the symmetric phase into the symmetry broken phase stopping at  $\tilde{\mu}_0^2(t_F)$  where the state is allowed to “relax” by evolving under the final time-independent Hamiltonian.

The initial state can be approximated using the vuMPS algorithm to produce  $|\Omega[A]\rangle$ , a uMPS approximation to the ground-state at  $t=0$ . In principle, the time dependent state  $|\psi(t)\rangle$  can then be approximated by evolving the initial ground-state uMPS approximation  $|\Omega[A]\rangle$  according to the Schrödinger equation

$$\begin{aligned} \frac{d}{dt} |\psi(t)\rangle &= -i\tilde{H}(t) |\psi(t)\rangle , \\ |\psi(t=0)\rangle &= |\Omega[A]\rangle . \end{aligned} \quad (8.21)$$

Unsurprisingly, this equation cannot be solved efficiently in general and there are a number of different strategies to approximate it using MPS.

In the case of finite-size, OBC MPS, a common approximation of time evolution is achieved by first breaking up the unitary time-evolution operator into small time-steps and applying one operator at a time. Such an application will lead to increased bond-dimension in the MPS representation. This is to be expected on physical grounds as time evolution tends to increase the entanglement in a state, as found e.g. when studying the time evolution of states under sudden “quenches” of the

Hamiltonian [107, 108]. In the sudden quench case, the entropy of entanglement can increase linearly with time  $S_{\mathcal{A}} \sim t$  which would require a bond-dimension  $\log(\chi) \sim t$  to represent exactly i.e. one that is increasing exponentially with time. To control this increasing bond-dimension the standard strategy, which is given in its most established form by the “time evolving block decimation” (TEBD) algorithm [109], is to allow the bond-dimension to grow  $\chi \rightarrow \chi'$  at each step before truncating the MPS back down  $\chi' \rightarrow \chi$  in some way that approximates the higher bond-dimension state accurately. A number of methods related to this exist, see e.g. [60, 110], and one can view this as a subset of methods in which the time-evolution of a  $D = (1 + 1)$  system is expressed as a two-dimensional tensor network which can then be contracted by some approximation scheme [111].

## 8.5 Time Dependent Variational Principle for uMPS

Rather than attempt to solve the Schrödinger equation (8.21) by direct approximation, the time-dependent variational principle can instead be applied to the MPS/uMPS ansatz in order to derive closed equations of motion within the variational manifold [71]. For uMPS, which we will use in Chapter 9, the variational parameters  $x_i$  are encoded in the rank-3 parameter tensor  $\mathbf{A}^n$ . The TDVP equations of motion for the parameters (8.17) can then be written as first-order differential equations in the parameter tensor as

$$\dot{\mathbf{A}}^n = -i\tilde{\mathbf{B}}^n[A], \quad (8.22)$$

where  $\tilde{\mathbf{B}}^n[A]$  is some rank-3 tensor that can be constructed from  $A$  [112]. The dependence of  $\tilde{\mathbf{B}}^n[A]$  on  $A$  is such that the various components of  $A$  are coupled in a highly non-linear way, though it can still be constructed relatively easily and efficiently. The TDVP equation of motion (8.22) can be solved with standard techniques such as Runge-Kutta and conserves energy along with other symmetries of the theory. This means it should remain stable over relatively long periods of time and there has been some success in studying thermalisation with this method [113].

To gain some intuition for the equation of motion (8.22) and the definition of the tensor  $\tilde{\mathbf{B}}^n[A]$ , the equations can be derived from an equivalent geometric picture that we outline in this Section, see [112, 114] for details. The subset of states defined by the infinite size uMPS forms a smooth manifold  $\mathcal{M}_{\text{uMPS}}$  [115]. As such, in order for a time evolved state to stay within the subset of uMPS states with

fixed bond-dimension, only tangent vectors  $|\Phi\rangle \in \mathbb{T}_{|\psi(A)\rangle} \mathcal{M}_{\text{MPS}}$  to the current state  $|\psi[A]\rangle$  can be used to update the state. Thus, the full time-evolution of the state can be approximated by projecting the right-hand-side of the Schrödinger equation (8.21) down to the tangent space of the state. The projector to the tangent state at this point can be written as  $\hat{P}_{\mathbb{T}_{|\psi(A)\rangle} \mathcal{M}_{\text{MPS}}}$  such that the desired evolution is given by the equation

$$\frac{d}{dt} |\psi(t)\rangle = -i \hat{P}_{\mathbb{T}_{|\psi(A)\rangle} \mathcal{M}_{\text{MPS}}} \left[ \hat{H} |\psi(t)\rangle \right]. \quad (8.23)$$

Such a projection is equivalent to finding the tangent vector  $|\tilde{\Phi}\rangle \in \mathbb{T}_{|\psi(A)\rangle} \mathcal{M}_{\text{MPS}}$  which satisfies the minimisation problem

$$|\tilde{\Phi}\rangle = \arg \min_{|\Phi\rangle} \| |\Phi\rangle + i \tilde{H} |\psi(t)\rangle \|^2. \quad (8.24)$$

This problem can be solved explicitly by finding representations for the tangent vectors  $|\Phi\rangle$  as a tensor network. Since the tangent space is spanned by the set of  $d\chi^2$  partial derivatives  $\frac{\partial}{\partial A_{\alpha,\beta}^n} |\psi\rangle = |\partial_i \psi\rangle$ , a tangent state can be written as a sum of these basis elements

$$|\Phi[B]\rangle = B^i |\partial_i \psi\rangle, \quad (8.25)$$

and is therefore specified by the rank-3 coefficient tensor  $B^i = B_{\alpha,\beta}^n$  of size  $(d, \chi, \chi)$ . Since  $|\psi\rangle = |\psi[A]\rangle$  is defined by a uMPS the partial derivatives can further be evaluated and represented as tensor networks via the product rule. This produces a sum of states  $|\Xi(m)\rangle$  which can be represented as uMPS but with a tensor at the site  $m$  removed. The tangent state  $|\Phi[B]\rangle$  can then be written as a sum of such states with the coefficient tensor  $B_{\alpha,\beta}^n$  inserted at site  $m$  such that

$$\Xi_{\mathbf{n}_x}(m) = \left( \prod_{x=-\infty}^{m-1} \mathbf{A}^{n_x} \right) \mathbf{B}^{n_m} \left( \prod_{x=m+1}^{\infty} \mathbf{A}^{n_x} \right), \quad (8.26)$$

and

$$|\Phi[B]\rangle = \sum_m |\Xi(m)\rangle. \quad (8.27)$$

This expression can then be used to determine the tangent space projector, or equivalently inserted into the minimisation problem (8.24). This equation can then be solved to determine  $|\tilde{\Phi}[\tilde{B}]\rangle$  and the coefficient tensor  $\tilde{B}[A]$ , which provides the right-

hand-side in the equations of motion (8.22). This procedure, which initially seems quite different to the standard MPS time-evolution procedures, is actually closely related, see [116] for more details and an overview of the general method.

# Chapter 9

## Studying the KZM with MPS

### 9.1 Introduction

In this chapter, which follows the work of the author published in [117], we apply TN techniques to the KZM. On the one hand, we would like to confirm the KZM description of the  $\phi^4$  theory driven through a quantum phase transition. On the other, we want to check that TN methods are indeed able to capture the physics of topological defect formation in a QFT. This, in addition to giving useful practical information about how TN approximations should be applied to non-equilibrium calculations, will allow us to benchmark them as a non-perturbative non-equilibrium QFT method.

We will study the KZM scenario via the lattice regularised Hamiltonian (4.2) with a time-dependent bare mass

$$\begin{aligned}\mu_0^2(t) &= -\frac{t}{\tau_Q} + \mu_0^2(t=0) , \quad t < t_F , \\ \mu_0^2(t) &= \mu_0^2(t_F) , \quad t \geq t_F ,\end{aligned}\tag{9.1}$$

where, as in Chapter 7, all quantities are in lattice units with tildes dropped for ease of notation. The time-dependence (9.1) is used to drive a ground state  $|\Omega(\mu_0^2(t=0))\rangle$  from the symmetric phase  $\mu_0^2(t=0) > m_C^2$  into the broken symmetry phase  $\mu_0^2(t_F) < m_C^2$  where it relaxes under a time-independent Hamiltonian with bare mass  $\mu_0^2(t_F)$ . The initial ground-state is approximated by a uMPS using the vuMPS algorithm, while the time-evolution is approximated by evolving the initial uMPS according to the TDVP projected Schrödinger equation (8.23) using a 5<sup>th</sup> order Runge-Kutta scheme.

As the physics of this non-equilibrium scenario is described by the Kibble-Zurek

mechanism of topological defect formation, we will compare the uMPS approximation of the equal-time two-point function  $G_2(k) = \langle \psi(t) | \phi(-k) \phi(k) | \psi(t) \rangle$ , obtained via a discrete cosine transform of  $G_2(r)$ , to the KZM expectations. In particular, we assume that the post-transition non-equilibrium two-point function is approximated by the defect ansatz (3.25) such that  $G_2(k) \approx G_{\text{def}}(k)$  and we check the consistency of this assumption in several stages.

Firstly, we compare the initial evolution of  $G_2(k=0)$  within the symmetric phase, which provides a measure of the correlation length  $\xi$ , to its equilibrium value  $G_2^\Omega(k=0)$ . We confirm that equilibrium is lost at a distance  $\hat{\epsilon} = \hat{\mu}_0^2 - m_C^2$  from the critical point and that  $\hat{\epsilon}$  scales as expected with the quench rate  $\tau_Q$ . Secondly, we study the time averaged equal time two-point function  $\bar{G}_2(k=0)$  in the broken symmetry phase, confirming that it also scales as expected and provides a consistent estimate of the defect density  $n_{\text{est}}$  (3.27) under the assumption that  $\bar{G}_2(k=0) = G_{\text{def}}(k=0)$ . Thirdly, we show that the observable  $G_{\text{uni}}(k)$  (9.6) is a universal function of  $n$  for low  $k$  and that it is described by the functional form of  $G_{\text{corr}}(k/n)$  (3.22). Furthermore, by including the contribution of the kink profile via a semiclassical approximation of  $G_{\text{kink}}(kd_K)$ , the function  $G_{\text{uni}}(k)/G_{\text{kink}}(kd_K)$  is also a universal function of  $n$  but now over a larger region of  $k$ . Finally, we show that  $\bar{G}_2(k) \approx G_{\text{def}}(k)$  for all  $k$  by including the matter contributions  $G_{\text{mat}}(k)$  (9.4) to the defect ansatz via a two-parameter fit. This then demonstrates that the two-point function of the post transition state is approximated by a form consistent with the KZM and displays clear signatures of universal topological defect formation.

## 9.2 Picking the Parameters for Time Evolution

To justify the explicit setup used to study the KZM (i.e. the choices of  $\mu_0^2(0)$ ,  $\mu_0^2(t_F)$  and  $\tau_Q$ ) we can examine the equilibrium physics of the theory. The important parameter regions can be identified by fixing the bare coupling and calculating  $m_S$  and  $M_K$  for various bare masses, here using the excitation ansatz method for  $m_S$ , and the TPBC method for  $M_K$ . These approximations to the scalar mass and kink mass are plotted in Figure 9.1 which demonstrates the various regions of interest.

To approximate the behaviour of the quantum field theory in the lattice regularised setting, we will be interested in working in the ‘‘continuum region’’ such that  $\xi > 1$  corresponding to  $m_S < 1$ . In this region, the effects of the lattice regularisation will be small and we will only consider evolutions that take place within this region.

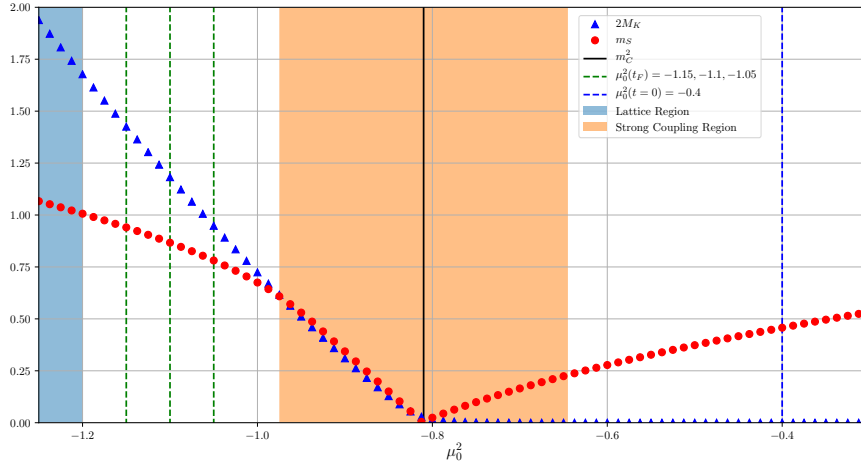


Figure 9.1: The scalar mass  $m_S$  (red circles) and twice the kink mass  $2M_K$  (blue triangles) as estimated using the tensor network techniques described in [72] with  $d = 18, \chi = 16$  and [84] with  $d = 18, \chi = 14, N = 32$  respectively. These quantities map out the important parameter regions studied by sweeping  $\mu_0^2$  for a fixed  $\lambda_0 = 3$ . The leftmost shaded region corresponds to the “lattice region” where  $m_S > 1$  such that lattice effects are important and should be excluded to get a good comparison with the KZM. Furthermore, the initial and final bare masses  $\mu_0^2(t = 0)$  and  $\mu_0^2(t_F)$ , indicated by the dashed vertical lines, should lie outside the shaded “strong-coupling region” where, in the broken symmetry phase,  $m_S \approx 2M_K$  and the kink-antikink excitations behave as standard scalar excitations.

Furthermore, we are interested in setting  $\mu_0^2(t_F)$  to lie outside the “strong coupling” region in the broken symmetry phase where  $m_S = 2M_K$  and kink-antikink pairs do not behave like classical extended objects but as standard particles. These two considerations then both limit the potential choices of  $\mu_0^2(t_F)$  and we have indicated the set of  $\mu_0^2(t_F)$  we use in Figure 9.1. The initial  $\mu_0^2(0)$  is also chosen to lie outside the strong-coupling region in the symmetric phase and a set of quench rates  $\tau_Q$  are chosen so that it is possible to maintain equilibrium into the strong-coupling region such that the scaling arguments (3.3) from the KZM can be applied. While increasing the bare coupling  $\lambda_0$  enlarges the strong-coupling region so that lower  $\tau_Q$  are required, it also shrinks the available continuum region in the broken symmetry phase that lies outside the strong-coupling region, and we have found  $\lambda_0 = 3$  to provide a good balance.

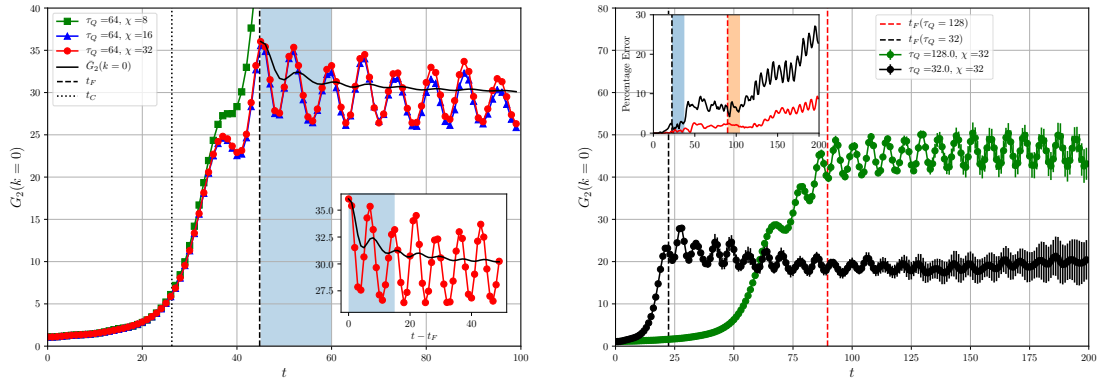


Figure 9.2: The evolution of  $G_2(k=0)$  is shown for  $\tau_Q = 32, 64$  and  $128$ . The left-hand plot shows the approximation for  $\tau_Q = 64$  with  $\chi = 16$  (blue triangles),  $\chi = 32$  (red circles) and an additional  $\chi = 8$  (green squares) for comparison. The  $\chi = 8$  approximation deviates significantly from the  $\chi = 16$  and  $\chi = 32$  approximations following  $t \approx t_C$  where  $t_C$  is the time when  $\mu_0^2(t) = m_C^2$ . Until the start of relaxation at  $t = t_F$  (vertical dashed line), the two higher  $\chi$  approximations are close on this scale, but deviate visibly during the relaxation period. This is also the case for other  $\tau_Q$  as shown in the right-hand plot where the maximum difference between the  $\chi = 16, 20, 24, 28$  and  $\chi = 32$  approximations is represented by errorbars. This difference as a percentage of the value of  $G_2(k=0)$  for  $\chi = 32$  is shown in the inset where, following  $t_F$ , it can be seen that the difference becomes significant and the time-evolution has been extended up to  $t = 200$  to illustrate the increase of errors with time. During the relaxation period, the value of  $G_2(k=0)$  displays large oscillations which can be removed by time averaging as shown in the left-hand plot (solid black line). While the plots show the time-evolution up to a maximum  $t = 100$  for  $\tau_Q = 64$  and  $t = 200$  for  $\tau_Q = 32, 128$ , we will only be interested in comparing different  $\tau_Q$  at the same “relaxation time” i.e. at the same time after  $t_F$ . The maximum time used for analysis is then different for each  $\tau_Q$  and the shaded regions indicate the data used in subsequent analysis from  $t = t_F$  to  $t = t_F + 15$ .

### 9.3 Time Evolution, Calculation of $G_2(k)$ and Time-Averaging

With the parameters for the evolutions fixed and an approximation of the initial state obtained by a uMPS with bond-dimension  $\chi$ , the equal-time two-point function can be approximated by numerically integrating the evolution equation (8.22). We do this for a set of  $\chi = 16, 20, 24, 28, 32$  using a 5<sup>th</sup> order Runge-Kutta scheme with time step  $\tau = 10^{-2}$  and local basis truncation  $d = 18$  up to total time  $T = 100$  with the observable  $G_2(k)$  being evaluated every 100 steps. The time evolution of  $G_2(k=0)$  for the case of  $\mu_0^2(t_F) = -1.1$  and  $\tau_Q = 32, 64, 128$  is shown in Figure 9.2 which illustrates several features of the evolution and approximations used.

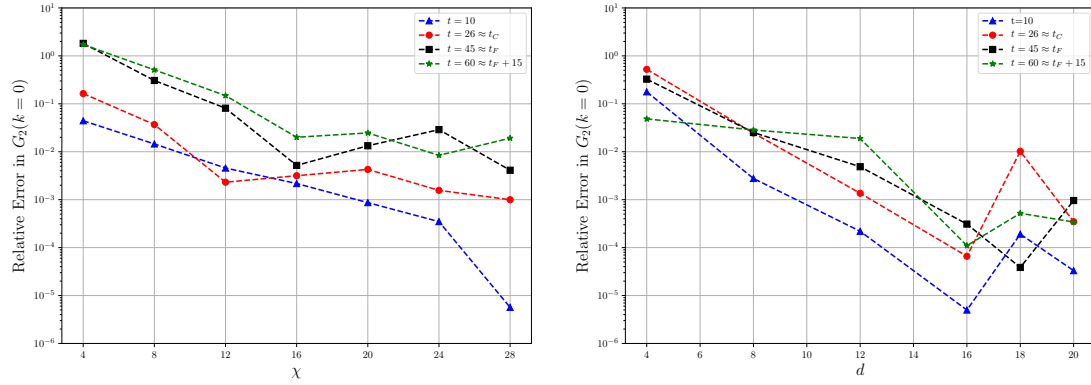


Figure 9.3: The “Relative Error” of  $G_2(k=0)$ , defined as the fractional difference between the value of  $G_2(k=0)$  for a given  $\chi$  or  $d$  and the maximum  $\chi = 32$  or  $d = 24$ , is shown for  $\tau_Q = 64$ ,  $\mu_0^2(t_F) = -1.1$  and four times  $t = 10, 26, 45, 60$ . In the left-hand plot, the error decreases with  $\chi$  for a fixed time while later times tend to have a higher overall error. However, the convergence is not smooth and, as can be seen in the  $t = 45$  and  $t = 60$  plots at  $\chi = 24$ , for some values of  $\chi$  the error at earlier times may appear greater than at some later times. This leads to a somewhat noisy error estimate for  $\chi = 32$  over time, defined as the maximum error for all  $\chi \geq 16$ , as can be seen in the right-hand inset of Figure 9.2. For  $\tau_Q = 64$  the latest time used in subsequent analysis is  $t = 60$ . For all  $t \leq 60$  the fractional error remains less than  $10^{-1}$  for all  $\chi \geq 16$ . In the right-hand plot, the relative error is shown for the truncation parameter  $d$  with fixed  $\chi = 16$ . At the times  $t \geq t_F$  used for subsequent analysis, the relative errors for  $d \geq 16$  are all below  $10^{-3}$  indicating that it is the error due to  $\chi$  that is most relevant. As such, we simply fix  $d = 18$  throughout and use the error on  $\chi$  as our error estimate when performing fits.

In the left-hand plot of Figure 9.2, the value of  $G_2(k=0)$  is shown for  $\tau_Q = 64$  and  $\chi = 16, 32$ . Initially, the difference between the two is small, being almost indistinguishable on this scale prior to the critical point (dotted vertical line) but the difference becomes significant during the “relaxation” portion of the evolution at  $t > t_F$  (dashed vertical line). Ideally, we would like to make a set of approximations for different  $\chi$  and extrapolate to the  $\chi \rightarrow \infty$  limit where the evolution of the regularised theory is exact. While this is possible in some cases where the convergence of observables is particularly smooth, it is difficult in others especially at later times when we no longer expect the state itself to be well described by uMPS with limited bond-dimension, even if the observable of interest itself can be reasonably approximated. As such, we instead make a simple estimate of the error by taking the maximum absolute difference between the  $\chi = 16, 20, 24, 28$  and highest  $\chi = 32$  approximations which we use as an input when fitting curves and display as error bars in plots (see Figure 9.3 for more discussion of the errors due to  $\chi$  and  $d$ ). The right-hand plot of Figure 9.2 shows the evolution of the two  $\tau_Q = 32$  and  $\tau_Q = 128$

quenches along with the error bars. Once again, the most significant errors occur at later times  $t \gg t_F$  as the system relaxes. In the  $\tau_Q = 32$  cases, there are then significant errors occurring at much earlier absolute time  $t$  than for the corresponding  $\tau_Q = 128$ , as shown in the inset which gives the error as a percentage of the value of  $G_2(k=0)$ . However, we will not be interested in comparing different  $\tau_Q$  quenches at the same absolute time but rather at the same relaxation time  $t_R = t - t_F$  after the quench ends. As such we will not be interested in the regions with the most significant errors far from the point  $t_F$  (the dashed black and red vertical lines) such that the errors in different  $\tau_Q$  quenches will be much closer than if taken at the same absolute time.

In addition to the errors, the plots in Figure 9.2 display temporal oscillations in  $G_2(k=0)$ , particularly during the relaxation period, that are characteristic of the non-equilibrium dynamics of quenched systems, as often found when studying instantaneous  $\tau_Q \rightarrow 0$  quenches [89]. While there may be some physical damping of these oscillations over time, the time-scale on which this occurs is longer than the time-scales we have approximated. Because of this, rather than focus on the equal-time two-point function directly, we will instead use the time-averaged two-point function  $\bar{G}_2(k)$  given by averaging over the available data for  $G_2(k)$  after the final bare mass  $\mu_0^2(t_F)$  has been reached and relaxation begins such that

$$\bar{G}_2(k, t_R) = \frac{1}{t_R} \int_{t_F}^{t_F+t_R} G_2(k, T) dT. \quad (9.2)$$

This observable can then be used to provide a clean comparison with the expected KZM behaviour and displays a similar error for different  $\tau_Q$  quenches given a fixed relaxation time  $t_R$ . The value of  $\bar{G}_2(k=0)$  for the  $\tau_Q = 64$  case with  $\chi = 32$  is shown in the left-hand plot of Figure 9.2 with the inset displaying some of the region  $t > t_F$  where the averaging can be clearly seen.

## 9.4 Loss of Equilibrium

To check the initial evolution of the system up to the critical point, we compare the behaviour of  $G_2(k=0)$  to the equilibrium value  $G_2^\Omega(k=0)$ . The KZM states that initially the state should remain in equilibrium such that  $G_2(k=0) = G_2^\Omega(k=0)$  before becoming excited at some point  $\hat{\epsilon} = \mu_0^2 - m_C^2$  before the critical point. The KZM further provides an estimate for the scaling of  $\hat{\epsilon}$  with the quench rate  $\tau_Q$  such that  $\hat{\epsilon} \sim \tau_Q^{-1/2}$  when  $\tau_Q$  is sufficiently large to probe the critical region. Figure

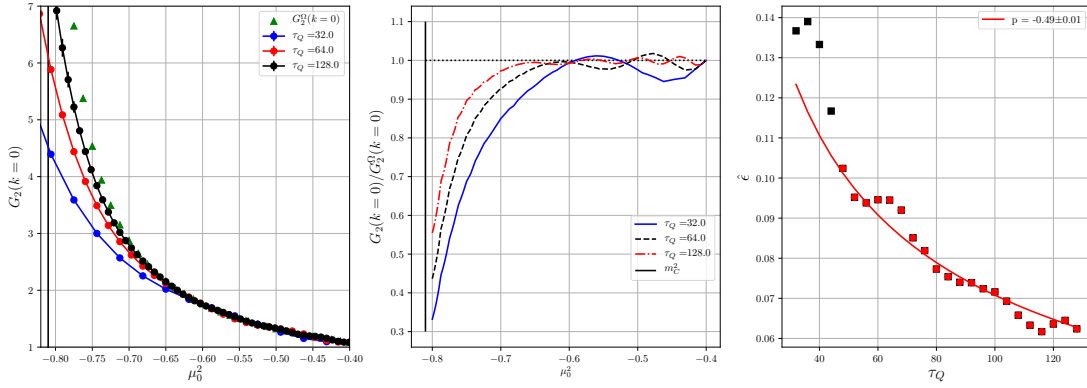


Figure 9.4: Plots of the time evolution of  $G_2(k=0)$  up the critical point  $m_c^2$  (vertical solid black line). In the leftmost plot this is compared with the ground state value (green triangles) with the increasing  $\tau_Q$  remaining close to this value for a larger region of  $\mu_0^2$ . In the central plot, the ratio of  $G_2(k=0)$  to the ground-state value is plotted using interpolating functions, showing the departure from equilibrium more clearly. This also allows for a criterion for the loss of equilibrium to be established and we used the condition  $G_2(k=0)/G_2^\Omega(k=0) = 0.9$  to define  $\hat{\epsilon} = \hat{\mu}_0^2 - m_c^2$  as the point where equilibrium is lost. The value of  $\hat{\epsilon}$  is shown in the rightmost plot where the larger  $\tau_Q$  data (red circles) are fit to a power-law.

9.4 illustrates this behaviour through the evolution of  $G_2(k=0)$  (leftmost plot), the ratio  $G_2(k=0)/G_2^\Omega(k=0)$  constructed using interpolating functions (centre plot) and a comparison of  $\hat{\epsilon}$  with  $\tau_Q$ , where  $\hat{\epsilon}$  is estimated by the point at which  $G_2(k=0)/G_2^\Omega(k=0) = 0.9$  (rightmost plot). The scaling of  $\hat{\epsilon}$  is established using a power-law fit to the points shown in red to give  $\hat{\epsilon} \sim \tau_Q^{-0.49 \pm 0.01}$  close to the  $\tau_Q^{-1/2}$  predicted by the KZM.

## 9.5 Estimating the Defect Density

As the system enters the broken symmetry phase, the value of  $G_2(k=0)$  continues to grow, but the scaling established at the point  $\hat{\epsilon}$  should be retained. Furthermore, once in the symmetry broken phase and after sufficient relaxation time, we can interpret the time-average  $\bar{G}_2(k=0)$  via the defect ansatz  $G_{\text{def}}(k=0)$  such that  $\bar{G}_2(k=0) - G_2^\Omega(k=0) \approx v^2/n$ , where the vacuum expectation value  $v(\mu_0^2)$  is determined from the corresponding uMPS approximation of the ground-state  $v = \langle \Omega[A] | \phi | \Omega[A] \rangle$ . The value of  $\bar{G}_2(k=0) - G_2^\Omega(k=0)$  is shown in Figure 9.5 (left-hand plot) for the  $\mu_0^2(t_F) = -1.1$  case with  $t_R = 0$  and  $t_R = 15$ . In the first case, the oscillatory behaviour is clearly visible as different  $\tau_Q$  lie at different

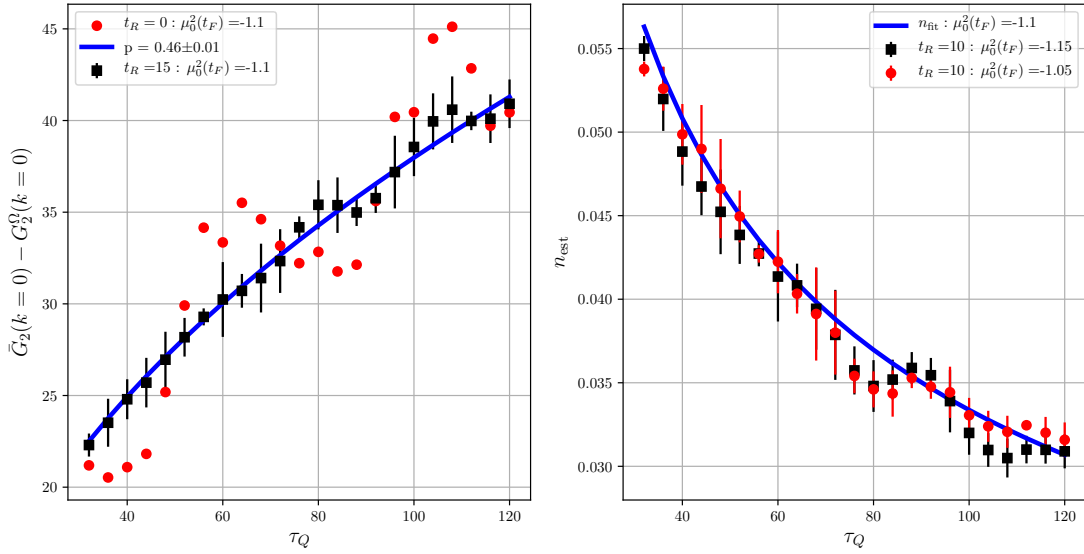


Figure 9.5: The value of  $\bar{G}_2(k=0)$  with the vacuum subtracted is shown (left-hand plot) for  $t_R = 0$  and  $t_R = 15$ . In the former case, there are large oscillations present in the data as different  $\tau_Q$  quenches lie in different phases of their evolution. These oscillations are significantly damped at  $t_R = 15$  by the time-averaging and a power-law fit has been taken. The defect density corresponding to this power-law fit  $n_{\text{fit}}$  is shown in the right-hand plot which can be compared to the estimates  $n_{\text{est}}$  (3.27) for  $\mu_0^2(t_F) = -1.05, -1.15$  at  $t_R = 10$ . The data lies fairly close to the fit though the larger  $\tau_Q$  data still displays clear oscillations.

phases of their evolution. However, in the second case this behaviour is damped significantly by the time-averaging. A power-law fit of the  $t_R = 15$  data scales as  $\tau_Q^{0.46 \pm 0.01}$ . This value is somewhere between the classical  $\tau_Q^{1/3}$  and quantum  $\tau_Q^{1/2}$ , though closer to the latter.

The estimate of the defect density  $n_{\text{est}}$  (3.27) is shown in the right-hand plot of Figure 9.5 for the cases  $\mu_0^2(t_F) = -1.15$  and  $-1.05$ . The agreement between the different  $\mu_0^2(t_F)$  and  $n_{\text{est}}$  obtained from the power-law fit of  $\bar{G}_2(k=0) - G_2^\Omega(k=0)$  is reasonable, consistent with the interpretation that  $\bar{G}_2(k=0) \approx v^2/n$ , though the large  $\tau_Q$  data still displays oscillations for this  $t_R$  and the low  $\tau_Q$  data for  $\mu_0^2(t_F) = -1.15$  lies somewhat below  $n_{\text{fit}}$  indicating that longer relaxation times and slower quenches could improve the agreement further. Nevertheless, this data suggests that  $\bar{G}_2(k=0)$  can indeed provide a simple observable with which to estimate the defect density in a quantum field theory.

## 9.6 Using The Defect Ansatz with Tensor Networks

With the defect density estimated, we now want to compare the form of  $\bar{G}_2(k)$  to that of  $G_{\text{def}}(k)$  (3.25) as outlined in Section 3.3. In particular, we want to compare the observable

$$\frac{n_{\text{est}}}{v^2} \frac{\bar{G}_2(k) - G_2^\Omega(k) - G_{\text{mat}}(k)}{G_{\text{kink}}(kd_K)} \quad (9.3)$$

to  $G_{\text{corr}}(k)$  (3.22) which should be equal and a function of  $k/n$  only if the KZM holds and the TN methods are capturing the defect formation correctly. However, as mentioned previously, we must make further approximations to calculate the quantities in (9.3) and rather than comparing (9.3) directly to  $G_{\text{corr}}(k)$  as might be possible classically, it is better to break up the comparison to test the accuracy of the approximations along the way.

The approximation of the kink-profile term  $G_{\text{kink}}(k)$  can in principle be done using non-perturbative methods by calculating the one-kink two-point function  $\langle K | \phi(-k) \phi(k) | K \rangle$ . However, this calculation is more difficult than the corresponding vacuum one and we will instead use a semi-classical approximation by combining the classical kink profile term (3.21) with the semi-classical width  $d_K = \sqrt{2}/m_S$ . Importantly, this approximation is still unambiguous requiring no fitting and completely independent of the other non-equilibrium calculations.

Unfortunately, the computation of the matter term  $G_{\text{mat}}(k)$  is somewhat more complicated and more approximations are required. In this case we assume that, given sufficient relaxation time, the matter excitations will “thermalise” in the sense that the two-point function  $G_{\text{mat}}(k)$  can be approximated by the two-point function of a thermal state with the vacuum subtracted i.e.  $G_{\text{mat}}(k) \approx \Delta G_{\text{therm}}(k)$  with  $\Delta G_{\text{therm}}(k) = \frac{1}{\mathcal{Z}} \text{tr} [\rho \phi(-k) \phi(k)] - G_2^\Omega(k)$ ,  $\rho = \frac{1}{\mathcal{Z}} e^{-\beta H}$  and  $\mathcal{Z} = \text{tr} [\rho]$ . Under this assumption, the matter contributions  $G_{\text{mat}}(k)$  are then also given by an independent equilibrium quantity and there exist non-perturbative methods to evaluate this. However, in the present case we will again use a semi-classical approximation by taking the non-interacting form such that

$$G_{\text{mat}}(k) \approx \frac{1}{\omega_k (e^{\beta \omega_k} - 1)}, \quad (9.4)$$

where  $\omega_k$  is the non-interacting lattice dispersion relation

$$\omega_k = \sqrt{\mu^2 + 4 \sin\left(\frac{p}{2}\right)^2} \quad (9.5)$$

and the inverse temperature  $\beta$  and mass  $\mu$  are treated as free parameters.

Since we do not calculate  $G_{\text{mat}}(k)$  a priori and we only know the form of  $G_{\text{kink}}(kd_K)$  approximately, we cannot simply determine the universal part of  $G_2(k)$  and compare it with  $G_{\text{corr}}(k/n)$  as desired. Instead, we will first focus on the region  $k/n \ll d_K^{-1}/n$  where the contributions from the kink profile and matter should be negligible. Defining the observable

$$\begin{aligned} G_{\text{uni}}(k) &= \frac{n_{\text{est}}}{v^2} [\bar{G}_2(k) - G_2^\Omega(k)] \\ &= \frac{\bar{G}_2(k) - G_2^\Omega(k)}{\bar{G}_2(k=0) - G_2^\Omega(k=0)}, \end{aligned} \quad (9.6)$$

we should then find that  $G_{\text{uni}}(k) \approx G_{\text{corr}}(k/n)$  under the assumption that  $\bar{G}_2(k) = G_{\text{def}}(k)$  such that the non-equilibrium observable  $G_{\text{uni}}(k)$  should be a universal function of  $n$  for low  $k$  and we can attempt to fit it to the functional form of  $G_{\text{corr}}(k/n)$  in this region. We can then compare this to the behaviour of the observable  $G_{\text{uni}}(k)/G_{\text{kink}}(kd_K)$  using the semi-classical approximation of  $G_{\text{kink}}(kd_K)$ . If the assumption  $\bar{G}_2(k) = G_{\text{def}}(k)$  holds and the semi-classical approximation for  $G_{\text{kink}}(kd_K)$  is accurate, then  $G_{\text{uni}}(k)/G_{\text{kink}}(kd_K)$  should be a universal function of  $n$  over a larger region up to  $k \approx d_K^{-1}$  where we can still neglect the matter term. The fit  $G_{\text{corr}}(k/n)$  should then also hold for this larger region and we can use this to estimate the universal parameters  $\alpha_1, \alpha_2, \beta_1, \beta_2$ .

The comparison between the two-point function  $\bar{G}_2(k)$  and the defect ansatz can then be completed via a two parameter fit using the ansatz for the matter contribution (9.4) and we should then find that  $\bar{G}_2(k) \approx G_{\text{def}}(k)$  over the full range of  $k$  and several orders of magnitude in the observable.

## 9.7 Universality of $G_2(k)$ with Defect Density

Following the above discussion, the comparison of  $\bar{G}_2(k)$  and  $G_{\text{def}}(k)$  continues by scaling the data using the estimated  $n_{\text{est}}$  and examining the observables  $G_{\text{uni}}(k)$  (9.6) and  $G_{\text{uni}}(k)/G_{\text{kink}}(kd_K)$  using the semi-classical approximation for  $G_{\text{kink}}(kd_K)$ . If indeed  $\bar{G}_2(k) = G_{\text{def}}(k)$  then  $G_{\text{uni}}(k)$  should be a universal function of  $n$  up

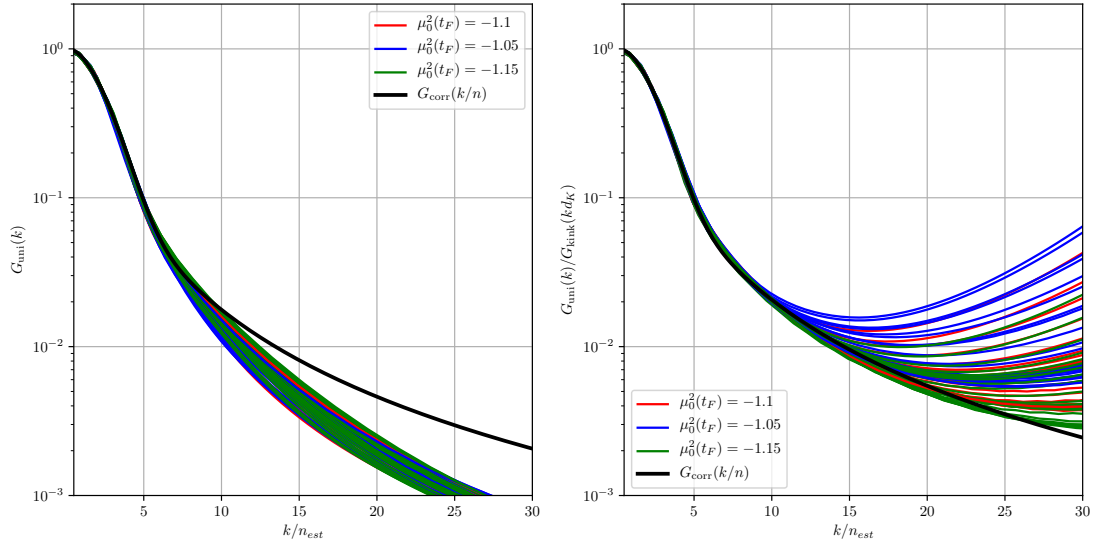


Figure 9.6: Plots of  $G_{\text{uni}}(k)$  (9.6) (left-hand plot) and  $G_{\text{uni}}(k)/G_{\text{kink}}(kd_K)$  (right-hand plot) for  $\tau_Q = 32, 36, 40, \dots, 128$  along with fits to the form functional form  $G_{\text{corr}}(k)$  (3.24). In the left-hand plot, the data collapses up to  $k/n_{\text{est}} \approx 5$  indicating a universal function of the defect density up to this point. With the inclusion of kink profile  $G_{\text{kink}}(kd_K)$  in the right-hand plot the universal region is increased to  $k/n_{\text{est}} \approx 10$  indicating that the semi-classical approximation for  $G_{\text{kink}}(kd_K)$  is accurate and that the data is consistent with kink formation in the system. The fitted form agrees well with the data in both cases within the universal regions giving  $\alpha_1, \alpha_2, \beta_1, \beta_2 = 0.683, 0.120, 0.329, 0.176$  and  $\alpha_1, \alpha_2, \beta_1, \beta_2 = 0.723, 0.128, 0.290, 0.130$  in the left-hand and right-hand plots respectively.

to a scale where the defect width  $d_K$  is important and  $G_{\text{uni}}(k) \approx G_{\text{corr}}(k/n)$ . If additionally, the approximate form of  $G_{\text{kink}}(kd_K)$  is accurate, then we can further expect the observable  $G_{\text{uni}}(k)/G_{\text{kink}}(kd_K)$  to be a universal function of  $n$  up to a somewhat higher scale where the matter contributions  $G_{\text{mat}}(k)$  become important and  $G_{\text{uni}}(k)/G_{\text{kink}}(kd_K) \approx G_{\text{corr}}(k/n)$  over this region.

Figure 9.6 shows the two observables  $G_{\text{uni}}(k)$  (left-hand plot) and  $G_{\text{uni}}(k)/G_{\text{kink}}(kd_K)$  (right-hand plot) for  $\tau_Q = 32, 36, 40, \dots, 128$  and  $\mu_0^2(t_F) = -1.05, -1.1, -1.15$  along with fits to the functional form of  $G_{\text{corr}}(k)$ . In the left-hand plot of Figure 9.6 the observable  $G_{\text{uni}}(k)$  collapses reasonably up to around  $k/n_{\text{est}} \approx 5$  and the functional form of  $G_{\text{corr}}(k)$  fits well in this region such that the approximation

$$\bar{G}_2(k) \approx \frac{v^2}{n_{\text{est}}} G_{\text{corr}}(k/n_{\text{est}}) + G_2^\Omega(k) \quad (9.7)$$

holds for these low  $k/n_{\text{est}}$ . However, for larger  $k/n_{\text{est}}$  the data begins to spread out indicating that  $G_{\text{uni}}(k)$  is not a universal function of  $n$  in this region. Furthermore,

the fit sits above the data indicating the need for an additional term to suppress it and suggesting that there is another relevant scale missing.

According to the Kibble-Zurek mechanism and the physical picture provided by the defect ansatz (3.25), this missing scale should be given by the width of defects in the system  $d_K$ . In the right-hand plot of Figure 9.6, the observable  $G_{\text{uni}}(k)/G_{\text{kink}}(kd_K)$  collapses well up until  $k/n_{\text{est}} \approx 10$ . At this point the data spreads out and begins to increase due to the division of  $G_{\text{kink}}(kd_K)$  which becomes small in this region. Nevertheless, the fit still agrees at  $k/n_{\text{est}} \approx 20$  with a number of curves for which the division by  $G_{\text{kink}}(kd_K)$  has not yet dominated. Up to this scale, we then have the approximation that

$$\bar{G}_2(k) \approx \frac{v^2}{n_{\text{est}}} G_{\text{corr}}(k/n_{\text{est}}) G_{\text{kink}}(kd_K) + G_2^\Omega(k), \quad (9.8)$$

which is the defect ansatz (3.25) with the matter contribution  $G_{\text{mat}}(k)$  neglected.

## 9.8 Comparison of $\bar{G}_2(k)$ and $G_{\text{def}}(k)$

To further check the consistency of the approximation  $\bar{G}_2(k) \approx G_{\text{def}}(k)$  we would like to account for the matter contributions. Firstly, we can check the consistency of their interpretation by comparing the data  $\bar{G}_2(k)$  to the vacuum explicitly as shown in Figure 9.7. As expected, the equal time two-point function tends to the vacuum at high  $k$  for all  $\tau_Q$  but has an additional positive contribution that is suppressed with increasing  $\tau_Q$ , consistent with the generation of additional non-vacuum excitations during the phase transition which provide the contribution  $G_{\text{mat}}(k)$  to the equal time two-point function.

We can now account for the remaining contributions to  $\bar{G}_2(k)$  by using a semi-classical ansatz for the matter contributions  $G_{\text{mat}}(k)$  (9.4). This constitutes a two parameter fit and we find that, once performed, the approximation  $\bar{G}_2(k) \approx G_{\text{def}}(k)$  holds over several orders of magnitude, as shown in Figure 9.8.

Figure 9.8 displays the defect ansatz fit (3.25) (solid black line) with the vacuum subtracted for the  $\tau_Q = 64, \mu_0^2(t_F) = -1.1$  data (red circles) along with the various components of the fit (left-hand plot). Firstly, the defect ansatz without the matter component (9.8) (dashed black line) decays rapidly to zero following the scale set by the kink width  $d_K^{-1} \approx 0.61$  (vertical dashed blue line). This is corrected by the matter contribution shown (dotted-dashed line) which is initially irrelevant but dominates at high  $k \gg d_K^{-1}$ . The full defect ansatz (solid black line) then approximates the

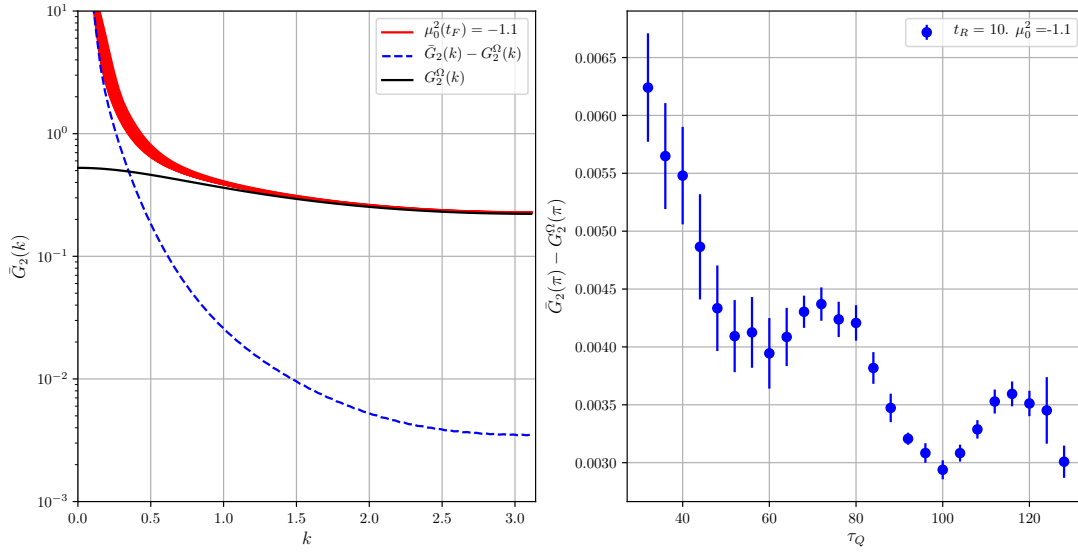


Figure 9.7: The value of  $\bar{G}_2(k)$  for  $\tau_Q = 32, 36, 40, \dots, 128$  (solid red lines) is plotted along with  $G_2^\Omega(k)$  (left-hand plot, solid black line) which agrees closely at large  $k$  as illustrated by the difference  $\bar{G}_2(k) - G_2^\Omega(k)$  (dashed blue lines). At the maximum momentum  $k = \pi$  the value of  $\bar{G}_2(k = \pi)$  still lies above the vacuum value but this positive contribution decreases with  $\tau_Q$  (right-hand plot, blue circles) consistent with the existence of additional non-vacuum contributions to  $\bar{G}_2(k)$  that are suppressed by slower quench rates.

data reasonably over the full range of  $k$ . The right-hand plot also shows the fits for the case  $\mu_0^2 = -1.05$  with lower  $\tau_Q = 40$  and higher  $\tau_Q = 116$  data (red circles and green triangles respectively). In this case, the plots behave as expected with the higher  $\tau_Q$  data starting at a larger value for low  $k$ , corresponding to a lower defect density, but ending up at a lower value since there are fewer non-vacuum excitations present.

## 9.9 Conclusion

In this chapter, we have shown that the KZM and Defect Ansatz provide a description of the non-equilibrium process of symmetry breaking in the  $\phi^4$  theory, consistent with the idea of topological defect formation during a quantum phase transition. As the non-equilibrium calculations were performed using tensor networks, these results also demonstrate that tensor networks can be considered a powerful non-perturbative non-equilibrium method for quantum field theory.

There are several areas in the previous study that can improved upon to achieve

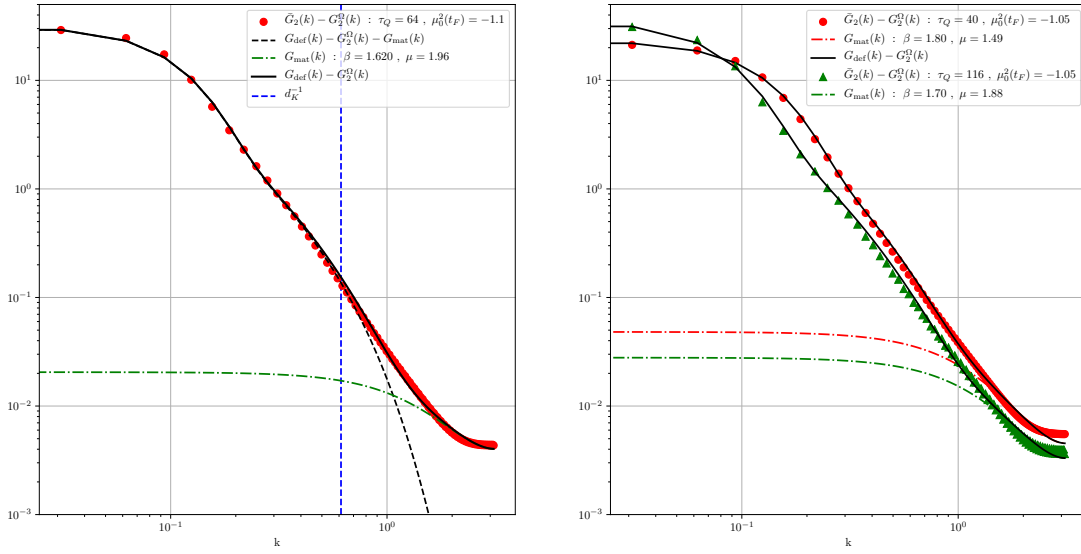


Figure 9.8: The value of  $\bar{G}_2(k) - G_2^\Omega(k)$  for  $\tau_Q = 64, \mu_0^2(t_F) = -1.1$  (left-hand plot, red circles) and  $\tau_Q = 40, 116, \mu_0^2(t_F) = -1.05$  (right-hand plot, red circles and green triangles respectively). All three observables are fitted to  $G_{\text{def}}(k) - G_2^\Omega(k)$  (3.25) via a two parameter fit with the values of  $\beta, \mu$  indicated. The  $G_{\text{mat}}(k)$  (9.4) component of  $G_{\text{def}}(k) - G_2^\Omega(k)$ , which contains the free parameters, is shown in both plots (dotted-dashed line). Initially, this component is irrelevant and the curves are described by a single universal part shown in the left-hand plot (black dashed line). In the universal part the effect of finite width kinks is clearly seen with the form being exponentially suppressed after the inverse kink width  $k \approx d_K^{-1}$  (vertical blue dashed line), such that the matter component dominates in the higher  $k$  region. In the right-hand plot the curves behave as expected with the higher  $\tau_Q$  case having a smaller matter component.

higher accuracies and a deeper understanding of the physical processes involved. Firstly, while the defect ansatz provides a reasonable approximation with the form of  $G_{\text{mat}}(k)$  given by (9.4), as (9.5) and the corresponding values of  $\mu$  and  $\beta$  were determined by fitting we cannot interpret these parameters as cleanly as we would like since they display large variations with  $\tau_Q$  that mask any overall trend. This also somewhat obscures the interpretation of the kink profile term since we cannot assess the impact of the semi-classical approximation cleanly. To improve this, it would be desirable in the future to have a non-perturbative approximation for the matter contribution  $G_{\text{mat}}(k)$ . This can be achieved by assuming, as done in this chapter, that the matter contributions can be described by thermal effects. The thermal two-point function can then be estimated by a non-perturbative method such as the *minimally entangled typical thermal states* (METTS) tensor network method [118], which takes  $\beta$  as an input with a definite interpretation as the inverse temperature and eliminates the need for the additional parameter  $\mu$ . While it is

still not clear exactly what value of  $\beta$  should be used since we do not know how energy is partitioned in the system, this would still offer a more rigorous result and we could, e.g. determine  $\beta$  by fitting to the data at large  $k$  where any effect of the kink profile should be irrelevant. If we are able to establish the form of  $G_{\text{mat}}(k)$  in this manner, we can then “measure”  $G_{\text{kink}}(kd_K)$  more directly. In principle, this can then be compared with a non-perturbative approximation of  $G_{\text{kink}}(kd_K)$  which e.g. might be obtained through a TN approximation of the equal time two-point function of the one kink state  $\langle K|\phi(-k)\phi(k)|K\rangle$ .

# Chapter 10

## Conclusion

We have studied the  $\phi^4$  quantum field theory in  $D = (1 + 1)$  spacetime dimensions in the lattice Hamiltonian framework using the matrix product state tensor network. We have focussed on the kink topological defects of the theory both in equilibrium and the process of their formation as described by the Kibble Zurek mechanism.

We have found that in equilibrium the tensor network techniques can be used to gain approximations of the one-kink state at both weak and strong couplings, potentially allowing for the calculation of a wide variety of observables. Additionally, the methods used are sufficiently general that they can be adapted to more complicated theories.

We have also investigated the non-equilibrium process of a symmetry breaking quantum phase transition in the theory and found that the resulting observables are consistent with a description of topological defect formation via the Kibble Zurek mechanism. On the one hand this provides evidence that the Kibble-Zurek mechanism holds as expected for the case of a quantum field theory undergoing a quantum phase transition. On the other, it demonstrates that tensor networks can be considered a truly non-perturbative non-equilibrium quantum field theory method.

It is now of considerable interest to see to what extent tensor networks can be applied to more realistic quantum field theories, with the long term goal of application as a non-perturbative non-equilibrium method for high energy physics and cosmology being particularly exciting. Of course, this will require the development of tensor networks into higher dimensions and to more sophisticated theories. In equilibrium, this is already an active area of research with some success being reported in  $D = (2 + 1)$  dimensions, though the situation is not yet clear. However, there is also significant opportunity for further investigation in  $D = (1 + 1)$  quantum field theories especially with regards to non-equilibrium and non-perturbative

effects. For example, studies of thermalisation, non-topological soliton formation and curved spacetimes are all, as with topological defect formation, of physical interest in their own right as they can be generalised easily to more realistic theories. Additionally, they are of technical interest as other non-equilibrium methods can prove inadequate for their treatment, allowing tensor networks to provide an immediate advantage by comparison. The parallel development of such work with the current push to higher dimensions and gauge theories should then provide a good developmental path for tensor networks, hopefully towards the treatment of realistic theories in the future.

# Bibliography

- [1] A. Milsted, J. Haegeman, and T. J. Osborne, “Matrix product states and variational methods applied to critical quantum field theory,” *Physical Review D* **88** no. 8, (Feb, 2013) 085030, [arXiv:1302.5582](#).
- [2] P. Silvi, G. Morigi, T. Calarco, and S. Montangero, “Crossover from Classical to Quantum Kibble-Zurek Scaling,” *Physical Review Letters* **116** no. 22, (Jun, 2016) 225701.
- [3] A. Rajantie and A. Tranberg, “Looking for defects in the 2PI correlator,” *Journal of High Energy Physics* no. 11, (2006) , [arXiv:hep-ph/0607292](#) [hep-ph].
- [4] M. Kleman, “Defects in liquid crystals,” *Rep. Prog. Phys.* **52** (1989) 555.
- [5] M. Yuriy and G. Henri, eds., *Topological Defects and the Non-Equilibrium Dynamics of Symmetry Breaking Phase Transitions*. Springer, Dordrecht, 1999.
- [6] A. Vilenkin and E. P. S. Shellard, *Cosmic Strings and Other Topological Defects*. Cambridge University Press, 2000.  
<http://inspirehep.net/record/1384873?ln=pt>.
- [7] A. Rajantie, “Formation of topological defects in gauge field theories,” *International Journal of Modern Physics A* **17** no. 1, (2002) 1–43, [arXiv:hep-ph/0108159](#) [hep-ph].
- [8] N. D. Mermin, “The topological theory of defects in ordered media,” *Reviews of Modern Physics* **51** no. 3, (1979) 591–648.
- [9] T. W. B. Kibble, “Topology of cosmic domains and strings,” *Journal of Physics A: Mathematical and Theoretical* **9** (1976) 1387–1398.
- [10] W. H. Zurek, “Cosmological experiments in superfluid helium?,” *Nature* **317** (1985) 505–508, [arXiv:cond-mat/9607135](#) [cond-mat].

- [11] A. del Campo and W. H. Zurek, “Universality of phase transition dynamics: Topological defects from symmetry breaking,” *International Journal of Modern Physics A* **29** no. 08, (Mar, 2014) 31–87, [arXiv:1310.1600](#).
- [12] W. Zurek, U. Dorner, and P. Zoller, “Dynamics of a Quantum Phase Transition,” *Physical Review Letters* **95** no. 10, (Sep, 2005) 105701.
- [13] J. Dziarmaga, “Dynamics of a quantum phase transition: Exact solution of the quantum Ising model,” *Physical review letters* (2005) 245701, [arXiv:cond-mat/0509490](#) [[arXiv:cond-mat](#)].
- [14] B. Damski and W. H. Zurek, “Dynamics of a quantum phase transition in a ferromagnetic bose-einstein condensate,” *Physical Review Letters* **99** no. 13, (Sep, 2007) 130402, [arXiv:0704.0440](#).
- [15] J. Dziarmaga, J. Meisner, and W. H. Zurek, “Winding Up of the Wave-Function Phase by an Insulator-to-Superfluid Transition in a Ring of Coupled Bose-Einstein Condensates,” *Physical Review Letters* **101** no. 11, (Sep, 2008) 115701.
- [16] M. Uhlmann, R. Schützhold, and U. R. Fischer, “ $o(n)$  symmetry breaking quantum quench: Topological defects versus quasiparticles.,” *Physical Review D* **81** no. 2, (Jan, 2010) 025017, [arXiv:0905.0877](#).
- [17] A. Rajantie and D. J. Weir, “Soliton form factors from lattice simulations,” *Physical Review D* **82** no. 11, (Dec, 2010) 111502.
- [18] J. Berges and S. Roth, “Topological defect formation from 2PI effective action techniques,” *Nuclear Physics B* **847** no. 1, (Jun, 2011) 197–219, [arXiv:1012.1212](#).
- [19] R. Rajaraman, *Solitons and Instantons*. North Holland, 1987.
- [20] T. Vachaspati, *Kinks and Domain Walls*. Cambridge University Press, 2006.
- [21] M. Schwartz, *Quantum Field Theory and the Standard Model*. Cambridge University Press, 2014.
- [22] O. A. McBryan and J. Rosen, “Existence of the critical point in  $\phi^4$  field theory,” *Communications in Mathematical Physics* **51** no. 2, (Jun, 1976) 97–105.

- [23] S. Weinberg, *The Quantum Theory of Fields, Volume 2: Modern Applications*. Cambridge University Press, 1996.
- [24] J. Zinn-Justin, *Quantum Field Theory and Critical Phenomena*. Clarendon Press, 2002.
- [25] J. Cardy, *Scaling and Renormalization in Statistical Physics (Cambridge Lecture Notes in Physics)*. Cambridge University Press, 1996.  
<http://www.worldcat.org/isbn/0521499593>.
- [26] S. P. Jordan, K. S. M. Lee, and J. Preskill, “Quantum computation of scattering in scalar quantum field theories,” *Quantum Info. Comput.* **14** no. 11-12, (Sept., 2014) 1014–1080.
- [27] V. Yurov and A. B. Zamolodchikov, “Correlation Functions of Integrable 2D Models of the Relativistic Field Theory: Ising Model,” *International Journal of Modern Physics A* **06** no. 19, (Aug, 1991) 3419–3440.
- [28] H. Kleinert and V. Schulte-Frohlinde, *Critical properties of  $\phi^4$ -theories*. World Scientific, River Edge, USA, 2001.
- [29] D. Giulini, “Superselection rules,” in *Compendium of Quantum Physics: Concepts, Experiments, History and Philosophy*, F. Weinert, K. Hentschel, D. Greenberger, and B. Falkenburg, eds., pp. 771–778. Springer, 2009.  
[arXiv:0710.1516](https://arxiv.org/abs/0710.1516).
- [30] S. Coleman, “Quantum sine-Gordon equation as the massive Thirring model,” *Physical Review D* **11** no. 8, (Apr, 1975) 2088–2097.
- [31] S. Mandelstam, “Xi. soliton operators for the quantized sine-gordon equation,” *Physics Reports* **23** no. 3, (1976) 307 – 313.
- [32] E. Weinberg, *Classical solutions in quantum field theory : solitons and instantons in high energy physics*. Cambridge University Press, 2012.
- [33] R. F. Dashen, B. Hasslacher, and A. Neveu, “Nonperturbative methods and extended-hadron models in field theory. I. Semiclassical functional methods,” *Physical Review D* **10** no. 12, (Dec, 1974) 4114–4129.
- [34] R. F. Dashen, B. Hasslacher, and A. Neveu, “Nonperturbative methods and extended-hadron models in field theory. II. Two-dimensional models and extended hadrons,” *Physical Review D* **10** no. 12, (Dec, 1974) 4130–4138.

- [35] M. Pawellek, “Quantum mass correction for the twisted kink,” *Journal of Physics A: Mathematical and Theoretical* **42** no. 4, (Jan, 2009) 045404, arXiv:0802.0710 [hep-th].
- [36] A. Rebhan, A. Schmitt, and P. van Nieuwenhuizen, “One-loop results for kink and domain wall profiles at zero and finite temperature,” *Physical Review D* **80** no. 4, (Aug, 2009) 045012, arXiv:0903.5242.
- [37] N. H. Christ and T. D. Lee, “Quantum expansion of soliton solutions,” *Physical Review D* **12** no. 6, (Sep, 1975) 1606–1627.
- [38] J. L. Gervais, A. Jevicki, and B. Sakita, “Perturbation expansion around extended-particle states in quantum field theory,” *Physical Review D* **12** no. 4, (Aug, 1975) 1038–1051.
- [39] C. Papageorgakis and A. B. Royston, “Scalar soliton quantization with generic moduli,” *Journal of High Energy Physics* **2014** no. 6, (Jun, 2014) 3, arXiv:1403.5017.
- [40] G. Delfino, “Universal amplitude ratios in the two-dimensional Ising model,” *Physics Letters B* **419** no. 1-4, (Feb, 1998) 291–295, arXiv:hep-th/9710019 [hep-th].
- [41] E. Fradkin, “Disorder Operators and Their Descendants,” *Journal of Statistical Physics* **167** no. 3-4, (May, 2017) 427–461, arXiv:1610.05780.
- [42] S. Sachdev, *Quantum Phase Transitions*. Cambridge University Press, second ed ed., 2011. <http://onlinelibrary.wiley.com/doi/10.1002/9780470022184.hmm108/full>.
- [43] A. Polkovnikov, “Universal adiabatic dynamics across a quantum critical point,” *Physical Review B - Condensed Matter and Materials Physics* **72** no. 16, (Dec, 2003) 1–5, arXiv:cond-mat/0312144 [cond-mat].
- [44] J. Dziarmaga, “Dynamics of a Quantum Phase Transition and Relaxation to a Steady State,” *Advances in Physics* (Dec, 2009) 1063–1189, arXiv:0912.4034.
- [45] A. Rajantie and A. Tranberg, “Counting defects with the two-point correlator,” *Journal of High Energy Physics* **2010** no. 8, (Aug, 2010) 86, arXiv:1005.0269.

- [46] J. Smit, *Introduction to Quantum Fields on a Lattice*. Cambridge University Press, Cambridge, 2002.  
<http://ebooks.cambridge.org/ref/id/CB09780511583971>.
- [47] C. Davies, “Lattice qcd - a guide for people who want results,” *Preprint. Lectures at 58th Scottish Universities Summer School in Physics, Hadron physics* (10, 2005) , [arXiv:hep-lat/0509046](https://arxiv.org/abs/hep-lat/0509046).
- [48] J. Groeneveld, J. Jurkiewicz, and C. P. K. Altes, “Twist as a Probe for Phase Structure,” *Physica Scripta* **23** no. 5B, (May, 1981) 1022–1031.
- [49] J. C. Ciria and A. Tarancón, “Renormalization group study of the soliton mass in the (1+1)-dimensional  $\lambda\Phi^4$  lattice model,” *Physical Review D* **49** no. 2, (Jan, 1994) 1020–1028, [arXiv:hep-lat/9309019](https://arxiv.org/abs/hep-lat/9309019) [hep-lat].
- [50] A. C. Davis, T. W. Kibble, A. Rajantie, and H. P. Shanahan, “Topological defects in lattice gauge theories,” *Journal of High Energy Physics* **2000** no. 11, (Nov, 2000) 010–010, [arXiv:hep-lat/0009037](https://arxiv.org/abs/hep-lat/0009037) [hep-lat].
- [51] A. Rajantie and D. J. Weir, “Nonperturbative study of the ’t Hooft-Polyakov monopole form factors,” *Physical Review D* **85** no. 2, (Jan, 2012) 025003, [arXiv:1109.0299](https://arxiv.org/abs/1109.0299).
- [52] M. E. Peskin and D. V. Schroeder, *An Introduction To Quantum Field Theory*. New York : Westview Press, 1995.
- [53] S. D. Drell, M. Weinstein, and S. Yankielowicz, “Strong-coupling field theory. I. Variational approach to  $\varphi^4$  theory,” *Physical Review D* **14** no. 2, (Jul, 1976) 487–516.
- [54] M. B. Hastings, “An area law for one-dimensional quantum systems,” *Journal of Statistical Mechanics: Theory and Experiment* **2007** no. 08, (Aug, 2007) P08024–P08024, [arXiv:0705.2024](https://arxiv.org/abs/0705.2024).
- [55] I. Arad, A. Kitaev, Z. Landau, and U. Vazirani, “An area law and sub-exponential algorithm for 1D systems,” *preprint* (Jan, 2013) 1–18, [arXiv:1301.1162](https://arxiv.org/abs/1301.1162).
- [56] M. B. Hastings, “Entropy and entanglement in quantum ground states,” *Physical Review B - Condensed Matter and Materials Physics* **76** no. 3, (2007) 035114, [arXiv:cond-mat/0701055](https://arxiv.org/abs/cond-mat/0701055) [cond-mat].

- [57] M. B. Hastings, “Solving gapped hamiltonians locally,” *Phys. Rev. B* **73** (Feb, 2006) 085115.
- [58] B. Pirvu, V. Murg, J. I. Cirac, and F. Verstraete, “Matrix product operator representations,” *New Journal of Physics* **12** (2010) 025012, [arXiv:0804.3976](#).
- [59] F. Brandão and M. Horodecki, “Exponential Decay of Correlations Implies Area Law,” *Communications in Mathematical Physics* **333** no. 2, (Jan, 2015) 761–798, [arXiv:1206.2947](#).
- [60] M. L. Wall and L. D. Carr, “Out-of-equilibrium dynamics with matrix product states,” *New Journal of Physics* **14** no. 12, (Dec, 2012) 125015.
- [61] J. Eisert, M. Cramer, and M. B. Plenio, “Colloquium : Area laws for the entanglement entropy,” *Reviews of Modern Physics* **82** no. 1, (Feb, 2010) 277–306, [arXiv:0808.3773](#).
- [62] L. Amico, R. Fazio, A. Osterloh, and V. Vedral, “Entanglement in many-body systems,” *Reviews of Modern Physics* **80** no. 2, (2008) 517–576, [arXiv:quant-ph/0703044](#) [quant-ph].
- [63] P. Calabrese and J. Cardy, “Entanglement entropy and quantum field theory: a non-technical introduction,” [arXiv:quant-ph/0505193](#) [quant-ph].
- [64] M. P. Hertzberg and F. Wilczek, “Some calculable contributions to entanglement entropy,” *Physical Review Letters* **106** no. 5, (2011) 1–5, [arXiv:1007.0993](#).
- [65] C. Holzhey, F. Larsen, and F. Wilczek, “Geometric and renormalized entropy in conformal field theory,” *Nuclear Physics, Section B* **424** no. 3, (1994) 443–467, [arXiv:hep-th/9403108](#) [hep-th].
- [66] M. P. Hertzberg, “Entanglement entropy in scalar field theory,” *Journal of Physics A: Mathematical and Theoretical* **46** no. 1, (Jan, 2013) 015402, [arXiv:1209.4646](#).
- [67] J. S. Cotler and M. T. Mueller, “Entanglement entropy and variational methods: Interacting scalar fields,” *Annals of Physics* **365** (2016) 91–117, [arXiv:1509.05685](#).

- [68] U. Schollwöck, “The density-matrix renormalization group in the age of matrix product states,” *Annals of Physics* **326** no. 1, (Jan, 2011) 96–192, [arXiv:1008.3477](#).
- [69] J. Eisert, “Entanglement and tensor network states,” *Modeling and Simulation* **3** no. 520, (Aug, 2013) 39, [arXiv:1308.3318](#).
- [70] C. Hubig, I. P. McCulloch, and U. Schollwöck, “Generic construction of efficient matrix product operators,” *Physical Review B* **95** no. 3, (Jan, 2017) 035129, [arXiv:1611.02498](#).
- [71] J. Haegeman, T. J. Osborne, and F. Verstraete, “Post-matrix product state methods: To tangent space and beyond,” *Physical Review B - Condensed Matter and Materials Physics* **88** no. 7, (2013) 075133, [arXiv:1305.1894](#).
- [72] L. Vanderstraeten, F. Verstraete, and J. Haegeman, “Scattering particles in quantum spin chains,” *Physical Review B* **92** no. 12, (Sep, 2015) 125136, [arXiv:1506.01008](#).
- [73] M. Lubasch, J. I. Cirac, and M.-C. Bañuls, “Unifying projected entangled pair state contractions,” *New Journal of Physics* **16** no. 3, (Mar, 2014) 033014, [arXiv:1311.6696](#).
- [74] J. Haegeman and F. Verstraete, “Diagonalizing Transfer Matrices and Matrix Product Operators: A Medley of Exact and Computational Methods,” *Annual Review of Condensed Matter Physics* **8** no. 1, (Mar, 2017) 355–406, [arXiv:1611.08519](#).
- [75] G. Evenbly, “Algorithms for tensor network renormalization,” *Physical Review B* **95** no. 4, (Jan, 2017) 045117, [arXiv:1509.07484](#).
- [76] M. Bal, M. Mariën, J. Haegeman, and F. Verstraete, “Renormalization Group Flows of Hamiltonians Using Tensor Networks,” *Physical Review Letters* **118** no. 25, (Jun, 2017) 250602, [arXiv:1703.00365](#).
- [77] S. Yang, Z. Gu, and X. Wen, “Loop Optimization for Tensor Network Renormalization,” *Physical Review Letters* **118** no. 11, (Mar, 2017) 110504, [1512.04938](#).
- [78] P. Absil, R. Mahony, and R. Sepulchre, *Optimization Algorithms on Matrix Manifolds*. Princeton University Press, Jan, 2008.

- [79] P. Pippa, S. R. White, and H. G. Evertz, “Efficient matrix-product state method for periodic boundary conditions,” *Physical Review B* **81** no. 8, (Feb, 2010) 081103, [arXiv:0801.1947](#).
- [80] D. Rossini, V. Giovannetti, and R. Fazio, “Stiffness in 1D matrix product states with periodic boundary conditions,” *Journal of Statistical Mechanics: Theory and Experiment* **2011** no. 05, (May, 2011) P05021, [arXiv:1102.3562](#).
- [81] V. Zauner-Stauber, L. Vanderstraeten, M. T. Fishman, F. Verstraete, and J. Haegeman, “Variational optimization algorithms for uniform matrix product states,” *Phys. Rev. B* **97** (Jan, 2018) 045145.
- [82] B. Pirvu, F. Verstraete, and G. Vidal, “Exploiting translational invariance in matrix product state simulations of spin chains with periodic boundary conditions,” *Physical Review B* **83** no. 12, (Mar, 2011) 125104, [arXiv:1005.5195](#).
- [83] J. Haegeman, B. Pirvu, D. J. Weir, J. I. Cirac, T. J. Osborne, H. Verschelde, and F. Verstraete, “Variational matrix product ansatz for dispersion relations,” *Physical Review B* **85** no. 10, (Mar, 2012) 100408, [arXiv:1103.2286](#).
- [84] E. Gillman and A. Rajantie, “Topological defects in quantum field theory with matrix product states,” *Phys. Rev. D.* **96** (Nov, 2017) 094509, [arXiv:1705.09802](#).
- [85] S. Singh and G. Vidal, “Global symmetries in tensor network states: Symmetric tensors versus minimal bond dimension,” *Physical Review B* **88** no. 11, (Sep, 2013) 115147, [arXiv:1307.1522](#).
- [86] B. Pirvu, G. Vidal, F. Verstraete, and L. Tagliacozzo, “Matrix product states for critical spin chains: Finite-size versus finite-entanglement scaling,” *Physical Review B* **86** no. 7, (Aug, 2012) 075117, [arXiv:1204.3934](#).
- [87] G. Vidal, “Class of Quantum Many-Body States That Can Be Efficiently Simulated,” *Physical Review Letters* **101** no. 11, (Sep, 2008) 110501, [arXiv:quant-ph/0610099](#) [quant-ph].
- [88] J. Berges, “Introduction to Nonequilibrium Quantum Field Theory,” *AIP Conference Proceedings* **739** no. 1, (2004) , [arXiv:hep-ph/0409233](#) [hep-ph].

- [89] S. Sotiriadis and J. Cardy, “Quantum quench in interacting field theory: A self-consistent approximation,” *Physical Review B - Condensed Matter and Materials Physics* **81** no. 13, (2010) 134305, [arXiv:1002.0167](#).
- [90] M. Salle, J. Smit, and J. C. Vink, “Thermalization of inhomogeneous quantum scalar fields in 1+1D,” in *AIP Conference Proceedings*, vol. 555, pp. 429–432. AIP, 2001. [arXiv:hep-ph/0010239](#) [hep-ph].  
<http://aip.scitation.org/doi/abs/10.1063/1.1363556>.
- [91] J. Berges, “N-particle irreducible effective action techniques for gauge theories,” *Phys. Rev. D* **70** (2004) 105010, [arXiv:hep-ph/0401172](#) [hep-ph].
- [92] J. Berges, “Controlled nonperturbative dynamics of quantum fields out of equilibrium,” *Nuclear Physics A* **699** no. 3, (2002) 847 – 886.
- [93] J. Berges and I. O. Stamatescu, “Simulating nonequilibrium quantum fields with stochastic quantization techniques,” *Physical Review Letters* **95** no. 20, (2005) 202003, [arXiv:hep-lat/0508030](#) [hep-lat].
- [94] E. Seiler, “Status of complex langevin,” *preprint* (2017) , [arXiv:1708.08254](#) [hep-lat].
- [95] G. Aarts, F. A. James, J. M. Pawłowski, E. Seiler, D. Sexty, and I. O. Stamatescu, “Stability of complex Langevin dynamics in effective models,” *Journal of High Energy Physics* **1303** no. 3, (2013) 073, [arXiv:1212.5231](#).
- [96] J. Berges and D. Sexty, “Real-time gauge theory simulations from stochastic quantization with optimized updating,” *Nucl. Phys.* **B799** (2008) 306–329, [arXiv:0708.0779](#) [hep-lat].
- [97] S. Rychkov and L. G. Vitale, “Hamiltonian truncation study of the  $\phi^4$  theory in two dimensions,” *Physical Review D* **91** no. 8, (Apr, 2015) 085011, [arXiv:1412.3460](#).
- [98] Z. Bajnok and M. Lajer, “Truncated Hilbert space approach to the 2d  $\phi^4$  theory,” *Journal of High Energy Physics* **2016** no. 10, (Oct, 2016) 50, [arXiv:1512.06901](#).
- [99] T. Rakovszky, M. Mestyán, M. Collura, M. Kormos, and G. Takács, “Hamiltonian truncation approach to quenches in the ising field theory,” *Nuclear Physics B* (2016) 805–845, [arXiv:1607.01068](#).

- [100] A. Alexandru, G. Basar, P. F. Bedaque, and G. W. Ridgway, “Schwinger-Keldysh on the lattice: a faster algorithm and its application to field theory,” [arXiv:1704.06404](#).
- [101] S. Sengupta, F. C. Khanna, and S. P. Kim, “Nonequilibrium evolution of correlation functions: A canonical approach,” *Physical Review D* **68** no. 10, (Nov, 2003) 105014, [arXiv:hep-ph/0301071](#) [hep-ph].
- [102] G. Carleo, F. Becca, L. Sanchez-Palencia, S. Sorella, and M. Fabrizio, “Light-cone effect and supersonic correlations in one- and two-dimensional bosonic superfluids,” *Physical Review A* **89** no. 3, (Mar, 2014) 031602, [arXiv:1310.2246](#).
- [103] P. Kramer and M. Saraceno, “Geometry of the Time-Dependent Variational Principle in Quantum Mechanics,” in *Lecture Notes in Physics*. Springer-Verlag Berlin, 1981.
- [104] G. Carleo, F. Becca, M. Schiró, and M. Fabrizio, “Localization and Glassy Dynamics Of Many-Body Quantum Systems,” *Scientific Reports* **2** no. 1, (Dec, 2012) 243, [arXiv:1109.2516](#).
- [105] G. Carleo and M. Troyer, “Solving the Quantum Many-Body Problem with Artificial Neural Networks,” [arXiv:1606.02318](#).
- [106] R. Jackiw and A. Kerman, “Time Dependent Variational Principle and the Effective Action,” *Phys. Lett.* **A71** (1979) 158–162.
- [107] P. Calabrese and J. Cardy, “Evolution of entanglement entropy in one-dimensional systems,” *Journal of Statistical Mechanics: Theory and Experiment* **2005** no. 04, (Apr, 2005) P04010, [arXiv:cond-mat/0503393](#) [cond-mat].
- [108] J. S. Cotler, M. P. Hertzberg, M. Mezei, and M. T. Mueller, “Entanglement growth after a global quench in free scalar field theory,” *Journal of High Energy Physics* **2016** no. 11, (2016) , [arXiv:1609.00872](#).
- [109] G. Vidal, “Efficient classical simulation of slightly entangled quantum computations,” *Physical Review Letters* **91** no. 14, (Oct, 2003) 147902, [arXiv:quant-ph/0301063](#) [quant-ph].
- [110] J. J. García-Ripoll, “Time evolution of matrix product states,” *New Journal of Physics* **8** (2006) 305.

- [111] A. Müller-Hermes, J. Ignacio Cirac, and M. C. Bañuls, “Tensor network techniques for the computation of dynamical observables in one-dimensional quantum spin systems,” *New Journal of Physics* **14** no. 7, (Jul, 2012) 075003, [arXiv:1204.5080](https://arxiv.org/abs/1204.5080).
- [112] J. Haegeman, J. I. Cirac, T. J. Osborne, I. Pižorn, H. Verschelde, and F. Verstraete, “Time-Dependent Variational Principle for Quantum Lattices,” *Physical Review Letters* **107** no. 7, (Aug, 2011) 070601, [arXiv:1103.0936](https://arxiv.org/abs/1103.0936).
- [113] E. Leviatan, F. Pollmann, J. H. Bardarson, and E. Altman, “Quantum thermalization dynamics with Matrix-Product States,” [arXiv:1702.08894](https://arxiv.org/abs/1702.08894).  
<http://arxiv.org/abs/1702.08894>.
- [114] J. Haegeman, M. Mariën, T. J. Osborne, and F. Verstraete, “Geometry of matrix product states: Metric, parallel transport, and curvature,” *Journal of Mathematical Physics* **55** no. 2, (Feb, 2014) 021902, [arXiv:1210.7710](https://arxiv.org/abs/1210.7710).
- [115] J. Haegeman, M. Marien, T. J. Osborne, and F. Verstraete, “Geometry of matrix product states: Metric, parallel transport, and curvature,” *Journal of Mathematical Physics* **55** no. 2, (2014) 021902, [arXiv:1210.7710](https://arxiv.org/abs/1210.7710).
- [116] J. Haegeman, C. Lubich, I. Oseledets, B. Vandereycken, and F. Verstraete, “Unifying time evolution and optimization with matrix product states,” *Physical Review B* **94** no. 16, (Oct, 2016) 165116, [arXiv:1408.5056](https://arxiv.org/abs/1408.5056).
- [117] E. Gillman and A. Rajantie, “The Kibble Zurek Mechanism of Topological Defect Formation in Quantum Field Theory with Matrix Product States,” *preprint. Accepted for publication in Phy. Rev. D* (Nov, 2017) 1–17, [arXiv:1711.10452](https://arxiv.org/abs/1711.10452).
- [118] E. M. Stoudenmire and S. R. White, “Minimally entangled typical thermal state algorithms,” *New Journal of Physics* **12** no. 5, (May, 2010) 055026, [arXiv:1002.1305](https://arxiv.org/abs/1002.1305).